



UNIVERSIDAD AUTÓNOMA DE SAN LUIS POTOSÍ
FACULTAD DE CIENCIAS QUÍMICAS

**“DISEÑO DE COMPOSITOS FUNCIONALES DE
PSi/QUITOSANO: SÍNTESIS,
CARACTERIZACIÓN Y EVALUACIÓN EN
TERAPÉUTICOS”**

TESIS PARA OBTENER EL GRADO DE:
DOCTOR EN CIENCIAS EN INGENIERÍA QUÍMICA

PRESENTA
M.C. CÁNDIDA ANAHY CISNEROS COVARRUBIAS

DIRECTORA DE TESIS
DRA. ALMA GABRIELA PALESTINO ESCOBEDO



SAN LUIS POTOSÍ, S.L.P. MAYO DE 2021



UNIVERSIDAD AUTÓNOMA DE SAN LUIS POTOSÍ

FACULTAD DE CIENCIAS QUÍMICAS

**“DISEÑO DE COMPOSITOS FUNCIONALES DE
PSi/QUITOSANO: SÍNTESIS, CARACTERIZACIÓN Y
EVALUACIÓN EN TERAPÉUTICOS”**

TESIS PARA OBTENER EL GRADO DE:
DOCTOR EN CIENCIAS EN INGENIERÍA QUÍMICA

P R E S E N T A:

M.C. CÁNDIDA ANAHY CISNEROS COVARRUBIAS

DIRECTORA DE TESIS

DRA. ALMA GABRIELA PALESTINO ESCOBEDO

SINODALES:

Dra. Alma Gabriela Palestino Escobedo

Dr. Sergio Rosales Mendoza

Dr. Omar González Ortega

Dr. Raúl Ocampo Pérez

Dr. Raúl González García



SAN LUIS POTOSÍ, S.L.P. MAYO 2021

El programa de Doctorado de la Universidad Autónoma de San Luis Potosí pertenece al Programa Nacional de Posgrados de Calidad (PNPC) del CONACYT, registro 000897.

Número de registro de la beca otorgada por CONACYT: 335248

Este trabajo fue apoyado por donaciones del CONACYT: CB 2017/2018 Project, No. A1-S-31287.



DISEÑO DE COMPOSITOS FUNCIONALES DE PSi/QUITOSANO:
SÍNTESIS, CARACTERIZACIÓN Y EVALUACIÓN EN TERAPÉUTICOS
por Cándida Anahy Cisneros Covarrubias se distribuye bajo una Licencia
Creative Commons Atribución-NoComercial-SinDerivadas 4.0
Internacional.

AGRADECIMIENTOS

PERSONALES

Principalmente agradezco a Dios por ser mi fortaleza en los momentos difíciles, por permitirme obtener un logro más en mi vida profesional y por concederme vida, salud y amor.

A mi padre, el Sr. José Santos Cisneros Medrano por ser mi fortaleza y mi pilar, por apoyarme en cada una de mis decisiones a pesar de la distancia, por comprenderme, por el esfuerzo que hace en todo momento para darme lo mejor y por el amor incondicional que me ha brindado.

A mi hermano Juan Alberto por estar siempre a mi lado, por los momentos especiales que hemos vivido juntos, por llenar mi vida de alegría y amor, y por apoyarme durante esta etapa.

Al destino, por poner a mi lado a mi esposo Hugo René. Gracias por toda la felicidad y el amor que me das, por ser mi compañero de vida, por caminar a mi lado durante estos 4 años, por comprenderme en mis momentos de estrés, por darme ánimos cuando quiero rendirme, por el tiempo que me dedicas, por tu paciencia, por motivarme a ser mejor, por apoyarme a cumplir mis metas, por los momentos bonitos y, sobre todo, por aguantar mi carácter en momentos complicados. Te amo!!!.

A la Dra. Gaby Palestino por aceptarme como su estudiante para realizar este trabajo de investigación, por darme la oportunidad de ser parte de su equipo de trabajo, por las palabras de apoyo brindadas en momentos difíciles, por todos los conocimientos brindados, por sus consejos tanto personales como académicos, por escuchar mis inquietudes, mis tristezas y alegrías, y por ser además de mi asesora, mi amiga. Mi admiración y enorme cariño siempre para usted. Este logro no hubiera sido posible sin su apoyo, mil gracias.

A mi tío Javier Cisneros, por ser mi segundo papá, por guiarme y apoyarme siempre, por escucharme, por quererme y por estar siempre pendiente de mi avance personal y profesional, sin duda alguna es una persona esencial en mi vida.

A mi tía Angélica Cisneros por su cariño y amor incondicional, por estar siempre para mí, por apoyarme en todos los sentidos y por el esfuerzo que hace día a día para ayudarme a concluir esta etapa.

A mi segunda mamá, Elena, gracias por ser quién eres conmigo, por educarme, por los valores que me diste, por tu inmenso amor y por cuidarme siempre a pesar de la distancia.

A mis compañeros y amigos de laboratorio por sus comentarios constructivos y positivos, por los momentos agradables, por la convivencia, por las pláticas en momentos de estrés, agradezco a todos su tiempo y cariño.

A la Dra. Lourdes Betancourt por su tiempo, por compartir conmigo sus conocimientos, por su apoyo incondicional en la escritura y discusión del artículo científico, por su compañerismo y sobre todo por su bonita amistad.

Al Dr. Azael Gómez Durán por estar siempre pendiente de mis avances, por su apoyo en cada duda, por compartir conmigo sus conocimientos y por brindarme momentos de diversión y distracción en días pesados.

Al Dr. Omar González Ortega por los comentarios constructivos en cada avance de tesis, por el apoyo en la revisión del artículo científico y por las asesorías brindadas durante mis estudios de doctorado.

Al Dr. Raúl González García por las asesorías brindadas y conocimientos compartidos en la discusión del diseño de experimentos y por su tiempo.

A mi amiga Diana Moreno por el bonito lazo de amistad que hemos formado, por hacer mi vida más feliz, por brindarme siempre palabras de motivación, por su cariño, por apoyarme en las mejores etapas de mi vida y por su amistad incondicional.

A mi amiga Fide Báez por apoyarme en la realización de mis experimentos, por la bonita amistad que formamos, por tomar café conmigo para distraernos un poco mientras realizamos los experimentos de liberación, por su confianza y disponibilidad siempre, por las risas y pláticas agradables.

A mi amiga Janeth Moreno por su amistad, confianza y apoyo en algunos experimentos de mi tesis y por los momentos de convivencia en días pesados de

experimentos (fines de semana).

A mi amigo César Del Ángel por su linda amistad y por las pláticas por whatsapp en momentos de estrés y desesperación.

A Elioth y Jeny por su apoyo durante su servicio social.

INSTITUCIONALES

A la Universidad Autónoma de San Luis Potosí, que a través del Doctorado en Ciencias en Ingeniería Química me dio la oportunidad de realizar mis estudios de doctorado y de desarrollar el presente trabajo de investigación.

Al laboratorio de Biopolímeros y Nanoestructuras de la Facultad de Ciencias Químicas, por brindarme el espacio, material, reactivos y equipos necesarios para desarrollar mi proyecto de tesis.

Al laboratorio de Bionanomateriales del Centro de Investigación en Ciencias de la Salud y Biomedicina por el espacio otorgado para desarrollar parte experimental del proyecto de tesis.

Al Consejo Nacional de Ciencia y Tecnología (CONACYT) por la beca No. 335248 otorgada durante los estudios de doctorado, y la beca otorgada por el proyecto A1-S-31287 para concluir la tesis doctoral y la escritura de un artículo científico. Un agradecimiento adicional por los fondos brindados realizar esta investigación a través del proyecto CB 2017/2018, No. A1-S-31287.

A mi Comité Tutorial: Dr. Omar González Ortega, Dr. Raúl Ocampo Pérez, Dr. Raúl González García y Dr. Sergio Rosales Mendoza por las aportaciones realizadas durante las revisiones de avance, por sus comentarios constructivos y por el apoyo que sin duda alguna enriqueció este trabajo de tesis.

Al Dr. Jaime Reyes Hernández por el apoyo brindado, permitiendo el uso de sus instalaciones y equipo para la realización de mis experimentos de TGA.

A la Dra. Patricia Aguirre Bañuelos y a la M.C. Rosa Alejandra Hernández Esquivel del Laboratorio de Farmacología por su aportación a este proyecto mediante la realización de los experimentos in vivo.

DEDICATORIA



Al gran amor de mi vida: Mi madre

Profra. Ma. De la Paz Covarrubias Bernal

1969 - 2013

No solo te agradezco mi vida, te dedico cada paso que doy
“TU CORAZÓN VIVE EN EL MÍO, PORQUE NO IMPORTA DONDE TE
ENCUENTRES, YO SIEMPRE TE LLEVO CONMIGO”

A mi hija

Ana Victoria Carrizalez Císneros

El mejor regalo de la vida, mi felicidad de cada día
Mi motivo para crecer personal y profesionalmente siempre

“La vida no es fácil, para ninguno de nosotros. Pero.... ¡qué importa! Hay que perseverar y, sobre todo, tener confianza en uno mismo. Hay que sentirse dotado para realizar alguna cosa y esa cosa hay que alcanzarla, cueste lo que cueste”.

Marie Curie

PRODUCTOS OBTENIDOS

ARTÍCULOS CIENTÍFICOS

- Cisneros-Covarrubias C. A., Palestino G., Gómez-Durán C. F. A. Rosales-Mendoza S. and Betancourt-Mendiola M. L. Optimized microwave-assisted functionalization and quantification of superficial amino groups on porous silicon nanostructured microparticles. *Anal. Methods*, 2021, 13, 516. DOI: 10.1039/d0ay02083d.
- Cisneros-Covarrubias C. A., Gómez-Durán César F. A., Aguirre Bañuelos P., Hernández-Esquivel R. A. and Palestino G. Porous silicon microparticles as nanovehicles for the sustained release of tramadol: Kinetic, physicochemical and biological evaluation (**En correcciones**).

CONGRESOS

- 4° Simposio Potosino de Investigación en Ciencia de Materiales. IPICYT. San Luis Potosí, S.L.P. 11 – 13 de Abril de 2018. “Estudio comparativo de los parámetros de síntesis de micro/nanopartículas de silicio poroso obtenidas por ataque electroquímico”. Autores: Cándida Anahy Cisneros Covarrubias a, César Fernando Azael Gómez Durán a, Alma Gabriela Palestino Escobedo.
- 1° Simposio Interno de Investigación. CICSAB. UASLP. San Luis Potosí, S.L.P. 3 de Diciembre de 2018. Ponencia. “Síntesis, caracterización y evaluación de propiedades de vehículos nanoestructurados de silicio poroso para la liberación sostenida de fármacos.
- XXVIII International Materials Research Congress. Cancún, Quintana Roo, México. 18 – 23 de Agosto de 2019. “Porous silicon microparticles as nanovehicles for the sustained release of tramadol: kinetic, physicochemical and biological evaluation”. Autores: Cándida A. Cisneros-Covarrubias, César F. A. Gómez-Durán, Gabriela Palestino.

- Segundo Encuentro de Ingeniería Química. Facultad de Ciencias Químicas. UASLP. 24 de Septiembre de 2019. "Micropartículas de silicio poroso como nanovehículos para la liberación sostenida de tramadol: evaluación fisicoquímica y cinética". Autores: Cándida Anahy Cisneros-Covarrubias, César F. A. Gómez-Durán, Gabriela Palestino.
- Segundo Curso-Taller: Eliminación de compuestos tóxicos del agua: Caracterización de materiales y sus aplicaciones. Facultad de Ciencias Químicas. UASLP. San Luis Potosí, S.L.P. "Micropartículas de silicio poroso como nanovehículos para la liberación sostenida de tramadol: evaluación fisicoquímica y cinética". Autores: Cándida Anahy Cisneros-Covarrubias, César F. A. Gómez-Durán, Gabriela Palestino.
- Concurso de Exhibición de Carteles de Proyectos de Investigación de Estudiantes de Posgrado. Centro Cultural Universitario Bicentenario, UASLP. San Luis Potosí, S.L.P. 11 de Octubre de 2019. "Micropartículas de silicio poroso como nanovehículos para la liberación sostenida de tramadol: evaluación fisicoquímica y cinética". Autores: Cándida Anahy Cisneros Covarrubias, Alma Gabriela Palestino Escobedo, César F. A. Gómez Durán, Lourdes Betancourt Mendiola.
- Simposio Virtual: Nanotecnología y sus aplicaciones en las áreas de la Química. San Luis Potosí, S.L.P. 14 – 16 de Octubre de 2020. "Micropartículas de silicio poroso como nanovehículos para la liberación sostenida de tramadol: evaluación fisicoquímica, cinética y biológica". Autores: Cándida A. Cisneros-Covarrubias, César F. A. Gómez-Durán, Gabriela Palestino, Aguirre Patricia, Hernández Alejandra.

PREMIOS

- 24 de Septiembre de 2019. Mejor cartel de la LGAC Materiales avanzados y nanoestructuras: polímeros, sensores y adsorbentes, con el Póster: "Micropartículas de silicio poroso como nanovehículos para la liberación

sostenida de tramadol: evaluación fisicoquímica y cinética". Autores: Cándida Anahy Cisneros-Covarrubias, César F. A. Gómez-Durán, Gabriela Palestino. Segundo Encuentro de Ingeniería Química. Facultad de Ciencias Químicas. UASLP. San Luis Potosí, S.L.P.

- 14 – 16 de Octubre de 2020. Segundo lugar en el concurso de carteles con el Póster: "Micropartículas de silicio poroso como nanovehículos para la liberación sostenida de tramadol: evaluación fisicoquímica, cinética y biológica". Autores: Cándida A. Cisneros-Covarrubias, César F. A. Gómez-Durán, Gabriela Palestino, Aguirre Patricia, Hernández Alejandra. Simposio Virtual: Nanotecnología y sus aplicaciones en las áreas de la Química. UASLP. San Luis Potosí, S.L.P.

RESUMEN

La investigación relacionada con los sistemas de liberación controlada de medicamentos ha crecido rápidamente en los últimos años, ya que estos sistemas ofrecen propiedades ventajosas tales como eficiencia mejorada, toxicidad mínima y administración amigable en comparación con los procedimientos tradicionales de administración de medicamentos. La mayoría de estos sistemas se han sintetizado utilizando biopolímeros biocompatibles y biodegradables con partículas nanoestructuradas con propiedades biocompatibles, no tóxicas y biodegradables. La combinación de estos materiales permite mejorar las propiedades del sistema de liberación. Principalmente mejorando la presentación temporal y espacial de los fármacos en el organismo y protegiéndolos de la degradación o eliminación fisiológica. En este trabajo se diseñaron, sintetizaron, caracterizaron y evaluaron las propiedades fisicoquímicas y morfológicas de partículas de silicio poroso térmicamente oxidadas (TOPSip) y de compositos funcionales a base de partículas de silicio poroso (PSip) y quitosano (CH). Se utilizó clorhidrato de tramadol (TR) como fármaco modelo para evaluar los perfiles de liberación acumulativa in vitro de TOPSip y de los compositos. Se obtuvieron los porcentajes de capacidad de carga de TR en TOPSip y compositos, y se demostró que la adsorción de TR se rige por fuerzas intermoleculares (fuerzas electrostáticas ion-ion y enlaces de hidrógeno) y por la dimensión de los poros. Se obtuvieron los perfiles de liberación acumulada de TR in vitro en fluidos simulados (gástrico e intestinal) para todos los sistemas de liberación diseñados, obteniendo un tiempo de liberación de 24 h para TOPSip desnudas y tiempos de 30 h para los compositos de PSip-CH con bajo efecto de estallido. Finalmente, la evaluación in vivo utilizando microportadores TOPSip mostró evidencia de efectos antinociceptivos y antiinflamatorios mejores y sostenibles cuando se usan los compositos TOPSip-OH/TR en comparación con TR solo.

ABSTRACT

Studies related to the controlled release system have developed rapidly in recent years to provide beneficial properties such as increased efficiency, reduced toxicity, and helpful administration compared to conventional treatment regimens. Many of these systems are synthesized by combining biopolymers and nanostructured particles, both materials with biodegradable and biocompatible properties and low toxicity. The combination of these materials makes it possible to improve the properties of the delivery system. Mainly improving the spatial and temporal presentation of drugs in the body and protecting them from degradation or physiological elimination. In this work, the physicochemical and morphological properties of thermally oxidized porous silicon particles (TOPSip) and functional composites based on porous silicon particles (PSip) and chitosan (CH) were designed, synthesized, characterized, and evaluated. Tramadol hydrochloride (TR) was used as a model drug to evaluate the in vitro cumulative release profiles of the TOPSip and composites. The percentages of TR loading capacity in TOPSip and composites were obtained, showing that TR adsorption was governed by intermolecular forces (ion-ion electrostatic forces and hydrogen bonding) and by pore dimension. The in vitro TR cumulative release profiles in simulated fluids (gastric and intestinal) were obtained for all the designed delivery systems, obtaining a release time of 24 h for bare TOPSip and for the PSip-CH composites times of 30 h with low burst effect. Finally, the in vivo evaluation using TOPSip microcarriers showed evidence of better and sustainable anti-nociceptive and anti-inflammatory effects when using TOPSip-OH/TR composites compared with TR alone.

INDEX

1. INTRODUCTION	1
1.1 Controlled drug delivery systems	1
1.2 Nanostructured porous silicon (PSi)	2
1.3 Chitosan (CH)	3
1.4 Tramadol hydrochloride (TR)	5
2. JUSTIFICATION	9
3. HYPOTHESIS	9
4. GENERAL OBJECTIVE	9
5. SPECIFIC OBJECTIVES	9
CHAPTER 1	11
 Porous silicon microparticles as nanovehicles for the sustained release of tramadol: Kinetic, physicochemical and biological evaluation	11
ABSTRACT	12
1. INTRODUCTION	13
2. MATERIALS AND METHODS.....	15
2.1 Materials	15
2.2 General procedure for the synthesis of PSi layers	15
2.3 Fabrication of PSi microparticles.....	17
2.4 TR loading and quantification in TOPSip	18
2.5 In vitro TR release.....	20
2.6 Physicochemical characterization of TOPSip.....	20
2.7 In vivo assessment	22
3. RESULTS AND DISCUSSIONS.....	24
3.1 Morphological characterization of TOPSip	24
3.2 FT-IR of TOPSip-OH pre-TR-loading and post-TR-loading.....	28
3.3 TR loading on TOPSip-OH.....	29
3.4 ζ -potential analysis.....	31
3.5 In vitro TR release study	33

3.6	TR release kinetics modeling	38
3.7	In vivo assessment	40
4.	CONCLUSIONS	45
CHAPTER 2		58
Optimized Microwave-Assisted Functionalization and Quantification of Superficial Amino Groups on Porous Silicon Nanostructured Microparticles ..		58
	ABSTRACT	59
1.	INTRODUCTION	59
2.	EXPERIMENTAL SECTION	63
2.1	General materials and methods	63
2.2	Synthesis of TOPSip	63
2.3	Functionalization of TOPSip-OH via traditional method	63
2.4	Functionalization of TOPSip via microwave irradiation	64
2.5	Physicochemical characterization of PSip	64
2.6	Central composite design (CCD)	64
2.7	Quantification of amino groups	65
3.	RESULTS AND DISCUSSION	65
3.1	Morphological characterization of PSip	65
3.2	Quantification of amino groups	68
3.3	Exploring experiments	69
3.4	APTES functionalization: The second-order model and analysis of variance (ANOVA)	71
3.5	Model fitting and statistical analysis	72
3.6	Response surface analysis and optimization process	76
3.7	Thermogravimetric Analysis	77
4.	CONCLUSIONS	80
CHAPTER 3		85
Design of functional PSi/CH composites: synthesis, characterization, and evaluation in therapeutics		85
	ABSTRACT	86

1. INTRODUCTION	86
2. EXPERIMENTAL SECTION	90
2.1 Materials	90
2.2 Synthesis of thermally oxidized porous silicon particles (TOPSip)	90
2.3 Surface modification	91
2.4 Drug loading.....	93
2.5 Synthesis of PSip/CH Composites	94
2.6 In vitro drug release study.....	95
2.7 Adsorption of mucin on PSi/CH composites.....	96
2.8 Physicochemical characterization of PSi microparticles and composites .	96
3. RESULTS AND DISCUSSION	98
3.1 Morphological characterization of TOPSip and PSip/CH composites	98
3.2 FT-IR of TOPSip-OH pre-TR-loading and post-TR-loading.....	101
3.3 ζ -potential analysis.....	103
3.4 Mucoadhesive strength of UnPSip/CH and TOPSip-OH/A/G/CH composites.....	106
3.5 TR loading and in vitro TR release study in UnPSip/CH and TOPSip- OH/A/G/CH	108
3.6 TR release kinetics modeling	111
4. CONCLUSIONS	112
GENERAL CONCLUSIONS	120
APPENDIX A	125
Published articles, Congresses and Awards certificates	125

INDEX OF FIGURES

CHAPTER 1. Porous silicon microparticles as nanovehicles for the sustained release of tramadol: Kinetic, physicochemical, and biological evaluation

- Fig. 1.** Schematic representation of the electrochemical etched cell used in the PSi synthesis. 16
- Fig. 2.** Schematic representation of free-standing PSi layers showing the different architectures. Single monolayers etched at (A) 17 mA/cm² for 2578 s, and (B) 15 mA/cm² for 3016 s. Multilayers formed by perforation method, the primary layer was obtained at 15 mA/cm² at the following etching times (C) 754, (D) 149, and (E) 73 s. (F) primary layer obtained at applying a current density of 10 mA/cm² for 48 s. According to the design, perforations were produced periodically by applying a current pulse of 50 mA/cm² for 3 s after each primary layer. 17
- Fig. 3.** Scheme of TOPSip hydroxylation and TR loading into TOPSip-OH by immersion method. 19
- Fig. 4.** Cross-sectional HRSEM images of thermally oxidized PSi layers. Single monolayers etched at (A) 17 mA/cm² for 2578 s (TOPSip_{M1}), and (B) 15 mA/cm² for 3016 s (TOPSip_{M2}). Multilayers formed by perforation method, the primary layer was produced using 15 mA/cm² current density at the following etching times (C) 754 s (TOPSip₋₄), (D) 149 s (TOPSip₋₂₀), and (E) 73 s (TOPSip₋₄₀). (F) Multilayer with a primary layer obtained at applying 10 mA/cm² current density for 48 s (TOPSip₋₈₀). After each primary layer, perforations were made by applying a current pulse of 50 mA/cm² for 3 s. The applied current density was periodically varied between these two values generating a total of 4, 20, 40, and 80 perforations for samples (C) to (F), respectively. 25

Fig. 5. HR-SEM and HR-TEM micrographs showing particle size, thickness, and pore dimensions of TOPSip microparticles. Single-layers: (A,G) TOPSip _{M1} and (B,H) TOPSip _{M2} . Perforated layers: (C,I) TOPSip-4, (D,J) TOPSip-20, (E,K) TOPSip-40, and (F,L)TOPSip-80.	27
Fig. 6. ATR Fourier transform infrared spectra of (A) TR, (B) TOPSip-OH and (C) TOPSip-OH/TR.	29
Fig. 7. TR loading as a function of the pore size of the TOPSip-OH.	30
Fig. 8. Speciation diagram of TR.	31
Fig. 9. ζ-potential curve vs pH for TOPSip-OH (black line) and TOPSip-OH/TR with different TR load; TOPSip-OH/TR _{M2} (pink line) and TOPSip-OH/TR-40 (green line).	33
Fig. 10. In vitro release profiles of 1) Commercial extended-release formulation of TR and 2) TOPSip-OH/TR with different particle thickness and pore size at 37 °C in A) Simulated gastric fluid (pH 1.2) and B) Simulated intestinal fluid (pH 6.8). Cumulative release of TR as a function of the particle thickness and pore size of the TOPSip-OH; C) Simulated gastric fluid (pH 1.2) and D) Simulated intestinal fluid (pH 6.8). Overlaid contour at out-of-trend experimental points.	35
Fig. 11. Diffusion of the simulated fluid into the pores and counter-diffusion of the TR toward the solution in A) TOPSip-OH _{M2} : pore size 6 ± 1.1 nm, thickness 27 ± 7 μm, and B) TOPSip-OH-40: pore size 67 ± 7 , thickness 0.5 ± 0.08 μm. The TR molecules size is $X = 10.83$, $Y = 9.26$ and $Z = 6.75$ Å, with 255.47 Å ³ overall volume [19].	36
Fig. 12. Time-course of carrageenan-induced mechanical nociceptive threshold in animals receiving the treatments (data are shown as mean ± standard deviation, n = 4 rats per group).	42
Fig. 13. Antinociceptive effect of treatments measured as the increase in the area under the curve of mechanical threshold versus time. (data are presented as mean ± standard deviation, n = 4 rats per group). Significance: **p < 0.01, ***p < 0.001 and ****p < 0.0001 by comparison	43

with the control. +++p < 0.001 and ++++p < 0.0001 by comparison with TOPSip-OH. #p < 0.05 and #####p < 0.0001 between TR 3.3 vs TOPSip-OH/TR 3.3, 13.5 and TR 13.5 vs TOPSip-OH/TR 13.5. ^p < 0.01 between TOPSip-OH/TR 3.3 and 13.5.

Fig. 14. The time course of carrageenan-induced inflammatory edema in animals receiving the treatments (data are shown as mean \pm standard deviation, n = 4 rats per group). 44

Fig. 15. Comparative effect of treatments in Inflammation measured as the paw thickness area under curve over 12 h period. Data are shown as mean \pm standard deviation (n = 4 rats). Significance: *p < 0.05 and ****p < 0.0001 by comparison with the control and TOPSip-OH vs all groups. Significance: #p < 0.05, ###p < 0.01 and #####p < 0.0001 between TR 3.3 vs 13.5, TOPSip-OH 3.3, 13.5 and TR 13.5 vs TOPSip-OH 13.5. +++p < 0.001 between TOPSip-OH/TR 3.3 and 13.5. 45

CHAPTER 2. Optimized Microwave-Assisted Functionalization and Quantification of Superficial Amino Groups on Porous Silicon Nanostructured Microparticles

Scheme 1. Different pathways for TOPSip functionalization by traditional method (path B) and MW-assisted methods (paths A and C). 62

Fig. 1. Morphological and chemical analyses of TOPSip. HR-SEM micrograph showing: (A) TOPSip shape and (C) pore size. (B) Particle size distribution histogram. (D) Pore size distribution histogram. (E) HR-TEM micrograph of TOPSip. (F) STEM image and elemental mapping of TOPSip and (G) TOPSip-OH/APTES. 66

Fig. 2. ATR Fourier transform infrared spectra of (A) TOPSip (a) and TOPSip-OH (b) and (B) TOPSip-OH/APTES functionalized with different amounts of APTES: 2.19 (a), 1.504 (b), and 0.888 $\mu\text{mol mg}^{-1}$ (c). 67

Fig. 3. Titration curve of ζ -potential vs. pH for TOPSip-OH (pink line) and TOPSip-OH/APTES (green line) after functionalization. 68

Scheme 2. Reaction mechanism between ninhydrin and TOPSip-OH/APTES to produce Ruhemann's purple dye.	69
Fig. 4. [TOPSip-OH/APTES] experimental values plotted against predicted values from the regression model in uncoded values.	75
Fig. 5. Response surface plot of [TOPSip-OH/APTES] in uncoded values. Overlaid contour at optimal experimental conditions.	77
Fig. 6. Thermogravimetric analysis (TGA) curve of TOPSip-OH/APTES corresponding to sample 1 from Table 4.	78

CHAPTER 3. Design of functional PSi/CH composites: synthesis, characterization, and evaluation in therapeutics

Fig. 1. Functionalization steps of A) TOPSip-OH (thermal oxidation), TOPSip-OH/A (silanization), and TOPSip-OH/A/G (functionalization with glutaraldehyde). B) UnPSi layers (hydrosilylation) and UnPSip (ultrasonication process).	93
Fig. 2. Intermolecular interactions between the functional groups of TR and A) surface UnPSip groups and B) surface TOPSip-OH/A/G groups.	94
Fig. 3. HR-SEM micrographs of A) TOPSip, B) UnPSip/CH and C) TOPSip-OH/A/G/CH composites.	99
Fig. 4. STEM image and elemental mapping of A) TOPSip, B) UnPSip/CH and C) TOPSip-OH/A/G/CH.	100
Fig. 5. ATR Fourier transform infrared spectra of each synthetic step in the synthesis of composites as well as TR loading: A) UnPSip/TR/CH and B) TOPSip-OH/A/G/TR/CH.	103
Fig. 6. ζ -potential curve vs pH for each synthetic step as well as TR loading for A) UnPSip-/TR/CH and B) TOPSip-OH/A/G/TR/CH.	106
Fig. 7. Mucoadhesive strength of UnPSip/CH and TOPSip-OH/A/G/CH composites as a function of pH and mucin concentration.	108
Fig. 8. In vitro cumulative TR release profiles of UnPSip/CH and TOPSip-OH/A/G/CH at 37 °C in simulated gastric fluid (pH 1.2) and simulated	110

intestinal fluid (pH 6.8). Comparison with the cumulative TR release profiles of TOPSip-OH-40 (Chapter 1).

INDEX OF TABLES

CHAPTER 1. Porous silicon microparticles as nanovehicles for the sustained release of tramadol: Kinetic, physicochemical and biological evaluation

Table 1. Experimental conditions for preparation of porous silicon particles.	18
Table 2. Particle size, thickness, pore size, and porosity of TOPSip microparticles.	28
Table 3. TR loading as a function of TOPSip-OH pore size.	30
Table 4. TR delivery systems.	38
Table 5. Kinetic parameters of the TOPSip-OH/TR _{M1} , TOPSip-OH/TR _{M2} , TOPSip-OH/TR-4, TOPSip-OH/TR-20, TOPSip-OH/TR-40, TOPSip-OH/TR-80 at 37 °C and pH 1.2.	40

CHAPTER 2. Optimized Microwave-Assisted Functionalization and Quantification of Superficial Amino Groups on Porous Silicon Nanostructured Microparticles

Table 1. Measured concentration of APTES on TOPSip and TOPSip-OH using 2 and 5% APTES solution.	71
Table 2. Estimated regression coefficients and P-values of the second-order polynomial model for [TOPSip-OH/APTES].	72
Table 3. 2 ² factorial central composite design with coded and uncoded variables. Experimental and predicted values for the [TOPSip-OH/APTES].	74

Table 4. $\mu\text{mol APTES g}^{-1}$ TOPSip-OH calculated by NIHM and TGA. 79

Table 5. Molecular structure and physicochemical properties. 80

**CHAPTER 3. Design of functional PSi/CH composites: synthesis,
characterization, and evaluation in therapeutics**

Table 1. Kinetic parameters of the UnPSip/CH and TOPSip-OH/A/G/CH 112
composites at 37 °C and pH 1.2 and 6.8.

1. INTRODUCTION

For many years, pharmaceutical companies have focused on the synthesis of chemical compounds for the treatment of various diseases. For their administration, these therapeutic systems are traditionally obtained in different presentations, including tablets, capsules, suppositories, creams, aerosols, and injections, among some others. The typical formulation of these systems entails certain disadvantages, among them, an instantaneous release of the drug, which makes it difficult to maintain drug concentration levels within adequate therapeutic limits and a low availability of the drug. These disadvantages lead to a multiple dose regimen, which results in significant fluctuations of drug levels in the blood plasma. This effect can decrease the effectiveness of the therapeutic and / or cause a certain degree of toxicity that leads to side effects for patients [1,2]. One option to solve this problem is to use the new emerging technologies offered by nanotechnology, an area in which great progress has been made in the manipulation of supramolecular molecules and structures, which has made it possible to produce controlled drug delivery systems with programmed functions, that drive the drug to a specific site, with the optimal concentration, in a suitable time profile [3].

1.1 Controlled drug delivery systems

Studies related to the controlled release system have developed rapidly in recent years to provide beneficial properties such as increased efficiency, reduced toxicity, and helpful administration compared to conventional treatment regimens [4]. Controlled drug release systems are designed primarily with the objectives of i) obtaining greater control during exposure of the therapeutic substance over time and protecting them from premature elimination, ii) guiding the desired site of action, iii) reducing minimizing their exposure to other parts of the body and iv) helping to cross physiological barriers [5]. Nowadays, the most relevant in this area of study is the design of hybrid systems in which biodegradable and biocompatible biopolymers are combined with various nanostructured materials, producing a new generation of composites with special

properties. This better control of properties shown by hybrid systems has generated great scientific interest to design nanostructured materials with controlled morphologies and pore size that can be used for the development of controlled drug release systems.

In recent years, nanostructured materials have been considered as emerging vehicles for their application as controlled release systems. They have a great variety of advantages, one of the main ones being their great stability, in addition, they have physicochemical and structural properties that make them ideal for the transport of drugs. They can be designed with morphological and chemical properties that increase their biocompatibility and at the same time induce a controllable degradation rate in low toxicity degradation products, which can be eliminated via the kidneys [6]. Some of the most widely used emerging nanomaterials are clays [7], silica nanoparticles [8], graphene [9], carbon nanotubes [10] and porous silicon (PSi) [11].

1.2 Nanostructured porous silicon (PSi)

In recent years, nanostructured porous silicon (PSi) has been extensively used as an attractive and flexible material for biomedical applications mainly related to the development of platforms for drug delivery [12]. PSi is prepared by electrochemical anodization of highly doped crystalline silicon wafers, in aqueous and organic solutions containing hydrofluoric acid (HF) and a surfactant (ethanol). This type of synthesis makes it possible to modulate various characteristics of PSi to control the load and release kinetics of therapeutic agents according to the required applications. Porous silicon particles (PSip) are characterized by having a large surface area ($\sim 500\text{m}^2/\text{cm}^3$) and a highly reactive surface that can be chemically modified, through functionalization or chemical conjugation with other biomolecules of interest [13]. The pore size and porosity of the PSip can be adjusted by manipulating the synthesis parameters (current density and attack time) to use them as reservoirs of therapeutic agents of different sizes [14]. In addition, it is important to highlight that PSip have high biocompatibility and biodegradability since they degrade, in a physiological conditions, it is converted

to monomeric silicic acid (Si(OH)_4), which is the most natural form of silicon that exists in the environment [15].

It has been shown that PSip have resistance to chemical degradation and changes in pH, due to this PSip can be considered as transporting and releasing vehicles for drugs [16]. Some studies that have demonstrated the use of PSip as vehicles are those carried out by Salonen et al, they studied the releases of 5 drugs: furosemide, griseofulvin, antipyrine, ranitidine and ibuprofen and showed that release kinetics can be obtained in periods of 50 - 350 minutes, depending on interaction of the PSip with the drugs, the pH of the medium and the solubility of the drugs [17]. Another example is that of Maniya et al, they studied the release of an antiviral Acyclovir and demonstrated that release kinetics can be obtained in periods of 3-8 hours, which depends on the surface chemistry of the PSip [18].

Although PSip can control drug release behavior, increase oral bioavailability, and drug efficacy, and reduce adverse side effects, they have the disadvantage of the rapid rate of drug release and/or therapeutic agent. One strategy to control the rate of drug release is to coverage the PSip with a biopolymer. The most used biopolymers in this application are natural polymers such as agarose, collagen, polylysine, dextran, hyaluronic acid, chitosan, pectin, carboxymethylchitin, gelatin; in addition, synthetic polymers, and a combination of natural and synthetic polymers [19].

1.3 Chitosan (CH)

Chitosan is a cationic polysaccharide that is commercially available with different degrees of deacetylation (DD) and molecular weights (MW). This polysaccharide is produced from chitin through a deacetylation process that involves alkaline hydrolysis. It is interesting highlight that chitin is the second most abundant biopolymer in the world, is a renewable and sustainable product, and it has a low-cost. Chitin is obtained mainly from the seafood industry as a waste product, this product is used as a pharmaceutical

raw material. Other sources of obtaining chitin are bacteria, fungi, and crustacean shells [20,21]. The properties of CH come from the combination of DD and MW [20].

CH is a hydrophilic copolymer of glucosamine and N-acetylglucosamine. It is considered a reliable excipient due to its advantageous properties. CH has a pKa value of 6.3, that is, at pH values > 6 CH has low solubility, its improve effect is conditioned at the sites of absorption and loses its positive charge, forming aggregates and precipitating from solution [22]. However, a contrary behavior is shown at pH values < 6. CH has high solubility and positive charge, this characteristic provides good properties such as the ability to open tight junctions improving absorption, better interaction with cell membranes and excellent mucoadhesive properties [23]. This attractive property has been used to design drug delivery systems for different vias of administration. The positive charge of CH is the main reason for the mucoadhesion properties. Electrostatic interactions between positively charged CH and negatively charged mucin, presents in the mucus layer, are considered the reason for its good adhesion on mucosal surfaces [21]. Mucoadhesive properties of CH are mainly a function of MW and DD. It has been shown that the mucoadhesive properties of CH increase with high MW and DD, however, high MW and DD decrease the biodegradability of CH, thus preventing the release of therapeutic agents [24]. In vitro studies to determine the mucoadhesion of chitosan have been carried out indirectly, in which the adhesion of mucin on chitosan was evaluated, obtaining mucoadhesion forces ranging from 61.9 to 72% [25].

Based on this information, the idea is to produce a vehicle that allows the drug to be protected and transported until the target site is reached. Once there, fix it in the physiological membrane of interest, so that it can act as a metering valve for the therapeutic agent. Finally, the SiP/CH composite is a promising material for both controlled release and permeability of drugs through intestinal cells.

1.4 Tramadol hydrochloride (TR)

In this work, TR is used as a model drug to evaluate the release profiles of TOPSip and designed composites. TR is an analgesic used for the treatment, management, and relief of moderate to severe pain. TR exhibits opioid and non-opioid activity primarily in the central nervous system (CNS) and it is associated with morphine and codeine, which is 1/10 less powerful than codeine and 1/6000 than morphine. TR was approved as a synthetic analgesic in 1995 by the Food and Drug Administration (FDA) [26]. TR is a reuptake inhibitor of norepinephrine and serotonin. It is suggested for patients who do not respond to certain therapies, or who have contraindications to cyclooxygenase-2 (COX-2) inhibitors and non-selective anti-inflammatory drugs (NSAIDs) [27]. There is a wide variety of pharmaceutical formulations available for TR, which have been administered by different vias including oral, intramuscular, subcutaneous, intravenous, and sublingual [28]. After TR oral administration (main route of administration), TR shows a very fast and almost complete absorption, showing a maximum mean plasma concentration after 2 hours of being administered. TR undergoes first-pass metabolism in the liver and has a bioavailability of approximately 70%. Approximately 20% of the drug binds to plasma proteins and has a half-life of 6 hours. The extraction process involves the kidneys almost entirely. TR is excreted in the urine in different forms, approximately 30% as unchanged drug, 60% as metabolites, and 10% is excreted in the bile. Regarding its solubility, TR is not soluble in organic compounds, it is slightly soluble in acetone and very soluble in methanol and water (more than 20 mg/ml in the pH range of 1.2 to 7.5) [26]. TR is administered every 4 to 6 hours in doses of 50 mg to 100 mg, depending on the needs of the patient, without exceeding a maximum daily dose of 400 mg. The average effective daily dose of TR is between 100 mg and 300 mg [27].

REFERENCES

1. Kost J., Lapidot S. A., Kumar N., Chaubal M., Domb A. J., Kumar R. and Majeti N. V. Drug delivery systems. *Enc. of Pol. Sc. Tech.* 2004, 5, 697-721, John Wiley & Sons, Inc.
2. Hnawate, R. M. and Deore P. Nanoparticle - novel drug delivery system: A Review. *PharmaTutor*, 2017, 5, 9-23.
3. Kumar, D. S., Banji D., Madhavi B., Bodanapu V., Dondapati S. and Sri A. P. Nanostructured porous silicon a novel biomaterial for drug delivery. *International Journal of Pharmacy and Pharmaceutical Sciences.* 2009, 1, 8-16.
4. Hamidi M., Azadi A. and Rafiei P. Hydrogel nanoparticles in drug delivery. *Adv. Drug Deliv. Rev.*, 2008, 60, 1638–1649.
5. Savage D., Liu X. and Curley S. Porous silicon advances in drug delivery and immunotherapy, *Curr. Opin. Pharm.* 2013, 5, 834-841.
6. Bae K. H., Wang L. S., and Kurisawa M. Injectable biodegradable hydrogels: progress and challenges. *J. Mater. Chem. B.*, 2013, 1, 5371-5388.
7. Viseras C., Aguzzi C., Cerezo P. and Bedmar M. C. Biopolymer–clay nanocomposites for controlled drug delivery. *Mater. Sci. Tech.*, 2008, 24, 1020-1026.
8. Song B., Wu C. and Chang J. Dual drug release from electrospun poly (lactic-co-glycolic acid)/mesoporous silica nanoparticles composite mats with distinct release profiles. *Acta Biomater.*, 2012, 8, 1901-1907.
9. Goenka S., Sant V. and Sant S. Graphene-based nanomaterials for drug delivery and tissue engineering. *J. Control. Release*, 2014, 173, 75-88.
10. Cirillo G., Hampel S., Spizzirri U. G., Parisi O. I., Picci N. and Iemma F. Carbon nanotubes hybrid hydrogels in drug delivery: a perspective review”, *Biomed Res Int.* 2014.
11. Low S. P., Williams K. A., Canham L. T. and Voelcker N. H. Evaluation of mammalian cell adhesion on surface-modified porous silicon. *Biomaterials*, 2006, 27, 4538–4546.

12. Zhang H., Liu D., Shahbazi M. A., Mäkilä E., Herranz-Blanco B., Salonen J., Hirvonen J. and Santos H. A. Fabrication of a Multifunctional Nano-in-micro-Drug Delivery Platform by Microfluidic Templated Encapsulation of Porous Silicon in Polymer Matrix, *Adv. Mater.* 2014, 26, 4497–4503.
13. Wang C. F., Mäkilä E. M., Kaasalainen M. H., Liu D., Sarparanta M. P., Airaksinen A. J., Salonen J., Hirvonen J. T. and Santos H. A. Copperfree azide-alkyne cycloaddition of targeting peptides to porous silicon nanoparticles for intracellular drug uptake, *Biomaterials*, 2014, 35, 1257-1266.
14. Santos H. A. and Hirvonen J. Nanostructured porous silicon materials: potential candidates for improving drug delivery, *Nanomedicine*, 2012, 7, 1281–4.
15. Paulis L, Mandal S., Kreutz M. and Figdor C. Dendritic cell-based nanovaccines for cancer immunotherapy, *Curr. Opin. Immunol.* 2013, 25, 389-395.
16. Chang-Fang W., Mäkilä E. M., Bonduelle C., Rytönen J., Raula J., Almeida S., Närvänen A., Salonen J., Lecommandoux S., Hirvonen J. T. and Santos H. A. Functionalization of Alkyne-Terminated Thermally Hydrocarbonized Porous Silicon Nanoparticles with Targeting Peptides, *ACS Appl. Mater. Interfaces*, 2015, 7, 2006–2015.
17. Salonen J., Laitinen L., Kaukonen A., Tuura J., Björkqvist M., Heikkilä T., Vähä-Heikkilä K., Hirvonen J. and Lehto V. P. Mesoporous silicon microparticles for oral drug delivery: Loading and release of five model drugs', *Journal of Controlled Release*, 2005, 108, 362–374.
18. Maniya N. H., Patel S. R. and Murthy Z. V. P. Development and in vitro evaluation of acyclovir delivery system using nanostructured porous silicon carriers. *Chemical engineering research and design*, 2015, 104, 551–557.
19. Hamidi M., Azadi A. and Rafiei P. Hydrogel nanoparticles in drug delivery *Adv. Drug Deliv. Rev.*, 2008, 60, 1638–1649.
20. Wang X., Chi N. and Tang X. Preparation of estradiol chitosan nanoparticles for improving nasal absorption and brain targeting. *European Journal of Pharmaceutics and Biopharmaceutics*. 2008, 70, 735–740.

21. Andersen T., Bleher S., Flaten G. E., Tho I., Mattsson S. and Škalko-Basnet N. Chitosan in Mucoadhesive Drug Delivery: Focus on Local Vaginal Therapy. *Mar Drugs*. 2015, 13, 222–236.
22. Wang X., Zheng C., Wu Z., Teng C., Zhang X., Wang Z. and Li C. Chitosan-NAC Nanoparticles as a Vehicle for Nasal Absorption Enhancement of Insulin. *Journal of Biomedical Materials Research Part B: Applied Biomaterials*. 2009.
23. Tamilselvan N. and Raghavan C. V. Formulation and characterization of anti-alzheimer's drug loaded chitosan nanoparticles and its In vitro biological evaluation. *Journal of Young Pharmacists*. 2015,7.
24. Dasha M., Chiellini F., Ottenbrite R. M. and Chiellini E. Chitosan—A versatile semi-synthetic polymer in biomedical applications. *Progress in Polymer Science*. 2011, 36, 981-1014.
25. Md S., Khan R. A., Mustafa G., Chuttani K., Baboota S., Sahni J. K. and Ali J. Bromocriptine loaded chitosan nanoparticles intended for direct nose to brain delivery: Pharmacodynamic, Pharmacokinetic and Scintigraphy study in mice model. *European Journal of Pharmaceutical Sciences*, 2013, 48, 393–405.
26. Vazzana M., Andreani T., Fanguero J., Faggio C., Silva C., Santini A., Garcia M. L. Silva A. M. and Souto E. B. Tramadol hydrochloride: Pharmacokinetics, pharmacodynamics, adverse side effects, co-administration of drugs and new drug delivery systems. *Biomedicine & Pharmacotherapy*, 2015, 70, 234-238.
27. McCarberg B. Tramadol extended-release in the management of chronic pain, *Ther. Clin. Risk Manage*. 2007, 3, 401.
28. Brvar N., Mateovic-Rojnik T. and Grabnar I. Population pharmacokinetic modelling of tramadol using inverse Gaussian function for the assessment of drug absorption from prolonged and immediate release formulations. *International Journal of Pharmaceutics*. 2014, 473, 170–178.

2. JUSTIFICATION

Based on the advantageous properties of biodegradability, biocompatibility and mucoadhesiveness of the designed composites (UnPSip/CH and TOPSip-OH/A/G/CH), the option of developing new hybrid materials as transport and delivery vehicles for therapeutic agents. In this way, by modifying the synthesis parameters of the composites, the physicochemical and morphological properties can be modulated that allow control of the release, improve the bioavailability and efficacy of the therapeutic agents.

3. HYPOTHESIS

Functional PSip/chitosan composites designed with careful control of their particle size and pore size, surface chemistry, shape, and porosity, impregnated with tramadol will be able to act as sustained release systems. The biodegradability, biocompatibility and mucoadhesive properties of the composites will allow a safe and sustained release of tramadol and will ensure greater permanence and permeability of tramadol at the target site. In addition, using the PSip will increase the adsorption of tramadol and will have a double control of release, from inside the PSip and through the chitosan chain.

4. GENERAL OBJECTIVE

Design, synthesize and characterize last generation functional composites based on nanostructured PSip/chitosan and evaluate their potential application as transport and release vehicles for tramadol.

5. SPECIFIC OBJECTIVES

- Determine the synthesis protocol to obtain PSip and determine the effect of the synthesis parameters on morphology, porosity, particle size and pore size.

- Synthesize and determine the methodology for obtaining and functionalizing the PSip, with the different reagents (thermal oxidation, APTES-GTA, UA), and optimizing the factors that intervene and directly modify the size (pore and particle), thickness and porosity of the PSip.
- Determine the morphological and physicochemical properties of PSip, using characterization techniques such as HRSEM, HRTEM, FTIR, etc.
- Determine the protocol to perform the loading of tramadol in PSip, evaluate the loading percentage, and determine the in vitro release kinetics by simulating the local environment of the gastrointestinal system.
- To evaluate the TOPSip-OH / TR nanostructured composites in carrageenan-induced hyperalgesia and edema models.
- Optimize the APTES functionalization of PSip parameters.
- Incorporate the chitosan to the PSip by chemical binding using APTES-GTA and UA as bridges and establish the synthesis methodology.
- Determine the morphological and physicochemical properties of the UnPSip/CH and TOPSip-OH/A/G/CH composites, using characterization techniques such as HRSEM, HRTEM, FTIR, etc.
- Evaluate the mucoadhesive properties of the UnPSip/CH and TOPSip-OH/A/G/CH composites by mucin adsorption.
- Evaluate the percentage of tramadol loading in the composites and monitor the release kinetics in vitro simulating the gastrointestinal system.
- Obtain the in vitro release kinetics modeling of PSip and composites.

CHAPTER 1

Porous silicon microparticles as nanovehicles for the sustained release of tramadol: Kinetic, physicochemical and biological evaluation

Cándida A. Cisneros-Covarrubias, César F. A. Gómez-Durán, Patricia Aguirre-Bañuelos, Rosa Alejandra Hernández-Esquivel, Gabriela Palestino.

ABSTRACT

Thermally oxidized porous silicon particles (TOPSip) have been widely studied as drug delivery systems for sustained release. In this work, TOPSip with different particle and pore sizes were synthesized by electrochemical etching and used as vehicles for the transport and sustained administration of tramadol hydrochloride (TR), a centrally acting opiate analgesic. The physicochemical and morphological properties of nanostructured TOPSip were fully characterized by Fourier transform infrared spectrometry (ATR-FTIR), transmission electron microscopy (TEM), scanning electron microscopy (SEM), and zeta potential techniques. TOPSip showed particle sizes from 0.8 to 31 μm and pore sizes from 6 to 67 nm. TR loading capacity in TOPSip-OH was quantified by UV-Vis spectroscopy, high pore size dependence of TOPSip-OH was observed. TOPSip-OH with pore size \sim 6 nm exhibited a TR loading capacity of 10%, whereas TOPSip-OH with 67 nm pore size shown an increase in loading capacity of tramadol up to 31%. TR release was carefully studied in simulated gastric fluid (pH 1.2) and simulated intestinal fluid (pH 6.8). TR released profiles demonstrated that TOPSip-OH with \sim 6 nm pore size exhibited a sustained release up to 24 h with burst effect depending on pH. Release profiles of TOPSip-OH were compared with the release profile of a commercial extended-release tramadol formulation (CERF) in both pHs. It was observed that CERF released TR quickly and entirely at 1 h. TR cumulative release data were fitted using different mathematical models. Korsmeyer-Peppas was the most appropriate model adjusted for both simulated fluids: gastric and intestinal. Through in vivo assessment, it was demonstrated that TR-loaded TOPSip sustains antinociceptive and anti-inflammatory effects compared to administration of tramadol at the same dose, which is a novel contribution of this work.

Keywords: Porous silicon microparticles, Tramadol, Drug release, Inflammation, Nociception, Commercial tramadol formulation.

1. INTRODUCTION

Sustained drug delivery systems are extensively explored to solve problems such as low in vivo stability, poor solubility, and inefficient intracellular delivery. These systems' main objective is to improve drug performance, increase drug action, decrease dose required and dosing frequency, and most importantly, reduce side effects. In recent years, an alternative widely studied is developing micro and nanocarriers, which improve mobility in biological systems and enhance delivery in the site of interest. Several micro-nano systems have been designed and used based on inorganic, organic, or composites micro-nano particles. Since the 50's decade, porous silicon (PSi) particles have been investigated owing to their numerous applications in sensors and biosensors [1–6], biomolecular screening [7], and drug delivery [8–20]. Their exciting properties, such as biodegradability [21,22] and high loading capacity for therapeutics [21], highlighted them as a recognized micro-nanocarrier for drug-delivery application. Nanostructured PSi possesses pores that act as reservoirs for drug loading. The amount of therapeutic able to load depends on particle size, pore size, and porosity. Several groups have studied these properties by modifying various synthesis conditions [23–28]. Although several processes have been reported to synthesize PSi particles, electrochemical etching of crystalline silicon wafers is the most used due to its flexibility to manipulate pore size and porosity [26, 29].

The current density and etching time can be easily manipulated during the electrochemical process, allowing a simple way to modify the PSi nanostructure. Studies on current density variation have been made showing a reasonable control of pore size [26]. Additionally, hydrofluoric acid (HF) concentration combined with current density offers increasing linear porosity to high current density [21,22]. In addition, different alcohols have been used for electrolyte solutions and have shown an effect on pore size and directly affected the pore growth process [23,27,28].

Moreover, the perforations method introduced by Qin et al. [27] has remarkably contributed to obtaining size homogeneity in PSi particulate material. The method

consists of applying periodically high current pulses (for a few seconds) during the electrochemical etching process. This action introduces cleavage sites parallel (perforations) to the wafer face [27]. As the method for producing PSi particles is top-down assisted by ultrasound, the perforations help break the PSi porous film more controllably. The particle thickness depends on the perforations' frequency. Many perforations usually produce smallest particle sizes. Thus, the number of perforations created during the material synthesis depends on the particle size desired, which, most of the time, also depends on the material application. However, for this method to be successful, a careful selection of the synthesis parameters must be made.

For drug loading, having reasonable control of porosity and pore size is essential because they determine the material loading capacity. Therefore, in the work we present here, a careful study was made to determine the optimal synthesis parameters to obtain porous silicon particles with suitable morphology to construct a drug delivery microcarrier. Tramadol (TR), a potent analgesic used for muscle and joint pain was used as the model drug. TR in oral administration has a short half-life (6-8 h). Thus, a slow delivery vehicle is desirable to improve drug absorption and drug performance. Besides, a drug-delivery system could decrease TR administration's frequency and its side effects, such as respiratory depression and addiction [28,30]. Previous works have reported TR nano and microcarriers with good drug release profiles. These composites are based on alginate-chitosan microcapsules [28], proteins [31], polycaprolactone [32] and cellulose [33] for mention some. Our group previously reported two microcarriers based on gelatin-citric acid hydrogel [34] and gelatin PSi crosslinked composites [19]. Although these delivery systems offer good release kinetics, in vivo studies are still missing. Additionally, they require polymers coverage or protein substrates such as albumin zein or egg albumin that once are absorbed and metabolized trigger the drug release [31]. However, that involve various steps and, in some cases, complicated synthesis procedures to obtain the delivery vehicle and reach the reported drug release profiles.

Thus, we offer a most straightforward alternative in our work by selecting an appropriate morphology of bare porous silicon particles to control drug dosage. A systematic study of the experimental conditions that revealed the impact of synthesis parameters in particle size, pore size, and particle dimensions was performed. Electrolyte ratio, current density, ultrasonication time, and perforations number were evaluated based on drug loading and release kinetics profiles. Particle dimensions were tuned by introducing perforations, which increased the ability to control TR release kinetics. In vitro studies demonstrated that extended drug dosage might be reached by engineering particle pore size and dimension. On the other hand, in vivo studies were conducted, denoting the therapeutic effect of TR-TOPSiP microcarriers for the first time. The anti-inflammatory and nociceptive activity were determined, which constitutes a novel contribution of this work.

2. MATERIALS AND METHODS

2.1 Materials

Single-crystal boron-doped p-type Si wafers with a resistivity between 0-0.005 Ω cm and $\langle 100 \rangle$ crystallographic orientation were purchased from WRS materials. Absolute ethanol (EtOH, 95.5 %) and aqueous hydrofluoric acid (HF, 48 %) were acquired from Monfel Industries (Mexico) and Golden Bell Chemicals (Mexico), respectively. Sulfuric acid (H_2SO_4 , 98 %) and hydrogen peroxide (H_2O_2 , 30 %) were purchased from Karal (Mexico) and Avantor (Mexico). Tramadol hydrochloride (TR, 99 %) and λ -carrageenan type IV were supplied from Sigma-Aldrich (Mexico) and used without further treatment.

2.2 General procedure for the synthesis of PSi layers

PSi layers were prepared from boron-doped, p⁺⁺-type, single-crystal Si wafers with resistivity < 0.005 Ω cm ($\langle 100 \rangle$ -oriented) by an electrochemical etching process. The electrolyte was composed of 3:7 (v/v) solution of HF (48%) and absolute EtOH. Si

wafers were placed into a Teflon etching cell (exposed area 9.6 cm^2) (Fig. 1). The cell's inner volume was filled with the electrolyte solution (10 mL), and the desired current densities were applied to the system. After etching, the PSi layers were rinsed three times with EtOH to remove the excess of HF and lifted off via an electropolishing step using ten pulses of 184 mA/cm^2 for five seconds. The PSi free-standing films were maintained in absolute EtOH to avoid natural aging.

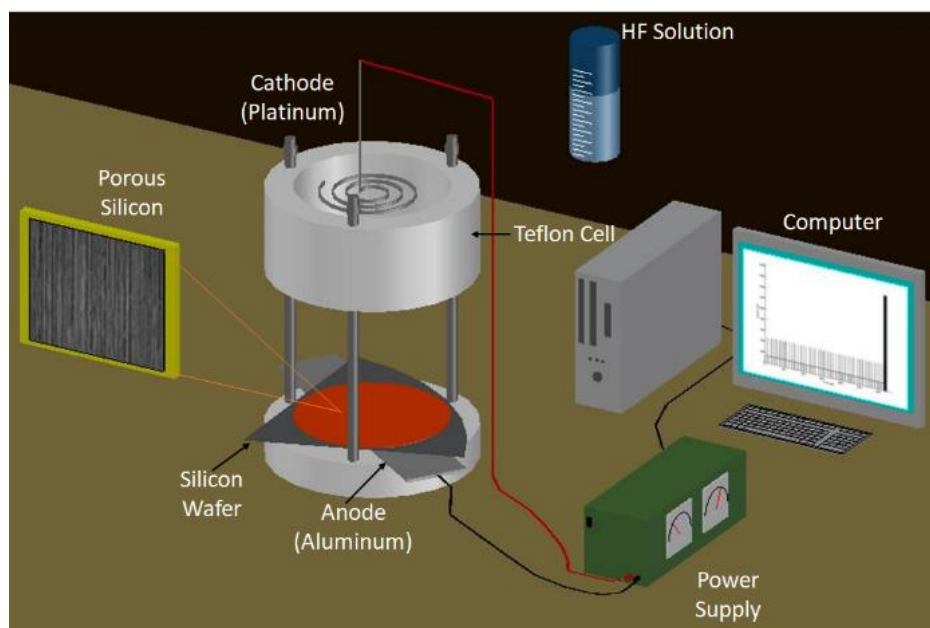


Fig. 1. Schematic representation of the electrochemical etched cell used in the PSi synthesis.

PSi layers were obtained following two different procedures (Table 1). 1) The traditional method, by applying a constant current density (15 or 17 mA/cm^2) for a controlled etching time (3016 or 2578 s respectively) (Fig. 2A,B), and 2) the perforation method by introducing cleavage points parallel to the wafer's face. In this procedure, high current pulses (50 mA/cm^2 for 3 s) were applied periodically after the primary layer (low current) according to the number of perforations desired (Fig. 2C-F) [27].

2.3 Fabrication of P*Si* microparticles

P*Si* microparticles were obtained by using an ultrasonic tip (30% amplitude, SONICS Vibra-Cell VCX-750), the free-standing P*Si* films were shaken (Fig. 2) in fresh EtOH for 15, 30 or 60 minutes. Afterward, P*Si* microparticles were stabilized by thermal oxidation (TOP*Si*p). A Carbolite furnace (model STF 15/-/180) was used, the samples were heated for 45 minutes with a ramp rate of 10 °C/min, at 450 °C under ambient air.

The impact of synthesis parameters on particle size, pore size, and porosity was determined and evaluated. Hence, P*Si* films with different architectures were obtained according to the parameters shown in table 1.

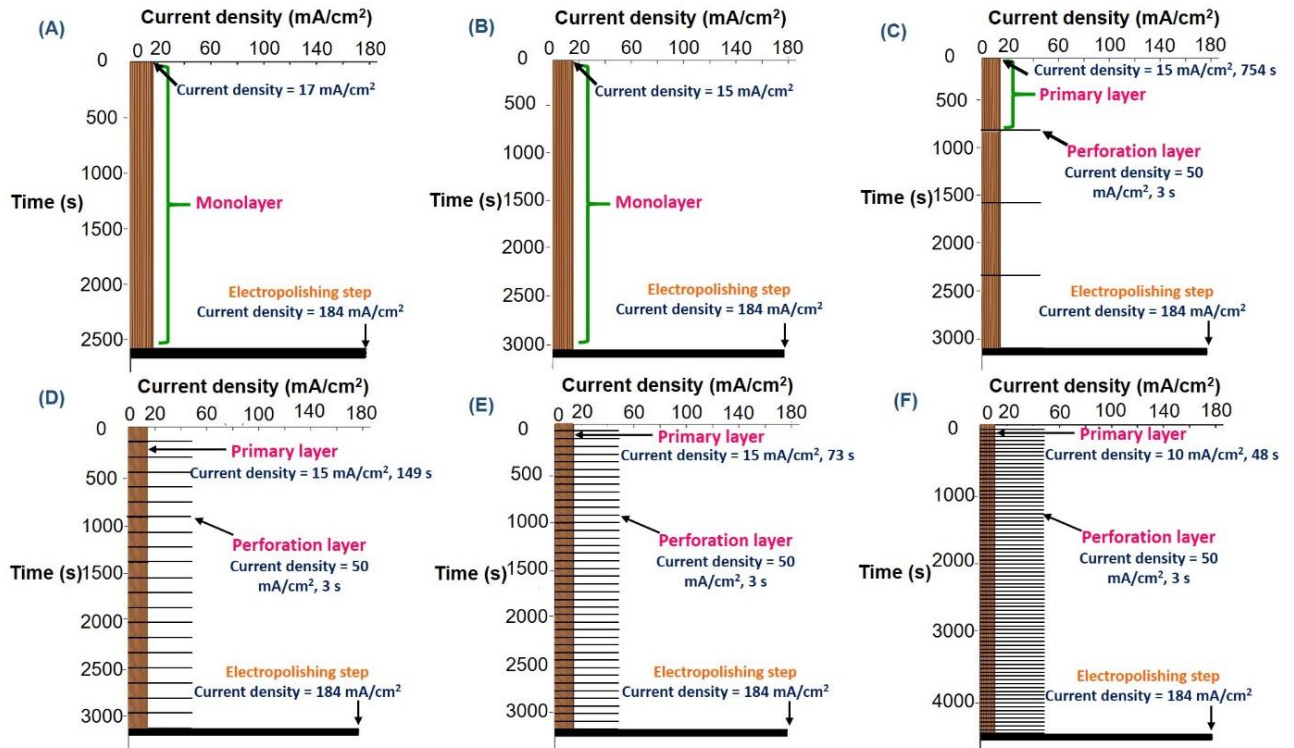


Fig. 2. Schematic representation of free-standing P*Si* layers showing the different architectures. Single monolayers etched at (A) 17 mA/cm² for 2578 s, and (B) 15 mA/cm² for 3016 s. Multilayers formed by perforation method, the primary layer was obtained at 15 mA/cm² at the following etching times (C) 754, (D) 149, and (E) 73 s. (F) primary layer obtained at applying a current density of 10 mA/cm² for 48 s.

According to the design, perforations were produced periodically by applying a current pulse of 50 mA/cm² for 3 s after each primary layer.

Table 1. Experimental conditions for preparation of porous silicon particles.

Sample	Material architecture	Electrolyte HF/EtOH	Current density (mA/cm ²)	Etching time (s)	Ultrasonication time (s)
TOPSip _{M1}	Monolayer	3:7	17	2578	
TOPSip _{M2}	Monolayer	3:1		3016	
TOPSip ₋₄	Multilayer (4 cycles)			3016 (754/cycle)	900
TOPSip ₋₂₀	Multilayer (20 cycles)		15	3016 (149/cycle)	
TOPSip ₋₄₀	Multilayer (40 cycles)	3:7		3016 (73/cycle)	3600
TOPSip ₋₈₀	Multilayer (80 cycles)		10	4057 (48/cycle)	

2.4 TR loading and quantification in TOPSip

TR loading was carried out by modifying the TOPSip surface chemistry through the hydroxylation method. Thus, 15 mg of each set of microparticles were placed in separated vials and dispersed in 3 mL of piranha solution (H₂SO₄/H₂O₂ in the volume ratio of 1:1.6). The suspensions were allowed to react for 60 minutes. Afterward, the TOPSip-OH suspensions were centrifuged at 5500 rpm for 10 minutes, and the supernatant was removed. The hydroxylated microparticles were rinsed several times with deionized water to remove the reactants excess (H₂SO₄/H₂O₂).

TR loading was carried out by the immersion method (Fig. 3). 15 mg of each set of TOPSip-OH were mixed with 3 mL of TR aqueous solution (25 mg/mL). The suspensions were stirred using an orbital shaker at 130 rpm until reaching equilibrium

(at least 24 h). Finally, TOPSip-OH/TR microparticles were centrifuged at 4000 rpm for 2 minutes and rinsed two times with deionized water and acetone. Wet particles were dried in the oven at 60 °C overnight, without further treatment. TR adsorption on the TOPSip-OH surface and pores was promoted by intermolecular interactions between surface TOPSip-OH groups (SiO^- , Si-OH) and the functional groups of TR ($-\text{OH}$, $-\text{NHR}_3^{+-}$) (Fig. 3).

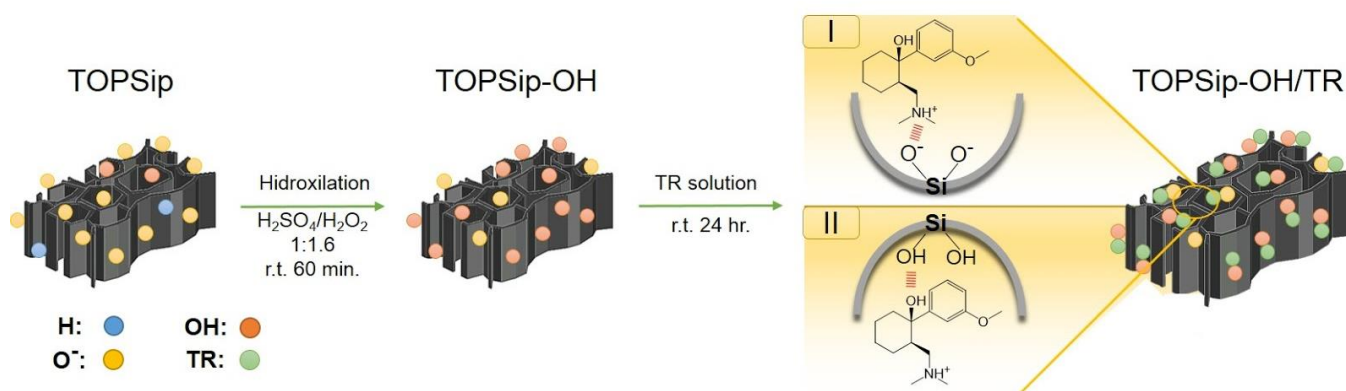


Fig. 3. Scheme of TOPSip hydroxylation and TR loading into TOPSip-OH by immersion method.

Quantification of TR loaded into TOPSip-OH was obtained by UV-Vis spectroscopy (Cary 60 UV-Vis). For the analysis, loaded TOPSip-OH were prepared as mentioned in section 2.3. TR molecules diffused from impregnation solution into TOPSip-OH pores during the loading process, reducing the supernatant's concentration. TR no specific binding was removed by rinsing and centrifugation. Then, the TOPSip-OH/TR (2 mg) composites were placed in 1 mL of KOH (2M) solution. Under these conditions, the hydroxide ions degrade TOPSip-OH materials producing a soluble form of silicon, orthosilicic acid ($\text{Si}(\text{OH})_4$) [36, 37]. This product has not absorption in the UV-Vis spectrum. Once TOPSip-OH is degraded, TR diffuses into the KOH solution. TR concentration was measured using a calibration curve in the range

from 50 to 1000 ppm ($R^2 = 0.9988$), at 271 nm (maximum absorption of TR) [37,38]. The percentage of TR loaded was calculated using Eq. 1 [39–41].

$$\text{Loading capacity (\%)} = \frac{\text{Amount of drug (mg)}}{\text{Amount of drug (mg)} + \text{Amount TOPSip-OH (mg)}} \times 100 \quad 1$$

2.5 In vitro TR release

TR release profiles were performed by dispersing 2 mg of each set of TOPSip-OH/TR in 0.5 mL of KCl/HCl buffered solution (pH 1.2) or acetates buffered solution (pH 6.8) under sink conditions at $37 \text{ }^\circ\text{C} \pm 2 \text{ }^\circ\text{C}$, simulating the TR process desorption in the human organism. A buffered solution with TOPSip-OH/TR was centrifuged at 12,000 rpm to separate the released TR from TOPSip-OH microparticles, and sampled aliquots at each selected time interval from the supernatant (0.4 mL) were collected. The concentration of the released TR was measured spectrophotometrically (Agilent Technologies, Cary 60 UV–Vis) at 271 nm (maximum absorption of TR) using external standard calibration curves in both buffered solutions in the 5 to 100 ppm ($R^2 = 0.999$) range. Based on the sink conditions protocol, aliquots were replaced with fresh buffer (0.4 mL) after measurement. The percentage of drug release was calculated by applying Eq. 2 [19].

$$\text{TR released (\%)} = \frac{M_t}{M_0} \times 100 \quad 2$$

where M_t is the amount of drug released at any time (t) and M_0 is the total mass of TR loaded into TOPSi-OH.

2.6 Physicochemical characterization of TOPSip

2.6.1 High-resolution scanning electron microscopy (HR-SEM)

HRSEM micrographs of TOPSip layers (top and cross-sectional views) were obtained using a field emission microscope (Dual Beam FIB/SEM FEI-Helios Nanolab

600) at accelerating voltage of 5 keV and 86 pA with a spot size of 4.0 mm. Backscattered and secondary electrons were used at 200, 6000, 50000, 100000, and 150000 × magnification.

2.6.2 High-resolution transmission electron microscopy (HR-TEM)

TOPSip micrographs were obtained using an HRTEM/STEM JEOL JEM-2100 microscope operated with acceleration voltage at 200 kV and resolution of 0.14 nm at 20000, 30000, and 40000 × magnification.

2.6.3 Fourier transform infrared spectrometry (ATR-FTIR)

Attenuated total reflectance Fourier transform infrared (ATR-FTIR) spectroscopy was used to characterize the functional groups on the PSi films in all the modification steps and before and after TR loading. Agilent Cary 600 Series FTIR instrument equipped with a Slide-On diamond ATR device were used to record the spectra. The recording was performed with a resolution of 4 cm⁻¹, 32 scans, in an interval of 4000 and 500 cm⁻¹, and at room temperature.

2.6.4 Zeta (ζ)-potential

Stability and the surface zeta potential distribution (ζ -potential) were measured as a function of pH using electrophoretic light scattering (ELS) on a Zetasizer Nano ZS (Malvern Instruments), before and after TR loading (TOPSip-OH/TR) and as a reference TOPSip-OH. Isoelectric point (IEP) from TOPSip, TOPSip-OH, and TOPSip-OH/TR was determined in the pH value where potential shows a zero value (neutral charge). ζ -potential measurements were carried out in different vials, 2 mg of each set of microparticles and 1 mL of the desired buffer solution were added: pH 1 (KCl/HCl), pH 3 (acetates), pH 7 (phosphates), and pH 9 (borax/HCl). All suspensions were strongly mixed, using an ultrasonic bath (Branson) for 20 minutes to disperse the

particles, and 4 hours later, the supernatants of each vial were measured. Isoelectric point analysis was carried out at room temperature; measurements were acquired in triplicate for each sample.

2.6.5 Gravimetric analysis

The porosity of PSi layers was determined by gravimetric analysis applying Eq. 3. In this equation, m_1 is the weight of the Si substrate before the electrochemical etching, m_2 after porous layer formation, and m_3 after porous layer total removal by dissolution in KOH (2 M aqueous solution) [13].

$$Porosity (\%) = \frac{m_1 - m_2}{m_1 - m_3} \quad 3$$

2.6.6 Statistical analysis

All values are reported as the mean \pm standard deviation of the mean from at least three independent experiments.

2.7 In vivo assessment

2.7.1 Animals

Male Wistar (330 g) rats were obtained from Harlan, Mexico, and were housed in plastic cages in a temperature-controlled room (22 °C), with a 12-h light/dark cycle. The animals had free access to food and tap water up to the time of the experiment. Each rat was used only once and euthanized by carbon dioxide inhalation at the end of the test. All procedures were conducted in accordance with the "Guidelines on Ethical Standards for Investigation of Experimental Pain in Animals" [42] and approved by the ethical committee of Medicine School of University Autonomous of San Luis Potosí (BGF MUASLP-09-02).

2.7.2 Treatments

Animals were randomly allocated in six experimental groups (n = 4) according to the following treatments: a) control saline, b) bare TOPSip-OH, c) TR (3.3 mg/Kg), d) TR (13.5 mg/Kg), and two TOPSip-OH/TR composites loaded with e) 3.3 mg TR/Kg (TOPSip-OH/TR_{M2}) and f) 13.5 mg/Kg (TOPSip-OH/TR₋₄₀). All treatments were diluted with saline 0.9% and administered orally (1 mL/Kg).

2.7.3 Assessment of inflammation

Inflammation was evaluated using the carrageenan-induced paw edema test according to the method of Winter [43]. Paw edema was induced in rats by injection of 100 µL of carrageenan 0.1% in the left hind foot paw. Paw thickness was determined using a digital caliper at 0, 2, 4, 6, 8, and 12 h. Anti-inflammation response data were evidenced as the statistical difference in the area under the curve of thickness vs. time, compared with control or the selected treatment.

2.7.4 Assessment of mechanical nociception

Mechanical stimulus was measured as the paw's withdrawal force threshold in rats with carrageenan-induced edema, as previously described by Vergnolle [44], at 0, 2, 4, 6, 8, and 12 hours. Mechanical antinociception response was defined as the difference between the area under the curve of threshold vs. time in treated animals and compared to the control.

3. RESULTS AND DISCUSSIONS

3.1 Morphological characterization of TOPSi_p

The batches of thermally oxidized PSi microparticles were morphologically characterized by scanning electron microscopy. Fig. 4 shows the cross-sectional images of various PSi monolayers and multilayers obtained varying the synthesis parameters (current density, electrolyte ratio, or perforations number). Fig. 4A,B shows the monolayers obtained at 17 and 15 mA/cm² and 3:7 and 3:1 HF:EtOH ratio, respectively. These parameters were established to obtain single monolayers with differences in pore sizes and particle thicknesses. It is well known that variations in the electrolyte concentration induce drastic changes in porous films' morphology. This was confirmed by synthesizing single monolayers at 15 and 17 mA/cm² while maintaining invariant the electrolyte ratio (3:7); as expected, the pore size and thickness had no significant differences (results not shown). Thus, PSi microparticles with greater thickness and smaller pore sizes were obtained by using 3:1 HF:EtOH electrolyte (Fig. 4B) [45].

HR-SEM images showing a lateral view of primary and perforated layers built periodically throughout the PSi multilayers are displayed in Fig. 4C-F. The PSi multilayers showed a total thickness of ~20 μm that agrees with the theoretically calculated value. The thickness of the primary porous layers was determined by the number of perforations made along the PSi structure. Thus, samples with 4, 20, 40, and 80 perforations produced primary layers with thicknesses of 5.62, 0.99, 0.5, and 0.25 μm. In all cases, straight and uniform pores randomly distributed on the surface in the crystallographic direction <100> are observed, suggesting the formation of not interconnected pores.

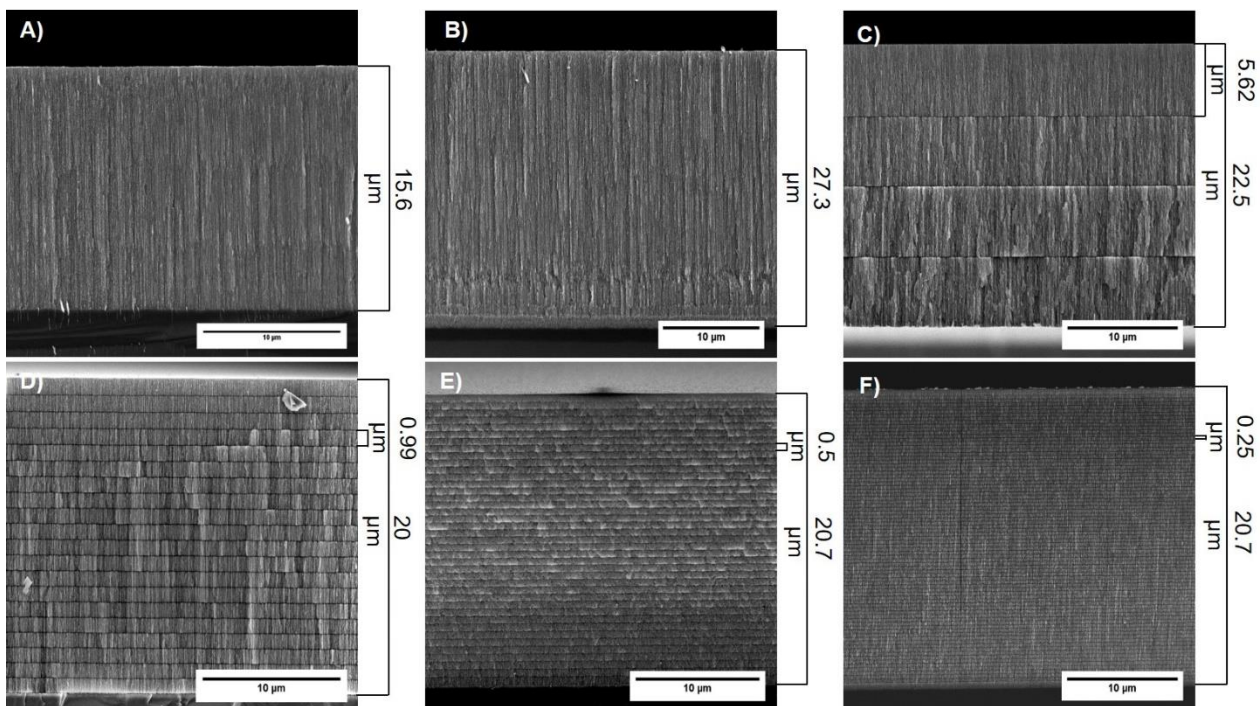


Fig. 4. Cross-sectional HRSEM images of thermally oxidized PSi layers. Single monolayers etched at (A) 17 mA/cm^2 for 2578 s (TOPSip_{M1}), and (B) 15 mA/cm^2 for 3016 s (TOPSip_{M2}). Multilayers formed by perforation method, the primary layer was produced using 15 mA/cm^2 current density at the following etching times (C) 754 s (TOPSip-4), (D) 149 s (TOPSip-20), and (E) 73 s (TOPSip-40). (F) Multilayer with a primary layer obtained at applying 10 mA/cm^2 current density for 48 s. After each primary layer, perforations were made by applying a current pulse of 50 mA/cm^2 for 3 s. The applied current density was periodically varied between these two values generating a total of 4, 20, 40, and 80 perforations for samples (C) to (F), respectively.

PSi microparticles were obtained following the ultrasonic fracture method. Hence, morphological characterization of TOPSip nanostructures was obtained by selected HR-SEM micrographs. ImageJ software (National Institutes of Health [NIH], Bethesda, MD, USA) was used to obtain the needed data. Average size, thickness, and pore dimensions were calculated, measuring at least 150 PSi microparticles

randomly selected in the images. Porosity was determined from gravimetric measurements.

Fig. A,B shows that TOPSip particles obtained by ultrasonic fracture of single monolayers (TOPSip_{M1}, TOPSip_{M2}, Table 2) display irregular shape and particle size similar to that observed in the attached monolayer (Fig. 4A,B). These results indicate that the porous films' ultrasonic fracture was predominantly carried out along the pore growth axis ($\langle 100 \rangle$). This method produced randomized shape and high dimensions PSi microparticles. The effect of electrolyte concentration in pore sizes dimension was confirmed in Fig. 5G,H (top view images), which respectively correspond to 3:7 (TOPSip_{M1}) and 3:1 (TOPSip_{M2}) HF:EtOH ratio. It is observed that a lower amount of ethanol in the electrochemical etching solution drastically reduces the pore sizes (6 ± 1.1 nm, Table 2) and the porosity of PSi particles (Fig. 5H). This effect is due to the lack of surface wettability. A high concentration of HF produced a fast electrochemical etching limited to a single site on the surface of crystalline silicon. This low spread of HF produces tiny and deep pores (Table 2). Likewise, the porosity also decreases.

On the other hand, TOPSip particles obtained by the perforation method showed more homogeneity and smaller particle size. The addition of periodical high current density pulses (perforations) as film fracture points allowed us to have better particle size control and smaller size microparticles than those prepared using a single monolayer [27]. The accuracy of the method was confirmed by systematically increasing the number of perforations. From HR-SEM images (Fig. 5C-F), it was observed that TOPSip microparticles size is perforation-number dependent. When increasing the number of perforations, the particle size decreased. Furthermore, TOPSip microparticles' thicknesses (see Table 2) was in good agreement with those of the primary porous layers observed in the undetached PSi samples (Fig 4C-F). These results confirmed that the inclusion of perforation in the PSi layers significantly improves the homogeneity of TOPSip [27]. It is also important to mention that the porosity of the TOPSip remained constant when they are etched at the same electrolyte ratio.

On the other hand, it was found that microparticle pore size is perforations number linear-dependent (Fig. 5I-L, Table 2). This behavior is probably produced by the high current density used to produce the cleavage layers. The high current density might promote a higher rate of electrochemical etching, which causes the enlargement and fusion of the pores, producing pores with irregular shape and pores coalescence (Fig. 5K,L) [25,46]. This effect widens pore sizes (standard deviation) and limited the number of perforations made during the synthesis. In our case, under the reported parameters, the maximum number of perforations was 80; for a greater number, the porous film was broken during the electrochemical etching procedure. TOPSip-80 prepared with 80 perforations showed the smallest particle size ($0.8 \pm 0.01 \mu\text{m}$) and medium pore size (32 ± 15) (Table 2).

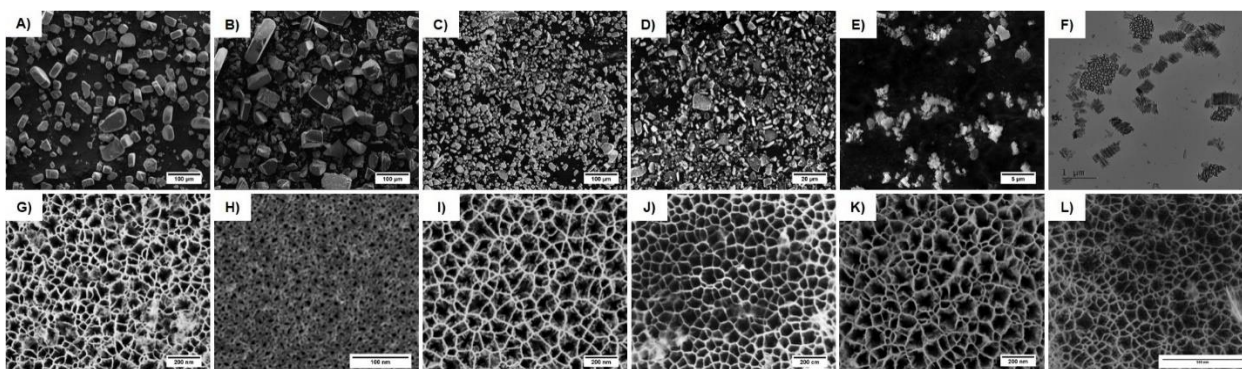


Fig. 5. HR-SEM and HR-TEM micrographs showing particle size, thickness, and pore dimensions of TOPSip microparticles. Single-layers: (A,G) TOPSip_{M1} and (B,H) TOPSip_{M2}. Perforated layers: (C,I) TOPSip-4, (D,J) TOPSip-20, (E,K) TOPSip-40, and (F,L)TOPSip-80.

Table 2. Particle size, thickness, pore size, and porosity of TOPSip microparticles

Sample	Average particle size (μm)	Thickness (μm)	Average pore size (nm)	Porosity (%)
TOPSip _{M1}	31 \pm 8.5	15 \pm 3	57 \pm 11.5	86 \pm 3
TOPSip _{M2}	31 \pm 12	27 \pm 7	6 \pm 1.1	57 \pm 1.3
TOPSip-4	21 \pm 7	4 \pm 0.8	48 \pm 13	87 \pm 3
TOPSip-20	5 \pm 1.5	1 \pm 0.2	52 \pm 12.5	
TOPSip-40	1 \pm 0.31	0.5 \pm 0.08	67 \pm 17	
TOPSip-80	0.8 \pm 0.01	0.22 \pm 0.05	32 \pm 15	89 \pm 2.5

3.2 FT-IR of TOPSip-OH pre-TR-loading and post-TR-loading

TR loading on TOPSip was determined by Attenuated Total Reflectance Fourier Transform Infrared Spectroscopy (ATR-FTIR). This technique was also used to confirm chemical modifications on TOPSip surface after each step. As shown in Fig. 6A, pure TR displays a strong and sharp absorption band at 3305 cm^{-1} assigned to $\nu(\text{O-H})$ and at 702 cm^{-1} due to $\delta(\text{OH})$. The absorption band located at 1477 cm^{-1} is attributed to $\delta(\text{CH}_3)$, while the band centered at 1288 and 1240 cm^{-1} corresponded to $\nu(\text{C-N})$ and $\nu(\text{CO})$, respectively. The IR spectrum of TR also shows a group of bands attributed to the presence of aromatic compounds: 3065 cm^{-1} and 1576 cm^{-1} $\nu(\text{C-H})$, 2929 and 2860 cm^{-1} $\nu(\text{C-H})$, and 1606 cm^{-1} $\nu(\text{C=C})$ [47–49].

On the other hand, TOPSip IR spectrum displays a strong band at 1060 cm^{-1} , characteristic of siloxane groups $\nu(\text{Si-O-Si})$, confirming the PSi microparticles surface's thermal oxidation. The shoulder located at 1184 cm^{-1} indicates oxygen as a suboxide species. Absorption bands located at 2165 and 2183 cm^{-1} are assigned to $\nu(\text{O}_y\text{SiH}_x)$ species. The PSi microparticles hydroxylation (TOPSip-OH) was confirmed by the presence of the 3389 cm^{-1} absorption band, characteristic of $\nu(\text{O-H})$ (Fig. 6B) [16]. Figure 6C shows IR spectrum of TR-loaded TOPSip-OH microparticles on which

distinctive bands attributed to TR functional groups are observed, confirming TOPSip-OH/TR surface attachment.

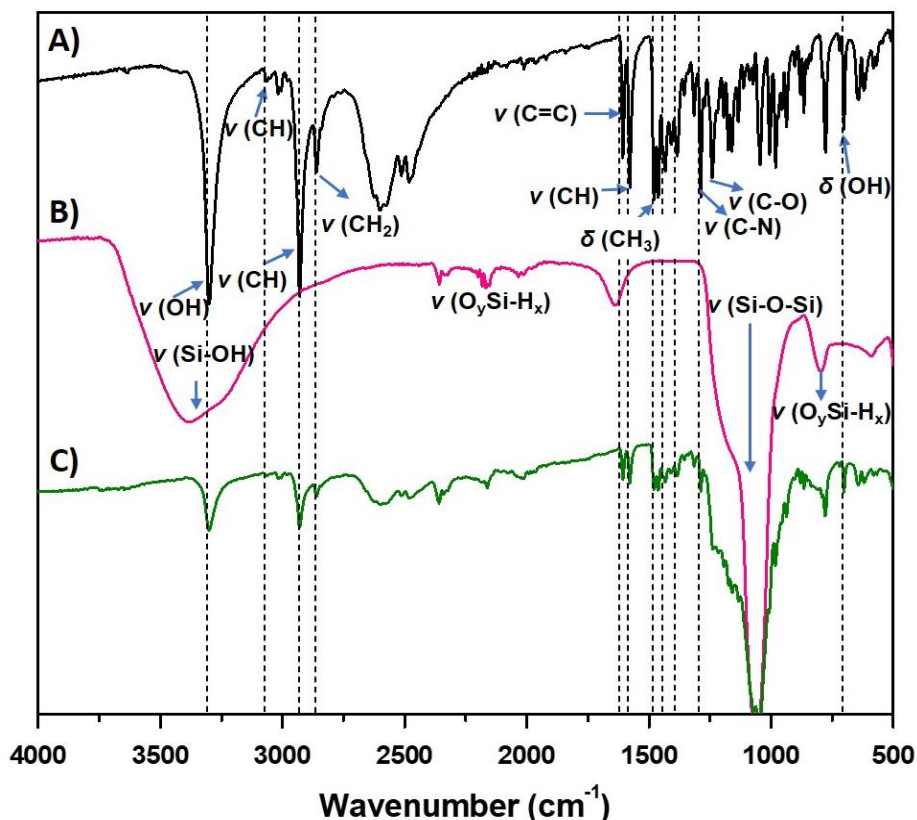


Fig. 6. ATR-FTIR spectra of (A) TR, (B) TOPSip-OH and (C) TOPSip-OH/TR.

3.3 TR loading on TOPSip-OH

The capability of TOPSip-OH to physically adsorb TR was evaluated as a function of pore dimensions. Table 3 shows the calculated drug loading percentages. All microparticles adsorbed TR, which confirms the excellent interaction between functional groups of PSi substrate and the therapeutic. It is noticed that TOPSip-OH pore size has a strong effect on the amount of TR loaded into the microparticle. Among the six TOPSip-OH samples that were evaluated, microparticles obtained by the single-layer method without perforations (TOPSip-OH_{M2}) and 3:1 HF:EtOH ratio produced the lowest TR loading. This is attributed to the small pore size (6 ± 1.1) and low porosity

(57 ± 1.3 %) of the sample that limits the infiltration of TR molecules [50]. TOPSip-OH_{M2} pore size is only ~ 5.5 times larger than the TR molecules ($X = 10.83$, $Y = 9.26$ and $Z = 6.75$ Å), TR overall volume is 255.47 Å³ [19].

Fig. 7 displays the % of TR loaded as a function of microparticles pore size. When the pore size increases, the loaded amount of TR becomes higher. The highest drug loading was found in TOPSip-OH_{B3} and TOPSip-OH_{M1} microparticles, which is attributed to their large pore size. The increasing pore size improves TR molecular diffusion and, for consequence, the molecular binding on pore walls, which resulted in a better drug packing efficiency [40,51]. These findings agree with previous studies reported for other porous materials like mesoporous silica nanoparticles [52–54]. In addition, it is observed that TOPSip-OH_{B1} and TOPSip-OH_{B2} showed close drug loading capacity, which is attributed to pore size similarity.

Table 3. TR loading as a function of TOPSip-OH pore size.

Sample	Average pore size (nm)	TR loading (%)
TOPSip-OH _{M1}	57 ± 11.5	29 ± 2.5
TOPSip-OH _{M2}	6 ± 1.1	10.4 ± 2.5
TOPSip-OH-4	48 ± 13	21.3 ± 0.7
TOPSip-OH-20	52 ± 12.5	23.6 ± 6
TOPSip-OH-40	67 ± 17	31.3 ± 4.8
TOPSip-OH-80	32 ± 15	18.3 ± 2.4

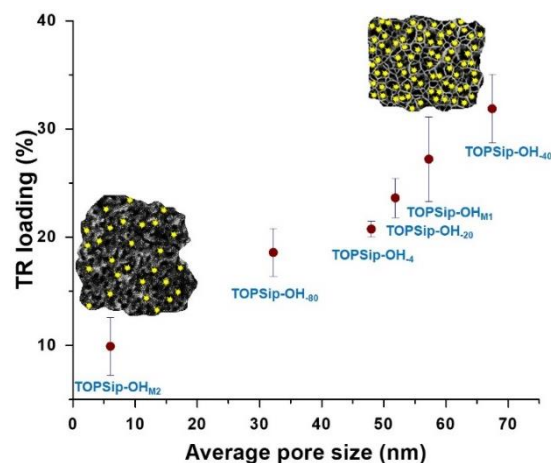


Fig. 7. TR loading as a function of the pore size of the TOPSip-OH.

3.4 ζ -potential analysis

ζ -potential is a useful method for verify surface functionality or stability of dispersed particles. Therefore, information on the surface charge of materials can be obtained using ζ -potential analysis [55]. For drug loading and release, ζ value is useful for determining optimal pH conditions that facilitate drug-particle interactions. Hence, the surface charge and stability of TOPSip-OH as a function of pH were studied before and after TR loading. TR adsorption on TOPSip-OH surface was promoted by intermolecular interactions between surface TOPSip-OH groups (SiO^- , Si-OH) and TR functional groups ($-\text{OH}$, $-\text{NHR}_3^+$) [19]. Fig. 8 shows TR speciation diagram (pKa values 9.41 and 13.1) [37]. It can be observed that pH below 9.41 provides a positively charged molecule, mainly due to the tertiary amine protonation. Between $9.41 < \text{pH} < 13.1$, neutral TR molecule predominates, and above pH 13.1, hydroxyl dissociation is promoted, providing a negatively charged molecule.

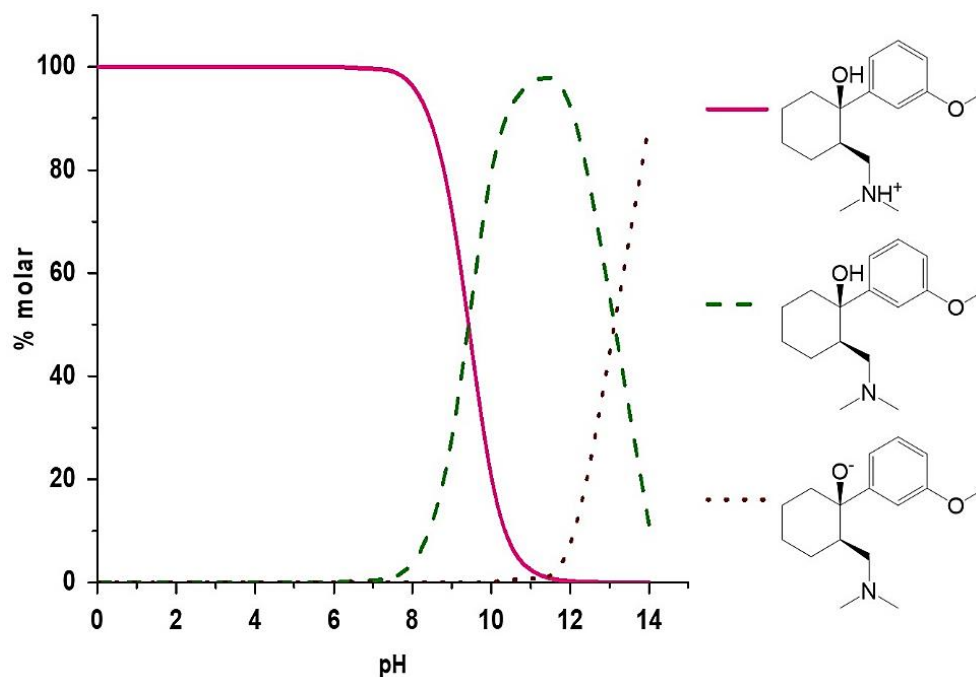


Fig. 8. Speciation diagram of TR.

The ζ -potential characteristic curves and the isoelectric point (IEP) of TOPSip-OH microparticles before and after TR adsorption are displayed in Fig. 9. The IEP of unmodified TOPSip-OH was found at 2.1, in agreement with previous reports [56–58]. The curve indicates the presence of different dissociated species. Si-OH_2^+ species are found below pH 2.1, whereas Si-O^- species predominate above this value. TOPSip-OH are negative in almost all the studied pH range [16]. After TR loading in TOPSip-OH, IEP shifted to higher values, IP = 3 for the sample TOPSip-OH-40 and IP = 2.4 for the sample TOPSip-OH/TR_{M2}. This effect is attributed to the physical adsorption of therapeutic molecules by intermolecular bonds (ion-ion electrostatic forces and hydrogen-bonding) among the silanol (Si-OH) and siloxane groups (SiO^-) of TOPSip and hydroxyl (OH) or protonated tertiary amine ($\text{R-NH}^+(\text{CH}_3)_2$) groups of TR molecule.

However, it is possible to notice that throughout the studied pH, the TOPSip-OH/TR ζ -potential curves of composites corresponding to the highest (TOPSip-OH/TR_{B3}) and lowest (TOPSip-OH/TR_{M2}) drug loading showed significant differences from each other (Fig. 9). It is well known that ζ -potential can be used to determine if drug-loaded is encapsulated within the particle or on the surface. Thus, if the drug is mainly infiltrated into the pores, the ζ -potential would be close to ζ -potential of bare particles [59–61]. Based on this information, the higher ζ -potential observed in the composite with bigger TR loading (structure with larger pores) is attributed to TR molecules that are found over TOPSip-OH surface besides being located inside the pores. In contrast, TOPSip-OH/TR_{M2} characterized for its tiny pores and low TR loading capacity, showed a ζ -potential curve similar to that of bare TOPSip-OH, indicating that TR molecules are predominantly into the pores [62].

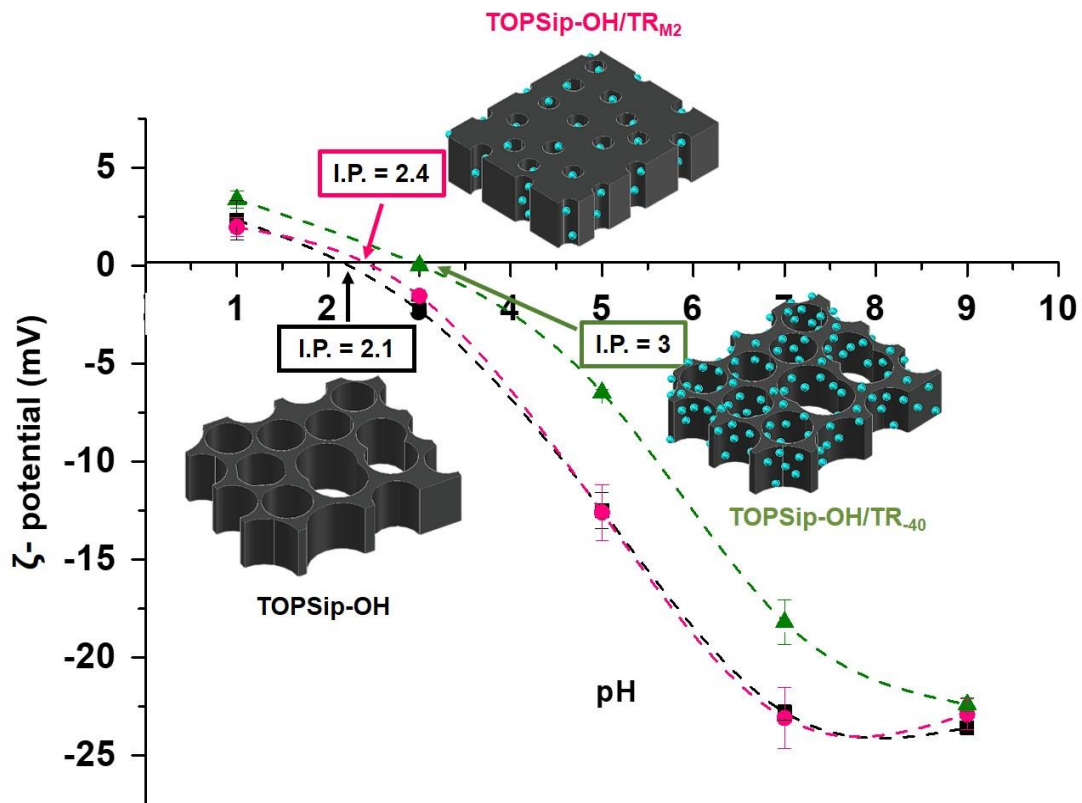


Fig. 9. ζ -potential curve vs pH for TOPSip-OH (black line) and TOPSip-OH/TR with different TR load; TOPSip-OH/TR_{M2} (pink line) and TOPSip-OH/TR₄₀ (green line).

3.5 In vitro TR release study

The TR in vitro cumulative release profiles from TOPSip-OH and a commercial extended-release formulation were evaluated in simulated gastric fluid (SGF, pH 1.2) and simulated intestinal fluid (SIF, pH 6.8) at 37 °C, under sink conditions. The TR release kinetics was evaluated for 24 h, samples from the supernatant were taken at different intervals of time. Results are shown in Fig. 10A,B. The cumulative release profiles of CERF (taken as reference) in both media showed a strong burst effect during the first 30 min and a low capacity to induce TR-controlled release. In both media, 100 % of the drug was released in ~3 h.

The inspection of TOPSip-OH/TR composites shows more sustained and controlled TR release profiles (over 24 h) compared to CERF in both simulated fluids. TOPSip-OH/TR composites in SGF behave similarly, releasing by burst effect, approximately 53–80 % of TR during the first 30 min. The highest and lowest burst effect was observed in TOPSip-OH/TR₄₀ (80 %) and TOPSip-OH/TR_{M2} (53 %). Initial burst release from PSi composites can be explained in terms of microparticles stability and low binding affinity between TOPSip surface and TR in strong acid media. As observed in TR speciation diagram (Fig. 8), TR molecule has a positive charge in acid media, while TOPSip are quite unstable (2 mV) and positively charged due to the protonation of silanol (Si-OH) groups [16]. Therefore, at pH 1.2 (SGF), the PSi functional groups reverse their charge, producing TR's spontaneous desorption, mainly due to electrostatic force repulsion. However, after 30 min, the TOPSip-OH/TR composites showed a sustained and more controlled drug delivery up to 24 h. The cumulative release kinetics of TOPSip composites showed different profiles depending on microparticle pore size. The material with the largest pore dimensions (TOPSip-OH₄₀) showed a faster drug release than the smallest one (TOPSip-OH_{M2}), indicating that a good control in pore size is enough to reduce the TR delivery rate, even in circumstances where the repulsion forces dominate. In this case, the drug release kinetics mechanism is governed by the molecular diffusion through the pores. Quite different behavior was observed when changing the pH of the medium. In SIF (pH 6.8), the burst effect is lower (35 - 63 %), attributed to greater stability of TOPSip-OH in this medium and a higher binding affinity between TR and microparticles surface. In SIF (pH 6.8), TR has a positive charge, and TOPSip-OH are negatively charged due to siloxane groups (SiO⁻). Therefore intermolecular forces between TOPSip-OH surface and TR are favored, leading to more negligible TR desorption [16]. It is possible that under these conditions, the overall mechanism of desorption involves the combined contributions of attractive electrostatic forces and molecular diffusion through the pores. This action is beneficial in an oral administration because, in a painful situation, it is necessary to have a high drug dose at the initial time to mitigate the pain, and then a sustained-release treatment to sustain the effective concentration of TR in the blood.

TR release at a fixed time (3.5 h) was evaluated in SGF and SIF, as a thickness and pore size function. The results are presented in Fig. 10C,D respectively. They have observed some tendencies; for instance, large pore size and small particle thickness let to faster release rate. Other authors have already observed this behavior in acrylic acid and methacrylic acid copolymer [63] particles, mesoporous silica nanoparticles [64–66], PLGA microspheres [67], among others.

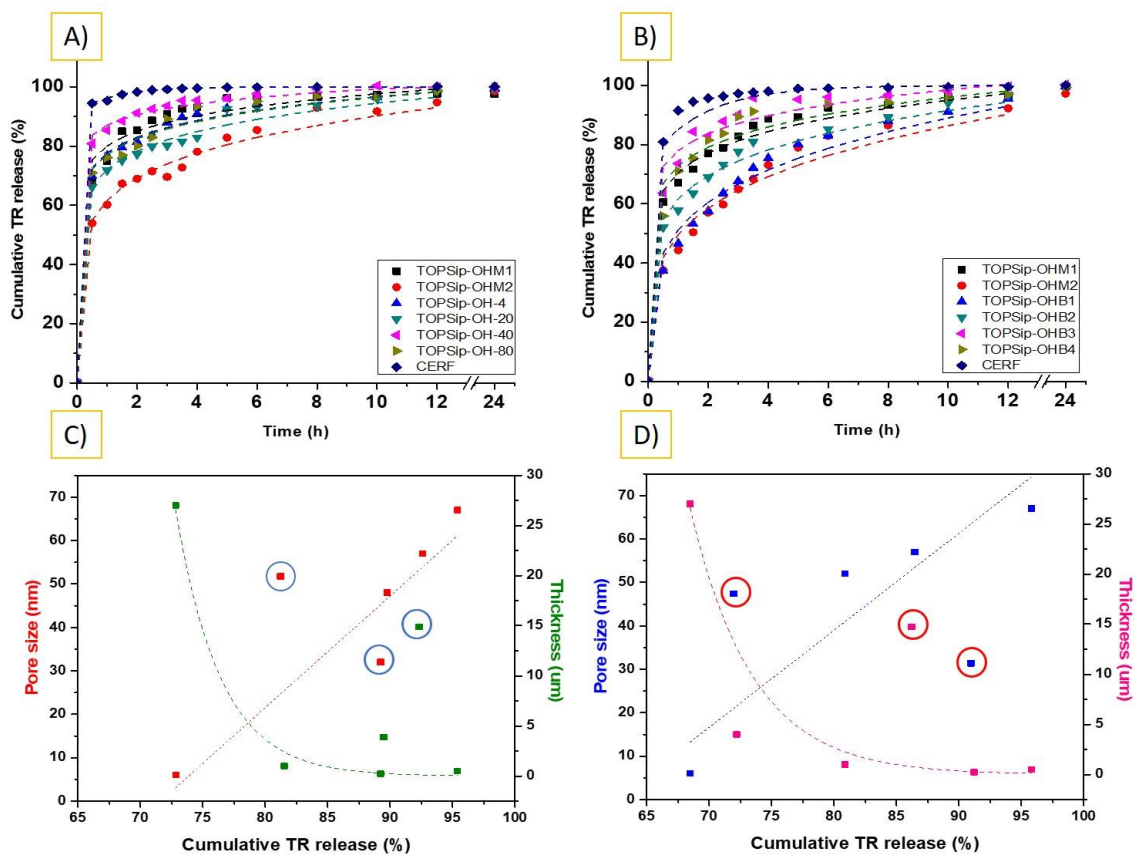


Fig. 10. In vitro release profiles of 1) Commercial extended-release formulation of TR and 2) TOPSip-OH/TR with different particle thickness and pore size at 37 °C in A) Simulated gastric fluid (pH 1.2) and B) Simulated intestinal fluid (pH 6.8). Cumulative release of TR as a function of the particle thickness and pore size of the TOPSip-OH; C) Simulated gastric fluid (pH 1.2) and D) Simulated intestinal fluid (pH 6.8). Overlaid contour at out-of-trend experimental points.

TOPSip-OH/TR_{M2} composite showed the slowest release rate, which can be a consequence of the porous material's small pore size that makes difficult the solvent's diffusion into the pores and the counter-diffusion of the drug toward the solution (Fig. 11A). On the other hand, the faster release rate observed in TOPSip-OH/TR₄₀ composite is attributed to the higher diffusion rate of the SGF solution into the pore. This effect is promoted by the large pore size of nanostructured material (~ 11 times greater than TOPSip-OH_{M2}) and the short diffusion distance needed to reach the SGF solution. This fast diffusion phenomenon is determined by microparticle pore length, which in turn is related to particle thickness (Fig. 11B), that for these two materials are 27 ± 7 (TOPSip-OH/TR_{M2}) and 0.5 ± 0.08 μm (TOPSip-OH₄₀), which confirms the contribution of molecular diffusion through the pores.

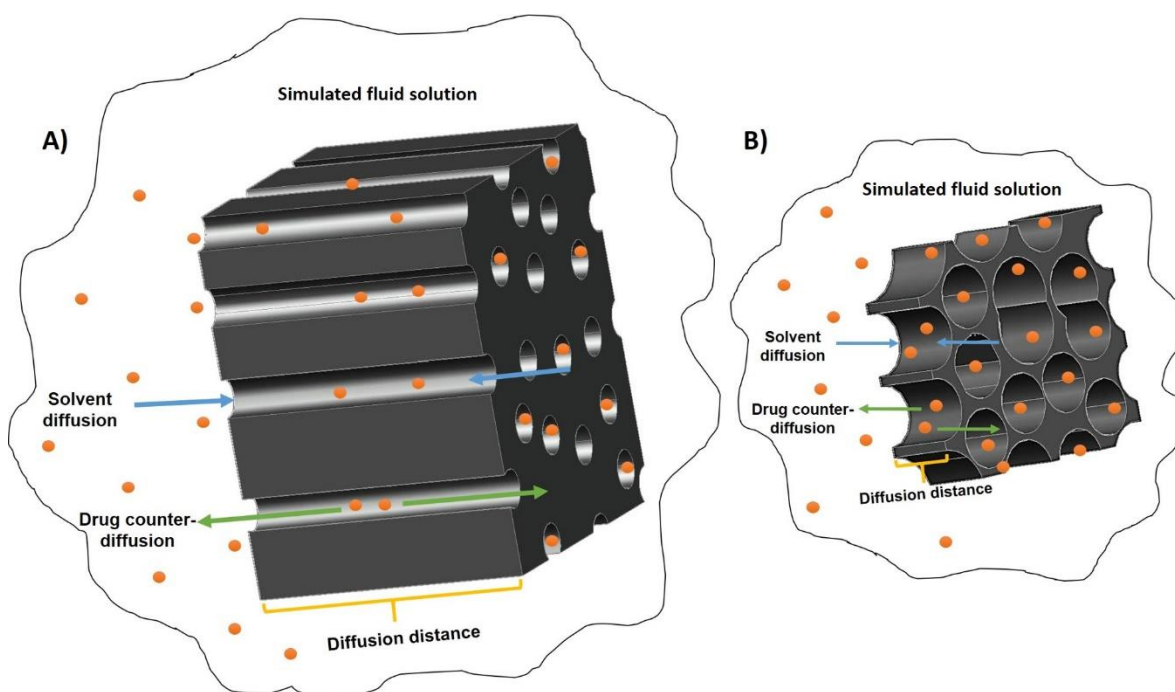


Fig. 11. Diffusion of the simulated fluid into the pores and counter-diffusion of the TR toward the solution in A) TOPSip-OH_{M2}: pore size 6 ± 1.1 nm, thickness 27 ± 7 μm , and B) TOPSip-OH₄₀: pore size 67 ± 7 , thickness 0.5 ± 0.08 μm . The TR molecules size is $X = 10.83$, $Y = 9.26$ and $Z = 6.75$ \AA , with 255.47 \AA^3 overall volume [19].

Oral administration of TR is not considered ideal because it is released spontaneously in the stomach. So, alternatives to reduce its fast dissolution are needed to increase its therapeutic effect. Hence, the P*Si* microcarriers might help to produce a better drug dosage. As discussed above TR release kinetics depends on P*Si* microparticle morphology. For instance, TOP*Si*p-OH₄₀, with the largest pore size, can easily allow TR diffusion and molecular adsorption increasing the amount of drug absorbed in the porous nanostructures. However, it does not guarantee an efficient cumulative release profile because TR release rate is fast. Therefore, the pore size of the microcarrier should be optimized according to molecule dimensions. Another option is TOP*Si*p-OH_{M2} vehicle which showed the smallest pore size. These pore dimensions seem to be good enough to allow drug molecule encapsulation. These custom-made pores improve drug kinetics release. TR dosage over 24 h was reached using this microcarrier with spontaneous release in SGF of 37 %, which is low compared with those observed in previous reports.

TR high solubility in water induces the major difficulty to increase the drug loading percentage. Hence, to solve this problem, some authors have developed and studied complex TR delivery systems [47,48,68–71]. Table 4 shows some TR delivery systems reported in the literature. It is observed that some delivery systems showed fast TR releases ≤ 12 h under the same release conditions used in this work (sink conditions). However, others showed prolonged and sustained releases up to 1080 h. Although these results are promising, unfortunately, most of these studies do not perform *in vivo* studies, and for a real application, it is needed to demonstrate the TR microcarrier therapeutic effect. In this regard, this work introduces a simple alternative using biodegradable and biocompatible P*Si* vehicles that allow a sustained TR dosage. The advantage is that the TOP*Si*p vehicles showed better drug release performance than the prolonged-release systems commercially available. Even some burst effect is observed. The composites are still promising if the drug release profiles can be efficiently optimized by coating or encapsulating them with a biopolymeric matrix. Thus, the burst effect can be decreased, and the release kinetics extended (> 24 h), as demonstrated previously in our research group [19].

Table 4. TR delivery systems

Structure	Composition	Drug loading (%)	Loading efficiency (%)	Release conditions	Release time (h) (Drug released percentage)	Ref.
Bulk tablets	Ethyl cellulose (EC)	68	Not mentioned	Sink conditions	12 (99.7)	[72]
	Hydroxypropyl cellulose (HPC), EC, HPMC K100, chitosan combinations	Not mentioned	98-99	Sink conditions	8 (90 - 97)	[73]
Nanoparticles	Poly (lactic-co-glycolic acid) (PLGA)	Not mentioned	71 - 73	Not mentioned	120 (70)	[74]
	Protein blends of egg albumin and zein	Not mentioned	67 - 74	Volume reposition	48 (77 – 85)	[31]
Microspheres	Ethyl cellulose (EC)	Not mentioned	12 - 31	Volume reposition	8 (66 – 99)	[75]
Hydrogels	Poly (ethylene glycol) diamine (PEGD) and gelatin (GEL)	Not mentioned	Not mentioned	Volume reposition	10 (60)	[34]
Ribbons	Poli (ϵ -caprolactona) (PCL)	Not mentioned	85 - 97	Not mentioned	1080 (48 - 94)	[32]
Hydrogels	Gelatin (GEL) - Porous silicon particles (PSip)	Not mentioned	100	Volume reposition	28 (98)	[19]

3.6 TR release kinetics modeling

The drug release mechanism for TOPSip-OH/TR composites was determined in SGF (pH 1.2) and SIF (pH 6.8). Hence, cumulative release data were fitted using different mathematical models, such as zero and first-order kinetics, Higuchi [76,77], Korsmeyer-Peppas [78,79], and Hixon-Crowell [80] models. For both simulated fluids the data fitted well for the Korsmeyer-Peppas model, in agreement with previous studies on which it was used for modeling different drugs adsorbed on micro/nano PSi

particles [78,79]. This model is generally applied when there is more than one mechanism governing the drug release profile (Eq. 4) [81].

$$\frac{M_t}{M_\infty} = k_{K-P} t^n \quad 4$$

In this mathematical expression, M_t/M_∞ is the fraction of drug released at time t , k_{K-P} is the Korsmeyer-Peppas kinetic release constant that incorporates the structural and geometrical characteristics of the release form. The n is the diffusional exponent describing the drug release mechanism [82,83]. The release mechanism is determined according to the following values: $n \leq 0.5$ for Fickian diffusion, $0.5 < n < 1$ for anomalous transport, and $n = 1$ for a zero-order [84].

Cumulative release kinetic parameters and regression coefficients calculated from Korsmeyer-Peppas model for SGF are listed in Table 3. TOPSip-OH/TR-40 composite shows the highest k_{K-P} value (0.87 ± 0.008), confirming the faster TR release attributed to the short and wide pore channels of the PSi structure, on which there is no hindrance for TR diffusion towards the SGF solution. In TOPSip-OH/TR-4, TOPSip-OH/TR-20, TOPSip-OH/TR-80, and TOPSip-OH/TR_{M1} composites, similar k_{K-P} values in the range of 0.72 ± 0.011 to 0.80 ± 0.017 were obtained. The combination of pore size and particle size in these composites does not show significant differences in release rate. The lowest k_{K-P} value (0.61 ± 0.012) was obtained for TOPSip-OH/TR_{M2}, which might be a consequence of the pore size's drastic decrease. The n values for all TOPSip-OH/TR composites were found < 0.5 suggesting a mechanism controlled by Fickian diffusion, which is mainly governed by the TR concentration gradient.

On the other hand, for SIF, the cumulative release kinetic parameters and regression coefficients calculated from the Korsmeyer-Peppas model for SIF are presented in Table 3. At comparing the release rate constants (k_{K-P}) of TOPSip-OH/TR composites, it was observed that the lowest and highest k_F values were found for TOPSip-OH/TR_{M2} (0.49 ± 0.019) and TOPSip-OH/TR-40 (0.78 ± 0.02). TOPSip-OH/TR-4, TOPSip-OH/TR-20, TOPSip-OH/TR-80, and TOPSip-OH/TR_{M1} showed close k_F values.

All these results agree with those explained above. Finally, these results suggest that the TR release rate can be controlled by varying the pore size and particle size of TOPSip-OH. However, although the Korsmeyer-Peppas model determined that the mechanism that controls TR release is Fickian diffusion, there are other factors that delay TR diffusion in both simulated fluids. Some of these factors are hydrodynamic and interactions between the diffusing TR, the pore wall, and the functional groups present in the pore wall, the structural defects of the PSip, and the possible desorption-adsorption of TR in the pore channels until diffusing to the buffered solution.

Table 5. Kinetic parameters of the TOPSip-OH/TR_{M1}, TOPSip-OH/TR_{M2}, TOPSip-OH/TR₋₄, TOPSip-OH/TR₋₂₀, TOPSip-OH/TR₋₄₀, TOPSip-OH/TR₋₈₀ at 37 °C and pH 1.2.

Kinetic parameters	TOPSip-OH/TR _{M1}	TOPSip-OH/TR _{M2}	TOPSip-OH/TR ₋₄	TOPSip-OH/TR ₋₂₀	TOPSip-OH/TR ₋₄₀	TOPSip-OH/TR ₋₈₀
SGF						
k	0.80 ± 0.017	0.61 ± 0.012	0.77 ± 0.01	0.72 ± 0.011	0.87 ± 0.008	0.77 ± 0.013
n	0.08 ± 0.012	0.16 ± 0.01	0.09 ± 0.007	0.11 ± 0.008	0.05 ± 0.005	0.09 ± 0.009
R ²	0.97	0.98	0.99	0.98	0.99	0.98
SIF						
k	0.70 ± 0.013	0.49 ± 0.019	0.51 ± 0.017	0.61 ± 0.014	0.78 ± 0.02	0.72 ± 0.022
n	0.13 ± 0.01	0.24 ± 0.019	0.24 ± 0.017	0.17 ± 0.011	0.10 ± 0.013	0.12 ± 0.016
R ²	0.98	0.96	0.97	0.98	0.97	0.96

3.7 In vivo assessment

The *in vitro* release studies were strengthened by conducting *in vivo studies*. TOPSip-OH composites with the highest (TOPSip-OH/₋₄₀) and lowest (TOPSip-OH_{M2}) tramadol loading were orally administered to selected groups of rats according to the

protocol described in section 2.6. The overall doses were 3.3 and 13.5 mg/kg, respectively. These studies aimed to determine tramadol-loaded TOPSip-OH composites' influence as a delivery vehicle to inhibit the nociceptive (analgesic) and inflammatory effect in an acute inflammatory model of pain edema in rats.

3.7.1 Antinociceptive effect

The antinociceptive effects of TOPSip-OH/TR composites measured as the paw withdrawal force threshold in rats (g) are presented in Fig. 12. In the case of the withdrawal threshold by mechanical stimulation control, TOPSip-OH groups were not statistically significant at 12 h of observation. This result reveals that bare TOPSip-OH does not cause inhibition of the nociceptive effect. The antinociceptive effect was evident after the administration of pure TR and TOPSip-OH/TR composites. The results showed that the nociceptive threshold increased significantly for both composites compared with that observed in the control. It was observed that the analgesic effect was dose-dependent, producing a stronger antinociceptive effect with the 13.5 mg/kg ($p < 0.001$) dose compared to 3.3 mg/kg ($p < 0.01$). This behavior is in agreement with previous reports, on which it was observed that increasing the TR dose nociceptive activity is reduced [85,86]. The cumulative variable area under the curve of nociceptive threshold (Fig. 13) confirmed these findings.

Besides, throughout 12 hours of observation, it could be observed that the treatment with TOPSip-OH composites showed the most pronounced antinociceptive effect compared to the treatments with pure TR ($p < 0.05$ and $p < 0.0001$). During the entire period of evaluation, the most significant antinociceptive effect was observed with TOPSip-OH/TR₄₀ (13.5 mg/kg), suggesting that treatment with TOPSip-OH/TR composites improved the clinical efficacy of TR, which correlates with the pharmacokinetic behavior of this drug. TR is wholly absorbed in the intestine and undergoes hepatic first-pass metabolism [30,87]. It is metabolized into active metabolites, which improves tramadol's ability to modulate the response to pain. Therefore, after TR administration, it is rapidly and completely absorbed in the intestine.

After which, it metabolizes in M1 (its most potent metabolite), increasing its antinociceptive effect. However, both TR and M1 have short mean lifetimes in plasma (6.3 and 7.4 h, respectively) [88], and they are cleared from the body almost simultaneously.

In contrast, when TR is loaded into TOPSip-OH microparticles, it is released in a sustained manner for an extended period. Thus, just the fraction of TR-released is metabolized. As the drug release is constant over time, its metabolites remain in the blood plasma for a more extended period, strengthening the therapeutic effect compared with that observed when administrating TR alone. These results highlight the benefit of using TOPSip-OH microcarriers. In both cases, treatment with TOPSip-OH/TR_{M2} (3.3 mg/kg) and TOPSip-OH/TR₄₀ (13.5 mg/kg) showed a better antinociceptive effect than treatment with pure TR.

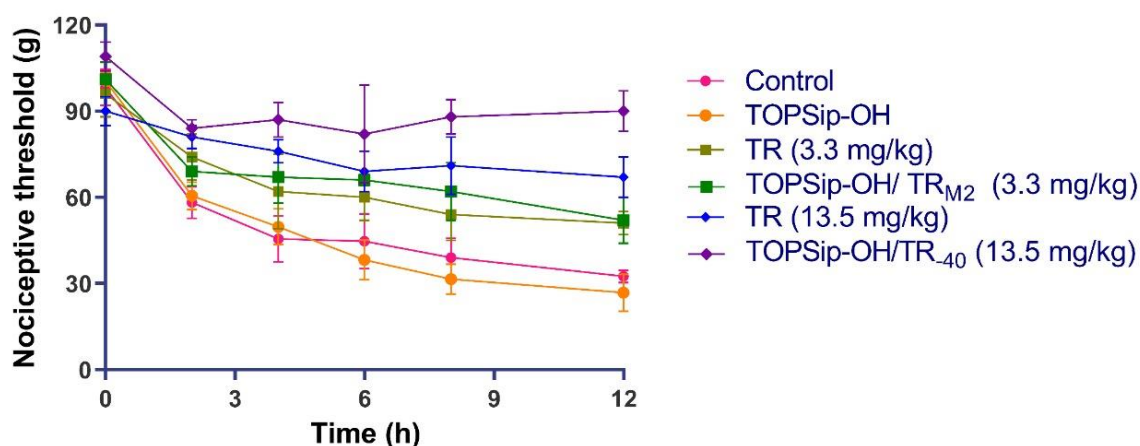


Fig. 12. Time-course of carrageenan-induced mechanical nociceptive threshold in animals receiving the treatments (data are shown as mean \pm standard deviation, n=4 rats per group).

both treatments with TR, it was observed that a higher concentration of TR (13.5 mg/kg) produced a more pronounced anti-inflammatory effect.

Furthermore, the administration of TOPSip-OH/TR_{M2} and TOPSip-OH/TR₄₀ composites having the same drug concentration (3.3 and 13.5 mg TR/kg rat), respectively, produced a more statistically significant reduction in paw thickness ($p < 0.01$ and $p < 0.0001$) compared to pure TR. It should be noted that the treatment with TOPSip-OH/TR₄₀ (13.5 mg / kg) was the most effective compared to the other treatments. Besides, after 12 h of inflammation induction, it was possible to recover the initial rat's paw thickness. The cumulative variable area under the curve of paw thickness (Fig. 15) confirmed these results.

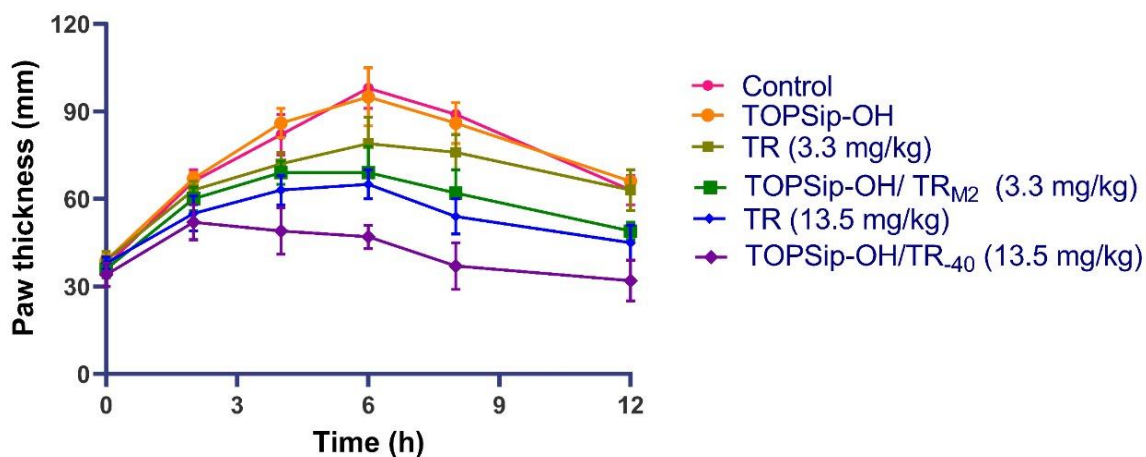


Fig. 14. The time course of carrageenan-induced inflammatory edema in animals receiving the treatments (data are shown as mean \pm standard deviation, $n=4$ rats per group).

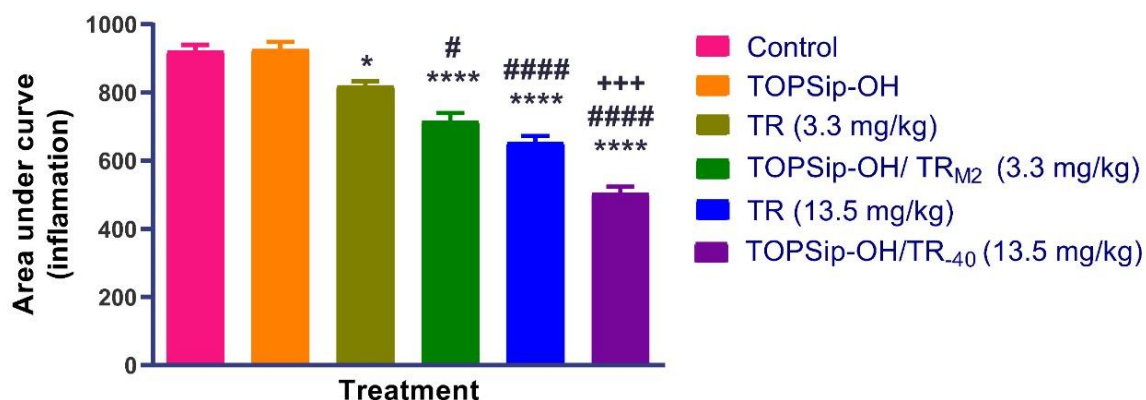


Fig. 15. Comparative effect of treatments in Inflammation measured as the paw thickness area under curve over 12 h period. Data are shown as mean \pm standard deviation (n=4 rats). Significance: *p < 0.05 and ****p < 0.0001 by comparison with the control and TOPSip-OH vs all groups. Significance: #p < 0.05, ####p < 0.01 and #####p < 0.0001 between TR 3.3 vs 13.5, TOPSip-OH 3.3, 13.5 and TR 13.5 vs TOPSip-OH 13.5. +++p < 0.001 between TOPSip-OH/TR 3.3 and 13.5.

4. CONCLUSIONS

In this study, thermally oxidized porous silicon microparticles (TOPSip) with different particle sizes and pore sizes were successfully synthesized. The synthesis parameters of the TOPSip played an essential role in the materials design. TOPSip with large particle sizes and small pore sizes were produced by using high concentration of HF relative to ethanol (3:1) and the ultrasonication (15 min) of monolayers. In contrast, TOPSip with smaller particle size and larger pore size were obtained using a low concentration of HF relative to ethanol (3:7) and the ultrasonication (60 min) of multilayers of 40 defects. TR loading capacity in TOPSip was mediated by pore dimension and intermolecular forces (ion-ion electrostatic forces and hydrogen bonding) created between the TR and the TOPSip inorganic surface. TOPSip with bigger pore size showed a higher TR loading capacity (31 %). The lowest

drug loading capacity (10 %) was found governed by particles pore size and solvent diffusion. Likewise, the *in vitro* TR cumulative release profiles were mediated by the particles pore size and solvent diffusion. TOPSip with smallest pore size and largest particle dimensions achieved a sustained TR release over 24 h in both simulated fluids (gastric and intestinal) with a non-significant burst effect compared to the rest of the TOPSip nanostructures. This sustained-release behavior was also related to TR molecules' encapsulation into the porous structure, which was confirmed by ζ -potential measurements. TR release was also mediated by pH. The TR sustained release was obtained in simulated intestinal fluid due to the high affinity between TR (positive charge) and TOPSip surface (negative charge) promoted in this physiological condition. The cumulative TR release kinetic parameters in simulated fluids were determined. It was found that TR transport is mainly controlled by drug concentration gradient (Fickian diffusion), however, there are other factors involved in the delay of diffusion such as structural defects of TOPSip and the possible desorption-adsorption of TR in the pore channels, among others. For the first time, *in vivo* evaluation using TOPSip microcarriers was performed, models of carrageenan-induced inflammation and withdrawal threshold by mechanical stimulation in rats were used. Evidence of better and sustainable antinociceptive and anti-inflammatory effects were obtained when using TR/TOPSip composites compared with TR alone. In addition, biological studies showed that the TOPSip did not cause any adverse effects in rats, suggesting that TR was metabolized correctly and eliminated from the rat body. There is evidence that TR/TOPSip composites made a synergic effect that improves the drug's anti-inflammatory and antinociceptive effect. It is essential to highlight that the use of TOPSip microcarrier improved the pharmacokinetic effect of TR. Treatment with TR/TOPSip composite at the lowest TR dosage increased the anti-inflammatory and antinociceptive effect compared to TR alone at its highest dose. These results suggest that efforts to design TOPSip microcarriers with reasonable particle size and pore size must be a significant advance in enhancing TR's pharmacokinetic effect.

REFERENCES

- [1] G. Palestino, V. Agarwal, R. Aulombard, C. Gergely, Biosensing and Protein Fluorescence Enhancement by Functionalized Porous Silicon Devices Biosensing and Protein Fluorescence Enhancement by Functionalized Porous Silicon Devices, (2008) 533–539. doi:10.1021/la8015707.
- [2] S. Dhanekar, S. Jain, Porous silicon biosensor: Current status, Biosens. Bioelectron. 41 (2013) 54–64. doi:10.1016/j.bios.2012.09.045.
- [3] M. De la Cruz-Guzman, A. Aguilar-Aguilar, L. Hernandez-Adame, A. Bañuelos-Frias, F.J. Medellín-Rodríguez, G. Palestino, A turn-on fluorescent solid-sensor for Hg(II) detection, Nanoscale Res. Lett. 9 (2014) 431. doi:10.1186/1556-276X-9-431.
- [4] M. De La Cruz-Guzman, A. Aguilar, A. Bañuelos-Frias, L.F. Chazaro-Ruiz, G. Palestino, Hybrid porous silicon-Rhodamine B derivative nanostructures as chemical sensor for hg(ii) detection., ECS Trans. 64 (2014) 31–34. doi:10.1149/06401.0031ecst.
- [5] B. Xia, W. Zhang, J. Shi, S. Xiao, Fluorescence quenching in luminescent porous silicon nanoparticles for the detection of intracellular Cu²⁺, Analyst. 138 (2013) 3629. doi:10.1039/c3an00503h.
- [6] J. Márquez, L.F. Cházaro-Ruiz, L. Zimányi, G. Palestino, Immobilization strategies and electrochemical evaluation of porous silicon based cytochrome c electrode, Electrochim. Acta. 140 (2014) 550–556. doi:10.1016/j.electacta.2014.05.065.
- [7] F. Cunin, T.A. Schmedake, J.R. Link, Y.Y. Li, J. Koh, S.N. Bhatia, M.J. Sailor, Biomolecular screening with encoded porous-silicon photonic crystals, Nat. Mater. 1 (2002) 39. <http://dx.doi.org/10.1038/nmat702>.
- [8] T. Kim, G.B. Braun, Z.G. She, S. Hussain, E. Ruoslahti, M.J. Sailor, Composite Porous Silicon-Silver Nanoparticles as Theranostic Antibacterial Agents, ACS Appl. Mater. Interfaces. 8 (2016) 30449–30457. doi:10.1021/acsami.6b09518.

- [9] R.-G. Denisse, G.-C. Antonio, R.-M. Sergio, P. Gabriela, Mini Review Open Access Role of porous silicon/hydrogel composites on drug delivery, *Mesoporous Biomater.* 3 (2016) 93–101. doi:10.1515/mesbi-2016-0011.
- [10] S. Sood, K. Jain, K. Gowthamarajan, Intranasal therapeutic strategies for management of Alzheimer's disease, *J. Drug Target.* 22 (2014) 279–294. doi:10.3109/1061186X.2013.876644.
- [11] A. Tzur-Balter, A. Gilert, N. Massad-Ivanir, E. Segal, Engineering porous silicon nanostructures as tunable carriers for mitoxantrone dihydrochloride, *Acta Biomater.* 9 (2013) 6208–6217. doi:10.1016/j.actbio.2012.12.010.
- [12] H. Hou, A. Nieto, F. Ma, W.R. Freeman, M.J. Sailor, L. Cheng, Tunable sustained intravitreal drug delivery system for daunorubicin using oxidized porous silicon, *J. Control. Release.* 178 (2014) 46–54. doi:10.1016/j.jconrel.2014.01.003.
- [13] G.S. García-Briones, R. Ocampo-Pérez, C.F.A. Gómez-Durán, T. Neri-Gómez, G. Palestino, Porous silicon microcarriers for extended release of metformin: Design, biological evaluation and 3D kinetics modeling, *Chem. Eng. J.* (2019). doi:10.1016/j.cej.2019.02.022.
- [14] W. Xu, R. Thapa, D. Liu, T. Nissinen, S. Granroth, A. Närvänen, M. Suvanto, H.A. Santos, V.P. Lehto, Smart Porous Silicon Nanoparticles with Polymeric Coatings for Sequential Combination Therapy, *Mol. Pharm.* 12 (2015) 4038–4047. doi:10.1021/acs.molpharmaceut.5b00473.
- [15] N.L. Fry, G.R. Boss, M.J. Sailor, Oxidation-induced trapping of drugs in porous silicon microparticles, *Chem. Mater.* 26 (2014) 2758–2764. doi:10.1021/cm500797b.
- [16] K.L. Jarvis, T.J. Barnes, C.A. Prestidge, Surface chemistry of porous silicon and implications for drug encapsulation and delivery applications, *Adv. Colloid Interface Sci.* 175 (2012) 25–38. doi:10.1016/j.cis.2012.03.006.
- [17] T. Kumeria, S.J.P. McInnes, S. Maher, A. Santos, Porous silicon for drug delivery applications and theranostics: recent advances, critical review and perspectives,

- Expert Opin. Drug Deliv. 00 (2017) 1–16. doi:10.1080/17425247.2017.1317245.
- [18] G. Navarro-Tovar, A. Wong-Arce, M. Campos-Portillo, G. Palestino, S. Rosales-Mendoza, The potential of porous silicon particles for multi-epitopic vaccine development, *Mesoporous Biomater.* 3 (2016) 83–92. doi:10.1515/mesbi-2016-0012.
- [19] D. Rocha-García, M. de L. Betancourt-Mendiola, A. Wong-Arce, S. Rosales-Mendoza, J. Reyes-Hernández, O. González-Ortega, G. Palestino, Gelatin-based porous silicon hydrogel composites for the controlled release of tramadol, *Eur. Polym. J.* 108 (2018) 485–497. doi:10.1016/j.eurpolymj.2018.09.033.
- [20] N. Shrestha, F. Araújo, M.-A. Shahbazi, E. Mäkilä, M.J. Gomes, B. Herranz-Blanco, R. Lindgren, S. Granroth, E. Kukk, J. Salonen, J. Hirvonen, B. Sarmiento, H.A. Santos, Thiolation and Cell-Penetrating Peptide Surface Functionalization of Porous Silicon Nanoparticles for Oral Delivery of Insulin, *Adv. Funct. Mater.* 26 (2016) 3405–3416. doi:10.1002/adfm.201505252.
- [21] D.X. Zhang, L. Esser, R.B. Vasani, H. Thissen, N.H. Voelcker, Porous silicon nanomaterials: recent advances in surface engineering for controlled drug-delivery applications, *Nanomedicine.* 14 (2019) 3213–3230. doi:10.2217/nnm-2019-0167.
- [22] M.B. Gongalsky, A.P. Sviridov, Y.I. Bezsudnova, L.A. Osminkina, Biodegradation model of porous silicon nanoparticles, *Colloids Surfaces B Biointerfaces.* 190 (2020). doi:10.1016/j.colsurfb.2020.110946.
- [23] T. Nissinen, T. Ikonen, M. Lama, J. Riikonen, V.P. Lehto, Improved production efficiency of mesoporous silicon nanoparticles by pulsed electrochemical etching, *Powder Technol.* 288 (2016) 360–365. doi:10.1016/j.powtec.2015.11.015.
- [24] E. Secret, C. Leonard, S.J. Kelly, A. Uhl, C. Cozzan, J.S. Andrew, Size Control of Porous Silicon-Based Nanoparticles via Pore-Wall Thinning, *Langmuir.* 32 (2016) 1166–1170. doi:10.1021/acs.langmuir.5b04220.

- [25] P. Elia, E. Nativ-Roth, Y. Zeiri, Z. Porat, Determination of the average pore-size and total porosity in porous silicon layers by image processing of SEM micrographs, *Microporous Mesoporous Mater.* 225 (2016) 465–471. doi:10.1016/j.micromeso.2016.01.007.
- [26] Y. Zhang, M. Yuan, B. Cai, D. Zhang, H. Chen, Y. Zhu, Morphologies of porous silicon etched by the electrochemical etching method with alcohols additives, *Optik (Stuttg).* 127 (2016) 3009–3012. doi:10.1016/j.ijleo.2015.12.020.
- [27] Z. Qin, J. Joo, L. Gu, M.J. Sailor, Size control of porous silicon nanoparticles by electrochemical perforation etching, *Part. Part. Syst. Charact.* 31 (2014) 252–256. doi:10.1002/ppsc.201300244.
- [28] N. Acosta, I. Aranaz, C. Peniche, A. Heras, Tramadol Release from a Delivery System Based on Alginate-Chitosan Microcapsules, *Macromol. Biosci.* 3 (2003) 546–551. doi:10.1002/mabi.200300009.
- [29] E.A. Ponomarev, C. Lévy-Clément, Macropore formation on p-type silicon, *J. Porous Mater.* 7 (2000) 51–56. doi:10.1023/A:1009690521403.
- [30] M. Subedi, S. Bajaj, M.S. Kumar, M. YC, An overview of tramadol and its usage in pain management and future perspective, *Biomed. Pharmacother.* 111 (2019) 443–451. doi:10.1016/j.biopha.2018.12.085.
- [31] S. Agrawal, P.R. Patel, R.V.N. Gundloori, Proteins as Nanocarriers To Regulate Parenteral Delivery of Tramadol, *ACS Omega.* 4 (2019) 6301–6310. doi:10.1021/acsomega.8b02060.
- [32] M. Mabrouk, H.H. Beherei, S. ElShebiney, M. Tanaka, Newly developed controlled release subcutaneous formulation for tramadol hydrochloride, *Saudi Pharm. J.* 26 (2018) 585–592. doi:10.1016/j.jsps.2018.01.014.
- [33] G.A. Olatunji, A.T. Kola-Mustapha, O.D. Saliu, A.B. Alabi, O.I. Abiodun, N.O. Obisesan, Tramadol hydrochloride delivery by regenerated cellulose nanofiber-TiO₂-ZnO composites, *Korean J. Chem. Eng.* 35 (2018) 784–791. doi:10.1007/s11814-017-0314-8.

- [34] D. Rocha-García, A. Guerra-Contreras, J. Reyes-Hernández, G. Palestino, Thermal and kinetic evaluation of biodegradable thermo-sensitive gelatin/poly(ethylene glycol) diamine crosslinked citric acid hydrogels for controlled release of tramadol, *Eur. Polym. J.* 89 (2017) 42–56. doi:10.1016/j.eurpolymj.2017.02.007.
- [35] A. Tzur-Balter, Z. Shatsberg, M. Beckerman, E. Segal, N. Artzi, Mechanism of erosion of nanostructured porous silicon drug carriers in neoplastic tissues, *Nat. Commun.* 6 (2015) 1–8. doi:10.1038/ncomms7208.
- [36] D.J. Savage, X. Liu, S.A. Curley, M. Ferrari, R.E. Serda, Porous silicon advances in drug delivery and immunotherapy, *Curr. Opin. Pharmacol.* 13 (2013) 834–841. doi:10.1016/j.coph.2013.06.006.
- [37] Smyj R., W.X. P., H. F., Tramadol Hydrochloride, in: *Profiles Drug Subst. Excip. Relat. Methodol.*, Elsevier Inc., Toronto, Canada, 2013: pp. 463–494.
- [38] S. Nayak, V. Singh, V. Bhaskar, DEVELOPMENT AND VALIDATION OF UV SPECTROPHOTOMETRIC METHOD FOR TRAMADOL, *World J Pharm Pharm Sci.* 4 (2015) 773–781.
- [39] A.E.B. Yassin, K. Anwer, H.A. Mowafy, I.M. El-bagory, A. Mohsen, Optimization of 5-fluorouracil solid-lipid nanoparticles : a preliminary study to treat colon cancer, 7 (2010) 398–408.
- [40] J. Li, S. Shen, F. Kong, T. Jiang, C. Tang, C. Yin, Effects of pore size on: In vitro and in vivo anticancer efficacies of mesoporous silica nanoparticles, *RSC Adv.* 8 (2018) 24633–24640. doi:10.1039/c8ra03914c.
- [41] Y. Çağlar, H. Özgür, I. Matur, T. Ebru Dünder, Yenilmez Abdullah, G. Gülfiliz, S. Polat, Ultrastructural evaluation of the effect of N-acetylcysteine on methotrexate nephrotoxicity in rats, *Histol Histopathol.* 28 (2013) 865–874.
- [42] M. Zimmermann, Ethical guidelines for investigations of experimental pain in conscious animals, *Pain.* 16 (1983) 109–110. doi:10.1016/0304-3959(83)90201-4.

- [43] C.A. Winter, E.A. Risley, G.W. Nuss, Carrageenin-Induced Edema in Hind Paw of the Rat as an Assay for Antiinflammatory Drugs, *Proc. Soc. Exp. Biol. Med.* 111 (1962) 544–547. doi:10.3181/00379727-111-27849.
- [44] N. Vergnolle, N.W. Bunnett, K.A. Sharkey, V. Brussee, S.J. Compton, E.F. Grady, G. Cirino, N. Gerard, A.I. Basbaum, P. Andrade-Gordon, M.D. Hollenberg, J.L. Wallace, Proteinase-activated receptor-2 and hyperalgesia: A novel pain pathway, *Nat. Med.* 7 (2001) 821–826. doi:10.1038/89945.
- [45] E.J. Anglin, L. Cheng, W.R. Freeman, M.J. Sailor, Porous silicon in drug delivery devices and materials, *Adv Drug Deliv Rev.* 60 (2008) 1266–1277. doi:10.1016/j.earlhumdev.2006.05.022.
- [46] I.K. Yazdi, A. Ziemys, M. Evangelopoulos, J.O. Martinez, M. Kojic, E. Tasciotti, Physicochemical properties affect the synthesis, controlled delivery, degradation and pharmacokinetics of inorganic nanoporous materials, *Nanomedicine.* 10 (2015) 3057–3075. doi:10.2217/nnm.15.133.
- [47] R. Kadiyam, Yi. Muzib, Colon specific drug delivery of tramadol HCl for chronotherapeutics of arthritis, *Int. J. Pharm. Investig.* 5 (2015) 43. doi:10.4103/2230-973x.147232.
- [48] N. Palla, V. Rajashekar, P. Marni, J. Mittepalli, K.A. Sridhar, Formulation and in-Vitro Evaluation of Tramadol Hydrochloride Floating Tablets, *Int. Res. J. Pharm.* 4 (2016) 138–144. doi:10.7897/2230-8407.04428.
- [49] C. Almansa, R. Mercè, N. Tesson, J. Farran, J. Tomàs, C.R. Plata-Salamán, Co-crystal of Tramadol Hydrochloride-Celecoxib (ctc): A Novel API-API Co-crystal for the Treatment of Pain, *Cryst. Growth Des.* 17 (2017) 1884–1892. doi:10.1021/acs.cgd.6b01848.
- [50] M. Fujiwara, F. Yamamoto, K. Okamoto, K. Shiokawa, R. Nomura, Adsorption of duplex DNA on mesoporous silicas: Possibility of inclusion of DNA into their mesopores, *Anal. Chem.* 77 (2005) 8138–8145. doi:10.1021/ac0516638.
- [51] Y. Zhang, Z. Zhi, T. Jiang, J. Zhang, Z. Wang, S. Wang, Spherical mesoporous

silica nanoparticles for loading and release of the poorly water-soluble drug telmisartan, *J. Control. Release.* 145 (2010) 257–263. doi:10.1016/j.jconrel.2010.04.029.

- [52] Y. Guo, K. Gou, B. Yang, Y. Wang, X. Pu, S. Li, Nanoparticles Loaded Poorly Water-Soluble Drug, (2019).
- [53] D. Liu, K. Lipponen, P. Quan, X. Wan, H. Zhang, E. Mäkilä, J. Salonen, R. Kostianen, J. Hirvonen, T. Kotiaho, H.A. Santos, Impact of Pore Size and Surface Chemistry of Porous Silicon Particles and Structure of Phospholipids on Their Interactions, *ACS Biomater. Sci. Eng.* 4 (2018) 2308–2313. doi:10.1021/acsbomaterials.8b00343.
- [54] L. Jia, J. Shen, Z. Li, D. Zhang, Q. Zhang, G. Liu, D. Zheng, X. Tian, In vitro and in vivo evaluation of paclitaxel-loaded mesoporous silica nanoparticles with three pore sizes, *Int. J. Pharm.* 445 (2013) 12–19. doi:10.1016/j.ijpharm.2013.01.058.
- [55] H. S., Z. F., Effect of zeta potential on the properties of nano-drug delivery systems - A review (Part 1), *Trop. J. Pharm. Res.* 12 (2013) 255–264. http://www.embase.com/search/results?subaction=viewrecord&from=export&id=L368832957%5Cnhttp://www.tjpr.org/vol12_no2/2013_12_2_19.pdf%5Cnhttp://dx.doi.org/10.4314/tjpr.v12i2.19%5Cnhttp://sfx.hul.harvard.edu/sfx_local?sid=EMBASE&issn=15965996&id=doi:10.431.
- [56] U. Kaasalainen, D.P. Fewer, J. Jokela, M. Wahlsten, K. Sivonen, J. Rikkinen, Lichen species identity and diversity of cyanobacterial toxins in symbiosis, *New Phytol.* 198 (2013) 647–651. doi:10.1111/nph.12215.
- [57] E. Mäkilä, L.M. Bimbo, M. Kaasalainen, B. Herranz, A.J. Airaksinen, M. Heinonen, E. Kukk, J. Hirvonen, H.A. Santos, J. Salonen, Amine modification of thermally carbonized porous silicon with silane coupling chemistry, *Langmuir.* 28 (2012) 14045–14054. doi:10.1021/la303091k.
- [58] G. Navarro-Tovar, D. Rocha-García, A. Wong-Arce, G. Palestino, S. Rosales-Mendoza, Mesoporous silicon particles favor the induction of long-lived humoral

- responses in mice to a peptide-based vaccine, *Materials (Basel)*. 11 (2018). doi:10.3390/ma11071083.
- [59] N. Csaba, M. Garcia-Fuentes, M.J. Alonso, The performance of nanocarriers for transmucosal drug delivery, *Expert Opin. Drug Deliv.* 3 (2006) 463–478. doi:10.1517/17425247.3.4.463.
- [60] S. Honary, P. Ebrahimi, M. Tabbakhian, F. Zahir, Formulation and characterization of doxorubicin nanovesicles, *J. Vac. Sci. Technol. B Microelectron. Nanom. Struct.* 27 (2009) 1573. doi:10.1116/1.3127504.
- [61] S. Honary, M. Jahanshahi, R. Golbayani, R. Ebrahimi, K. Ghajar, Doxorubicin-loaded albumin nanoparticles: Formulation and characterization, *J. Nanosci. Nanotechnol.* 10 (2010) 7752–7757. doi:10.1166/jnn.2010.2832.
- [62] S.M. Hartig, R.R. Greene, M.M. Dikov, A. Prokop, J.M. Davidson, Multifunctional nanoparticulate polyelectrolyte complexes, *Pharm. Res.* 24 (2007) 2353–2369. doi:10.1007/s11095-007-9459-1.
- [63] C. Yus, M. Arruebo, S. Irusta, V. Sebastián, Microflow nanoprecipitation of positively charged gastroresistant polymer nanoparticles of Eudragit® RS100: A study of fluid dynamics and chemical parameters, *Materials (Basel)*. 13 (2020) 1–23. doi:10.3390/ma13132925.
- [64] J. Luo, G. Panzarasa, A. Osypova, F. Sorin, F. Spano, R.M. Rossi, A. Sadeghpour, L.F. Boesel, Polyphenols as Morphogenetic Agents for the Controlled Synthesis of Mesoporous Silica Nanoparticles, *Chem. Mater.* 31 (2019) 3192–3200. doi:10.1021/acs.chemmater.8b05249.
- [65] X. Wang, F. Pacho, J. Liu, R. Kajungiro, Factors influencing organic food purchase intention in Tanzania and Kenya and the moderating role of knowledge, *Sustain.* 11 (2019). doi:10.3390/su11010209.
- [66] L. Latifi, S. Sohrabnezhad, M. Hadavi, Mesoporous silica as a support for poorly soluble drug: Influence of pH and amino group on the drug release, *Microporous Mesoporous Mater.* 250 (2017) 148–157. doi:10.1016/j.micromeso.2017.05.026.

- [67] H. Chen, W. Bin Nan, X. Wei, Y. Wang, F. Lv, H. Tang, Y. Li, C. Zhou, J. Lin, W. Zhu, Q. Zhang, Toxicity, pharmacokinetics, and in vivo efficacy of biotinylated chitosan surface-modified PLGA nanoparticles for tumor therapy, *Artif. Cells, Nanomedicine Biotechnol.* 45 (2017) 1115–1122. doi:10.1080/21691401.2016.1202260.
- [68] C. Dabhi, S. Randale, V. Belgamwar, S. Gattani, A. Tekade, Predictable pulsatile release of tramadol hydrochloride for chronotherapeutics of arthritis, *Drug Deliv.* 17 (2010) 273–281. doi:10.3109/10717541003706240.
- [69] K. gounder Subramanian, V. Vijayakumar, Synthesis and evaluation of chitosan-graft-poly (2-hydroxyethyl methacrylate-co-itaconic acid) as a drug carrier for controlled release of tramadol hydrochloride, *Saudi Pharm. J.* 20 (2012) 263–271. doi:10.1016/j.jsps.2011.09.004.
- [70] M.D. Aher, A.P. Jain, P.D. Kumbharde, N.S. Jadhav, Formulation and Evaluation of Sustained Release Matrix Tablets of Tramadol Hydrochloride and Study Itâ€™S Release (Dissolution) Kinetics, *Int. Res. J. Pharm.* 6 (2015) 528–536. doi:10.7897/2230-8407.068105.
- [71] S.K. GUPTA, A. HUNEZA, S. PATRA, Formulation, Development and in Vitro Evaluation of Tramadol Extended Release Tablets, *Int. J. Pharm. Pharm. Sci.* 11 (2019) 63–73. doi:10.22159/ijpps.2019v11i7.32100.
- [72] M.A. Naeem, A. Mahmood, S.A. Khan, Z. Shahiq, Development and evaluation of controlled-release bilayer tablets containing microencapsulated tramadol and acetaminophen, *Trop. J. Pharm. Res.* 9 (2010) 347–354. doi:10.4314/tjpr.v9i4.58926.
- [73] B. Selvaraj, P. Shanmugapandiyan, FORMULATION AND DEVELOPMENT OF TRAMODOL HYDROCHLORIDE EXTENDED RELEASE TABLETS, *J. Drug Deliv. Ther.* 3 (2013) 72–78. doi:10.22270/jddt.v3i4.572.
- [74] J. Lalani, Y. Raichandani, R. Mathur, M. Lalan, K. Chutani, A.K. Mishra, A. Misra, Comparative receptor based brain delivery of tramadol-loaded poly(lactic-co-

- glycolic acid) nanoparticles, *J. Biomed. Nanotechnol.* 8 (2012) 918–927. doi:10.1166/jbn.2012.1462.
- [75] P. Keyur, P. Vishnu, P. Mandev, P. Pranav, A. Ankit, R. Kinjal, PREPARATION AND CHARACTERIZATION OF TRAMADOL HYDROCHLORIDE MICROSPHERES, *Int. J. Drug Dev. Res.* 2 (2010) 260–266. <http://www.ijddr.in>.
- [76] P. Kinnari, E. Mäkilä, T. Heikkilä, J. Salonen, J. Hirvonen, H.A. Santos, Comparison of mesoporous silicon and non-ordered mesoporous silica materials as drug carriers for itraconazole, *Int. J. Pharm.* 414 (2011) 148–156. doi:10.1016/j.ijpharm.2011.05.021.
- [77] J. Andersson, J. Rosenholm, S. Areva, M. Lindén, Influences of material characteristics on ibuprofen drug loading and release profiles from ordered micro- and mesoporous silica matrices, *Chem. Mater.* 16 (2004) 4160–4167. doi:10.1021/cm0401490.
- [78] T. Heikkilä, J. Salonen, J. Tuura, N. Kumar, T. Salmi, D.Y. Murzin, M.S. Hamdy, G. Mul, L. Laitinen, A.M. Kaukonen, J. Hirvonen, V.P. Lehto, Evaluation of mesoporous TCPSi, MCM-41, SBA-15, and TUD-1 materials as API carriers for oral drug delivery, *Drug Deliv.* 14 (2007) 337–347. doi:10.1080/10717540601098823.
- [79] N.H. Maniya, S.R. Patel, Z.V.P. Murthy, Controlled delivery of acyclovir from porous silicon micro- and nanoparticles, *Appl. Surf. Sci.* 330 (2015) 358–365. doi:10.1016/j.apsusc.2015.01.053.
- [80] A.W. Hixson, J.H. Crowell, Dependence of Reaction Velocity upon Surface and Agitation, *Ind. Eng. Chem.* 23 (1932) 923–931.
- [81] N.H. Maniya, S.R. Patel, Z.V.P. Murthy, Drug delivery with porous silicon films, microparticles, and nanoparticles, *Rev. Adv. Mater. Sci.* 44 (2016) 257–272.
- [82] C. Maderuelo, A. Zarzuelo, J.M. Lanao, Critical factors in the release of drugs from sustained release hydrophilic matrices, *J. Control. Release.* 154 (2011) 2–19. doi:10.1016/j.jconrel.2011.04.002.

- [83] D. Wójcik-Pastuszka, J. Krzak, B. Macikowski, R. Berkowski, B. Osiński, W. Musiał, Evaluation of the release kinetics of a pharmacologically active substance from model intra-articular implants replacing the cruciate ligaments of the knee, *Materials (Basel)*. 12 (2019). doi:10.3390/ma12081202.
- [84] R.W. Korsmeyer, R. Gurny, E. Doelker, P. Buri, N.A. Peppas, Mechanisms of solute release from porous hydrophilic polymers, *Int. J. Pharm.* 15 (1983) 25–35. doi:10.1016/0378-5173(83)90064-9.
- [85] P. Oliva, C. Aurilio, F. Massimo, A. Grella, S. Maione, E. Grella, M. Scafuro, F. Rossi, L. Berrino, The antinociceptive effect of tramadol in the formalin test is mediated by the serotonergic component, *Eur. J. Pharmacol.* 445 (2002) 179–185. doi:10.1016/S0014-2999(02)01647-3.
- [86] E. Guneli, N.U. Karabay Yavasoglu, S. Apaydin, M. Uyar, M. Uyar, Analysis of the antinociceptive effect of systemic administration of tramadol and dexmedetomidine combination on rat models of acute and neuropathic pain, *Pharmacol. Biochem. Behav.* 88 (2007) 9–17. doi:10.1016/j.pbb.2007.06.006.
- [87] J. Shah, A.B. Nair, H. Shah, S. Jacob, T.M. Shehata, M.A. Morsy, Enhancement in antinociceptive and anti-inflammatory effects of tramadol by transdermal proniosome gel, *Asian J. Pharm. Sci.* (2019) 1–11. doi:10.1016/j.ajps.2019.05.001.
- [88] S.M.S. Lamana, M.H. Napimoga, A.P.C. Nascimento, F.F. Freitas, D.R. de Araujo, M.S. Quinteiro, C.G. Macedo, C.L. Fogaça, J.T. Clemente-Napimoga, The anti-inflammatory effect of tramadol in the temporomandibular joint of rats, *Eur. J. Pharmacol.* 807 (2017) 82–90. doi:10.1016/j.ejphar.2017.04.012.

CHAPTER 2

OPTIMIZED MICROWAVE-ASSISTED FUNCTIONALIZATION AND QUANTIFICATION OF SUPERFICIAL AMINO GROUPS ON POROUS SILICON NANOSTRUCTURED MICROPARTICLES

Cándida Anahy Cisneros-Covarrubias,^a Gabriela Palestino,^{ab} César F. A. Gómez-Durán,^a Sergio Rosales-Mendoza^b and María de Lourdes Betancourt-Mendiola^{*b}

^aLaboratorio de Biopolímeros y Nanoestructuras, Facultad de Ciencias Químicas, Universidad Autónoma de San Luis Potosí, C.P. 78210 San Luis Potosí, México.

^bSección de Biotecnología, Centro de Investigación en Ciencias de la Salud y Biomedicina, Universidad Autónoma de San Luis Potosí, C.P. 78210 San Luis Potosí, México.

Published in: Analytical Methods

Year: 2021

DOI: 10.1039/d0ay02083d.

ABSTRACT

This work presents an optimized microwave (MW)-assisted method for the chemical functionalization of porous silicon particles (PSip). 3-(Aminopropyl)triethoxysilane (APTES) was grafted on previously stabilized PSip. The functionalization efficiency was studied and optimized in terms of reaction time (Rt) and reaction temperature (RT) using a central composite design (CCD). The effect of MW irradiation on the surface coverage was found to strongly depend on the PSip surface chemistry, Rt, RT, and percentage of APTES. Quantification of grafted amino groups was performed by the ninhydrin method (NHIM); confirming the results by thermogravimetric analysis (TGA). Reacting with 5% APTES solution at 95°C for 26 min were the best functionalization conditions. Efficiency of PSip-APTES prepared under the optimized conditions were compared to those functionalized by the traditional method; MW irradiation increases by 39 % the number of functional groups grafted onto the PSip surfaces with the additional benefit of having a drastic reduction in Rt.

1. INTRODUCTION

The development of simpler methods that allow functionalizing micro or nanomaterials to confer them with the desired feature is one of the emerging challenges in nanotechnology. In this area, porous silicon particles (PSip) have arisen as promising candidates in a variety of applications that include the production of composites materials, [1,2] adsorbents, [3,4] and biosensors; [5] as well as medical diagnosis [6] and drug delivery systems. [7,8] The main advantages of PSip over other nanomaterials derive from their physicochemical and biological properties, which include high surface area, tunable pore size, high pore volume, and proved biocompatibility and biodegradability. [5] Coverage of the PSip surface with organic functional groups is highly desirable since it imparts them with stability under physiological conditions and enables further modification to achieve a specific function. The functionalization process to activate the PSip surface is often carried out by grafting

small organic molecules bearing an appropriate functional group (e.g., COOH, -NH₂, or -SH); via covalent bond formation.

3-(Aminopropyl)triethoxysilane (APTES) is an organosilane coupling agent having a free primary amino group that has been widely used for the conjugation of organic molecules (e.g., drugs, polymers, and dyes) and biomolecules (e.g., proteins and peptides) onto the PSip surface. [9-12] Often, APTES is used as a bridge to couple other molecules to the nanostructure through glutaraldehyde and carboxylic acid activation. [13] APTES silanization involves the covalent attachment of alkoxy groups onto oxidized (Si-O⁻ terminated) or hydroxylated (Si-OH- terminated) PSip surfaces. An important issue in the traditional methods used for PSip functionalization is the reaction time (Rt) necessary to produce the maximum surface coverage of the functional molecule. Several conditions of reaction in different silicon-containing materials (e.g., oxidized PSip, [14] thermally carbonized porous silicon (TCPSi) particles, [15–17] layers [13] of fresh and oxidized PSi,[18] and hydroxylated Si wafer [19] have been tested to covalently attach APTES on the materials surface. The functionalization conditions include various APTES concentrations and reaction times. From these studies it can be concluded that to obtain an optimal surface coverage a low concentration of APTES (2 – 5 %) and long reaction times (20 - 24 h) [13,14,19] or relatively high concentration of APTES (10 %) and short reaction times (20 - 60 min) [15] are the best combinations. However, using long functionalization time (> 1 h) is problematic [20] as it might induce APTES polymerization resulting in the formation of multiple layers over the surface or non-uniform coverage, meanwhile a functionalization time of 20 min produces APTES monolayers in the surface using the same reaction conditions. More recent studies use microwave (MW) irradiation as an useful tool for the silanization reaction; improving the amount of APTES grafted on the surfaces, while decreasing reaction times. [16]

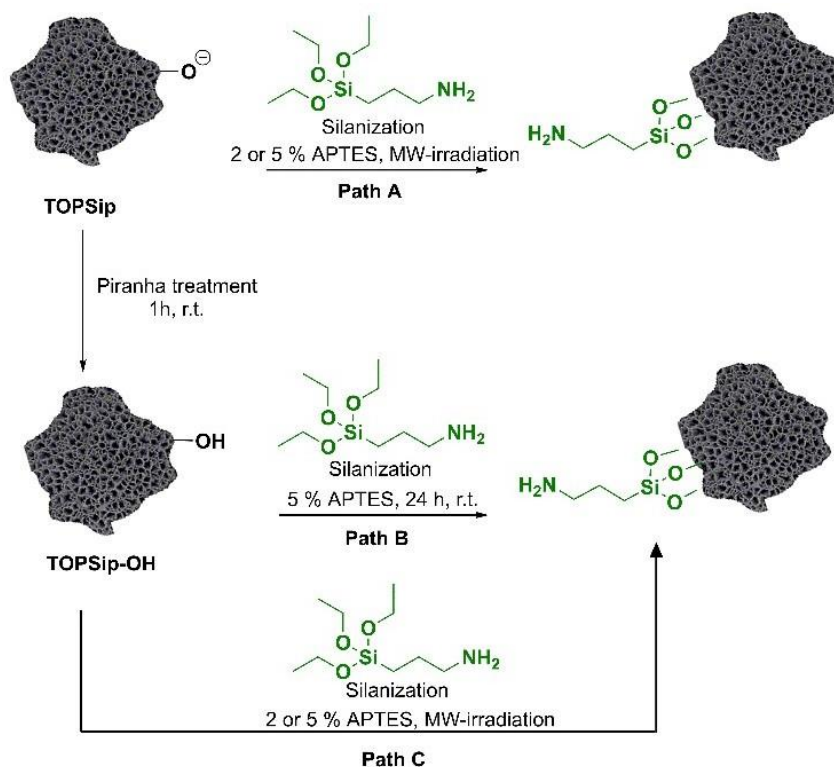
Given that surface chemistry is one of the most critical factors to determine the behaviour of the material, a good characterization of the number of reactive functional groups present in the particle is relevant to estimate the possible amount of recognition

units that can be attached onto the surface. In this sense, quantifying amino groups on PSip nanostructures is crucial since they are the point of interaction with other molecules for further functionalization. Several methods for amino groups quantification are available in the literature that include NMR, [21] XPS, fluorescence spectroscopy, [22] and chemical derivatization. [23,24] Nevertheless, most of these methods require expensive reagents, solvents, and sophisticated equipment. The ninhydrin method (NIHM) has been widely used for the quantitative determination of amino acids and other amino-containing compounds in different research fields (e.g., clinical, biomedical, food, forensic, and nutritional). [25,26] In the materials field, some reports have shown the applicability of NIHM in the quantification of amino groups; specifically on silica and iron particles. [27–29] Nevertheless, to the best of our knowledge, its application on porous materials such as PSip has not been reported yet. NIHM has several advantages over other methods; it is based on low-cost reagents and solvents and expensive equipment is not required since the reaction between ninhydrin and primary amino groups produces a purple dye (known as Ruhemann's purple) with high extinction coefficient that can be easily quantified by UV-Vis spectroscopy. Besides, the NIHM is highly reproducible and sensitive.

In this work, we report a new optimized method for the direct amino functionalization of PSip using MW irradiation (Scheme 1). A comparison was made with the traditional APTES grafting conditions, which consist of TOPSip-OH functionalization using 5% APTES solution for 24 h at r.t. (Figure 1, path B). [19,30] We also evaluated the surface reactivity of oxidized porous silicon particles (TOPSip) (Scheme 1, path A) and hydroxylated porous silicon particles (TOPSip-OH) (Scheme 1, path C) using dry toluene as solvent and APTES as silylating agent at two different concentrations (2 and 5 %). With these exploring results, a DOE was performed to determine the optimal R_t and R_T for MW- assisted APTES functionalization (Scheme 1).

We found that the effect of MW irradiation on the loading amount of APTES strongly depends on the PSip surface chemistry; as well as the MW-assisted reaction

time (Rt), reaction temperature (RT), and the amount of APTES initially used. The proposed functionalization technique presents many advantages compared to traditional protocols such as the enhancement of reaction kinetics, a larger amount of APTES grafted on the surface, and its associated low cost. [27,28] We also studied the feasibility of using NIHM for the quantification of amino groups attached to the PSi surface. For the first time, it is demonstrated that the ninhydrin method offers a useful tool to quantify the concentration of amino groups covalently grafted onto the surface of PSi. The NIHM results for amino content were compared to those retrieved from a thermogravimetric analysis (TGA); from both results, we conclude that the ninhydrin method is an excellent alternative for amino group quantification having several gains over TGA such as the small amount of sample required, low cost of the reagents, and the use of non-sophisticated analytic equipment.



Scheme 1. Different pathways for TOPSiP functionalization by traditional method (path B) and MW-assisted methods (paths A and C).

2. EXPERIMENTAL SECTION

2.1 General materials and methods

All reagents and solvents commercially available were purchased in reagent grade and were used as received without any further purification.

2.2 Synthesis of TOPSip

PSip were prepared by electrochemical anodization of p⁺⁺ type boron-doped (100) oriented Cz-silicon wafer (0.005 Ω -cm resistivity) in an electrolyte composed of a 3:7 (v/v) mixture of HF (48%) and ethanol (99 %). The synthesis was carried out by successively applying 40 cycles of two different current densities: 15 and 50 mA cm⁻² during 73 and 3 s, respectively. PSi layers were lifted-off from the Si wafer via an electropolishing step using ten pulses of 5 s at 184 mA cm⁻². After etching, the PSi layers were rinsed three times with EtOH. Free-standing PSi layers were sonicated in fresh EtOH using an ultrasonic tip (SONICS Vibra-Cell, 30% amplitude) for 60 min. The obtained PSip were stabilized by thermal oxidation (TOPSip) in a furnace (Carbolite) for 45 min at 450°C under ambient air; with a ramp rate of 10 °C min⁻¹. Hydroxylated PSip (TOPSip-OH) were obtained suspending 10 mg of TOPSip in 2 mL of H₂SO₄/H₂O₂ (1:1.6 v/v) and shaking for 1 h at room temperature. The piranha solution was decanted and the microparticles were washed three times with DI water and two times with ethanol.

2.3 Functionalization of TOPSip-OH via traditional method

The functionalization reaction was performed under room temperature by mixing, in a glass vial, 10 mg of the TOPSip-OH with 10 mL of 5 % (v/v) APTES solution in dry toluene. The mixture was stirred at 200 rpm for 24 h. After functionalization, the solid product was washed three times using ethanol and dried at 100 °C for 1 h.

2.4 Functionalization of TOPSip via microwave irradiation

Microwave reactions were carried out in a sealed microwave vials equipped with magnetic stir bars and heated in Anton Paar Monowave 400 microwave reactor. The functionalization was carried out by mixing in a glass reactor 10 mg of the selected microparticles (TOPSip or TOPSip-OH) with 2 or 5 % (v/v) APTES solution in dry toluene under microwave irradiation. The mixture was homogenized, heated at different temperatures and times (according to the CCD), and stirred at 600 rpm. After functionalization, the solid product was washed three times using ethanol and dried at 100 °C for 1 h.

2.5 Physicochemical characterization of PSip

High-Resolution Scanning Electron Microscopy images were obtained on a Dual Beam (FIB/SEM) FEI-Helios Nanolab 600 at 4000 and 100000 × magnification. High-resolution transmission electron microscopy micrographs of TOPSip and elements mapping analyses were obtained using a microscope HRTEM/STEM JEOL JEM-2100 operated with an acceleration voltage at 200 kV and resolution of 0.14 nm at 40000 × magnification. ATR-FTIR spectra were recorded using an Agilent Cary 600 spectrophotometer. Stability and ζ -potential distribution were measured on a Zetasizer Nano ZS (Malvern Instruments) using electrophoretic light scattering (ELS). Thermogravimetric analysis for TOPSip-OH/APTES was performed in a Q500 TGA (TA Instruments). TOPSip/APTES were heated up to 600 °C using a temperature ramp of 10 °C min⁻¹ under a constant N₂ flush of 20 mL min⁻¹.

2.6 Central composite design (CCD)

The amino-functionalization of TOPSip-OH was optimized using an orthogonal and spherical central composite design for the response surface. The studied factors were reaction temperature (A) (80 - 120 °C) and reaction time (B) (5 - 30 min). The high and low levels of A and B were taken as axial points. The total number of experiments

was 22 according to the expression: 2^n ($2^2 = 4$: factor points) + $2n$ ($2 \times 2 = 4$: axial points), + 3 center points, all with replicas and two blocks. The analysis of variance (ANOVA) of the results was carried out using the following second-order polynomial model (eq. (1)):

$$Y = \beta_0 + \beta_1 A + \beta_2 B + \beta_{12} AB + \beta_{11} A^2 + \beta_{22} B^2 \quad (1)$$

where Y is the [TOPSip-OH/APTES] ($\mu\text{mol mg}^{-1}$) grafted on PSip, β_n are the linear regression coefficients, and A and B the studied factors. The influence of the model parameters was evaluated using a significance level of $\alpha = 5\%$.

2.7 Quantification of amino groups

Quantification of amino groups grafted on the PSip surface was performed by the ninhydrin method. Briefly, ninhydrin (200 mg) and hydrindantin (30 mg) were dissolved in DMSO (7.5 mL), afterward 2.5 mL of acetate buffer (4 M, pH = 5.2) were added. The mixture was bubbled with N_2 for 3 min. 1 mg of TOPSip suspended in 1 mL of water and 1 mL of the ninhydrin-hydrindantin mixture were placed in screw-cap test tubes and heated in a water bath for 20 min. After heating, the suspension was cooled in an ice bath. Afterwards 5 mL of a EtOH:H₂O mixture (1:1) were added, following homogenization; the absorbance of the suspension was measured (Cary 60 spectrophotometer) at 570 nm. A calibration curve ($R^2 = 0.9955$) was performed reacting different amounts of aqueous APTES solution as standard (1-200 $\mu\text{g mL}^{-1}$) with ninhydrin-hydrindantin solution following the procedure described above.

3. RESULTS AND DISCUSSION

3.1 Morphological characterization of PSip

The morphological and chemical analyses of TOPSip are shown in Fig. 1. The HR-SEM micrograph of TOPSip in Fig. 1A shows irregularly shaped microparticles,

with an average size of $1.02 \pm 0.41 \mu\text{m}$ (histogram in Fig. 1B). The TOPSip thickness was found to be $0.48 \pm 0.08 \mu\text{m}$, while the average porosity was calculated as $87 \pm 3\%$ (based on gravimetric measurements). As shown in Fig. 1C, the TOPSip surface is composed of a porous network with an average pore size of $67.43 \pm 28.64 \text{ nm}$ (histogram in Fig. 1D). The HR-TEM micrograph of Fig. 1E corresponds to a lateral view of the microparticles that exhibits straight pores. The element mapping analyses are shown in Figures 1(F-G). Figure 1F evidences the structure and element distribution of TOPSip. The bright red and green spots indicate the presence of silicon and oxygen, respectively; the characteristic elements of TOPSip. After amino functionalization (Figure 1G), carbon (purple spots) and nitrogen (white spots) are observed over the surface; confirming that APTES was homogeneously grafted onto the TOPSip surface.

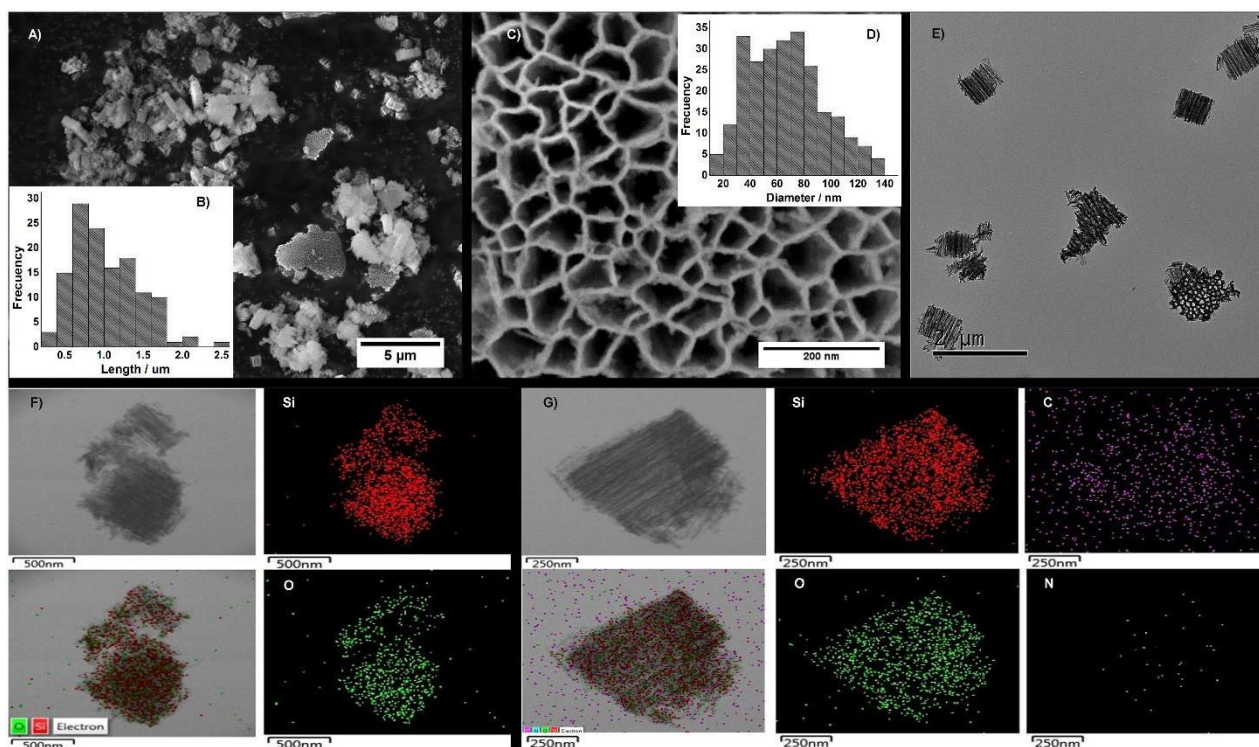


Fig. 1. Morphological and chemical analyses of TOPSip. HR-SEM micrograph showing: (A) TOPSip shape and (C) pore size. (B) Particle size distribution histogram. (D) Pore size distribution histogram. (E) HR-TEM micrograph of TOPSip. (F) STEM image and elemental mapping of TOPSip and (G) TOPSip-OH/APTES.

Chemical modification of PSip was followed by ATR-FTIR (Fig. 2). As expected, the TOPSip spectrum displays a strong band at 1060 cm^{-1} attributed to the siloxane groups (ν Si-O-Si) generated after thermal oxidation (Fig. 2A). The absorption band at 3389 cm^{-1} (ν Si-OH) assured hydroxylation of the microparticles (TOPSip-OH) (Fig. 2A). The spectrum of functionalized TOPSi-OH/APTES (Fig. 2B) shows a new group of weak bands attributed to the presence of the amino-silane molecule: 3349 cm^{-1} (ν_{asy} N-H), 1559 and 1484 cm^{-1} (δ N-H) belonging to NH_2 , and 2931 (ν_{sym} C-H) and 2879 cm^{-1} (ν_{asym} C-H) characteristic of CH_2 . It is essential to notice that band intensities increase as consequence of the attachment of APTES onto the TOPSip-OH surface (Figure 2B). [13]

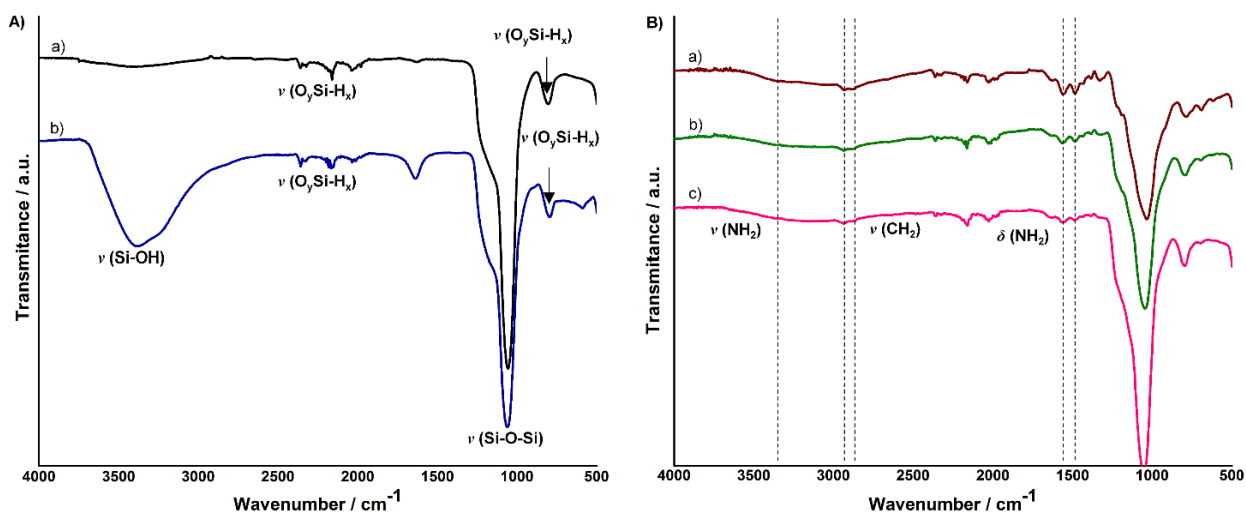


Fig. 2. ATR Fourier transform infrared spectra of (A) TOPSip (a) and TOPSip-OH (b) and (B) TOPSip-OH/APTES functionalized with different amounts of APTES: 2.19 (a), 1.504 (b), and 0.888 $\mu\text{mol mg}^{-1}$ (c).

ζ -potential measurements also confirmed the presence of APTES on the microparticle surface. The effect of TOPSip-OH surface chemistry and pH on the ζ -potential before and after functionalization with APTES was studied by using different

buffered TOPSip suspensions. The isoelectric points (IEPs) and characteristic curves are shown in Fig. 3. The IEP of TOPSip-OH was found at 2.1, in agreement with previous reports. [15,31] The functionalization of TOPSip-OH with APTES shifted the IEP of the particles to higher values (6.3). The significant change in the particles charge is attributed to the primary amino groups of the amino-silane molecule attached via siloxane bond formation to the TOPSip-OH surface. [7]

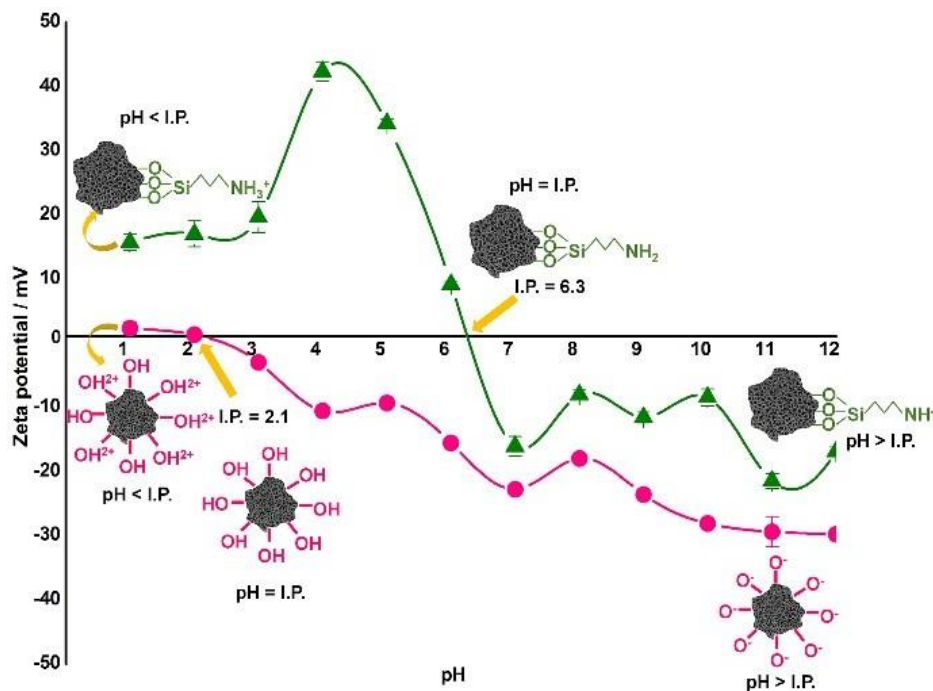
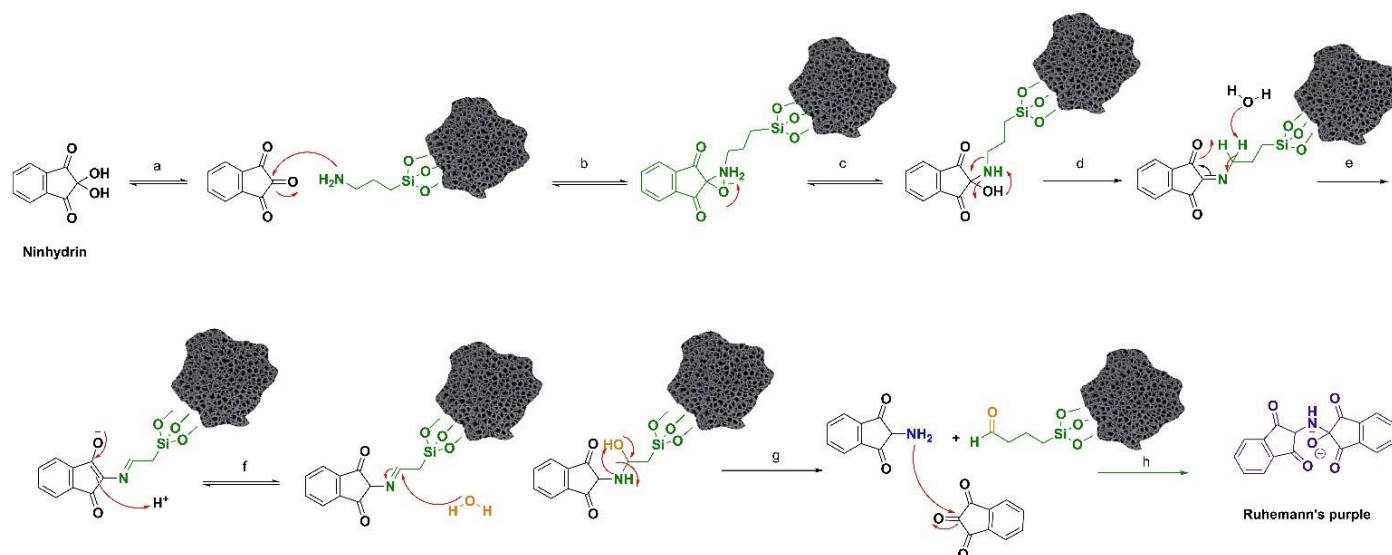


Fig. 3. Titration curve of ζ -potential vs. pH for TOPSip-OH (pink line) and TOPSip-OH/APTES (green line) after functionalization.

3.2 Quantification of amino groups

Quantification of amino groups grafted on the PSip surface was performed by the NIHM. The reaction mechanism is shown in Scheme 2, which involves the oxidative deamination of the primary amino group. In the first step (a), the amino group from APTES reacts with a ninhydrin molecule forming an imine intermediate (d), the hydrolysis (e) of the formed imine produces the corresponding ninhydrin-NH₂ and the solid PSip with an aldehyde functionality (f). The formed ninhydrin-NH₂ goes through a

condensation reaction with a second equivalent of ninhydrin to produce Ruhemann's purple (h). [32]



Scheme 2. Reaction mechanism between ninhydrin and TOPSip-OH/APTES to produce Ruhemann's purple dye.

3.3 Exploring experiments

In order to elucidate the optimal APTES-functionalization reaction conditions, some exploring experiments were conducted to evaluate the following synthesis variables: 1) The functionalization method, 2) The PSip surface chemistry, and 3) The concentration of APTES. The effect of these variables was determined by quantifying the concentration of amino groups attached to the PSip surface by NIHM; their statistical significance was assessed by a Student's t-test. An ANOVA was performed with a significance level $\alpha = 5\%$ ($P\text{-value} < 0.05$).

The efficacy of the proposed MW-assisted method was compared to the traditional functionalization method. [19,30] The results are summarized in Table 1. It can be observed that the concentration of amino groups attached to the PSip surface was increased by $\sim 39\%$ when using the MW-assisted method, with the additional

advantage of having a drastic reduction in R_t (15 min vs. 24 h). This result was statistically significant with a P- value lower than 0.05 ($P(t_0) = 0.0165$).

On the other hand, since the silanization reaction can be conducted in oxidized or hydroxylated PSip microparticles; [19,23,30] we evaluated the influence of the PSip chemical surface on the amount of APTES attached after the MW reaction. The effect of APTES concentration (2 and 5 %) [16,33] was found to depend on the PSip surface chemistry (Table 1). It can be observed that the amount of APTES grafted on thermally oxidized particles (TOPSip), characterized by a surface with high amount of oxygen; is not significantly different for the evaluated APTES concentrations. This result was statistically confirmed with the P-value obtained, which was higher than 0.05 ($P(t_0) = 0.3321$). Nevertheless, when APTES functionalization was evaluated in hydroxylated particles (TOPSip-OH), [19,23,30] with a surface mainly covered by hydroxyl groups; a 100 % increase on PSip surface coverage was obtained, maintaining the APTES concentration at 2 %. Remarkably, when the APTES concentration was increased to 5 %, the APTES surface coverage increased 3-fold compared to that obtained with TOPSip. These results confirmed that silanol groups (Si-OH) promote higher efficiency of the amino-silanization reaction. The P-values were lower than 0.05 for both tests ($P(t_0) = 0.0216$) and $P(t_0) = 0.0324$, respectively); confirming the statistical significance of the results.

Table 1. Measured concentration of APTES on TOPSip and TOPSip-OH using 2 and 5% APTES solution.

Sample	APTES (%)	Amino groups concentration (umol mg ⁻¹)
TOPSip ^a	2	0.3865 ± 0.0362
	5	0.4112 ± 0.0136
TOPSip-OH ^a	2	0.6029 ± 0.0958
	5	1.2410 ± 0.2901
Traditional method ^b	5	0.4846 ± 0.0371
Reaction conditions: [a] 120°C, 15 min under MW irradiation.		
[b] Traditional method using TOPSip-OH, 24 h, r.t.		

From the results in Table 1, it can be concluded that the MW- assisted amino functionalization using TOPSip-OH particles and 5 % APTES solution leads to higher amount of APTES grafted on the surface compared to the traditional method. Encouraged by these findings, in a second step, the silanization conditions under MW-irradiation were optimized. The dependence of Rt and RT on functionalization efficiency was determined with a central composite statistical design. The results of this study are reported below.

3.4 APTES functionalization: The second-order model and analysis of variance (ANOVA)

The results of the ANOVA for the studied [TOPSip-OH/APTES] (concentration of amino groups attached to the TOPSip-OH surface) is shown in Table 2. The coefficients display the un- coded terms. A second-order polynomial model obtained using Design-Expert® (Version 7.1.4) was adopted to describe the response surface. As it is observed in Table 2, the probability of β_0 is < 0.05 , which makes the overall analysis statistically significant. From the P-values, a linear contribution for Rt can be concluded. However, it is worth noticing that RT by itself has no effect over the

response variable, while contributions of the R_t and RT cross-product; as well as the quadratic products of RT and R_t do have important effects in the model. In addition, it was observed that the block design (each block represents an experimentation day) showed important significance ($P = 0.0009$) and strong influence in the response.

Table 2. Estimated regression coefficients and P-values of the second-order polynomial model for [TOPSip-OH/APTES].

Term	Coefficient ($R^2 = 0.77$)	P-value
β_0	-11.0575	0.0003*
A	0.2249	0.3406
B	0.1146	0.0036*
AB	-0.0015	0.0080*
A^2	-0.0009	0.0017*
B^2	0.0014	0.0415*
* $P < 0.05$. A is RT ($^{\circ}C$) and B is R_t		

3.5 Model fitting and statistical analysis

In the CCD presented in Table 3, [TOPSip-OH/APTES] was correlated to the two independent variables studied: reaction temperature (A) and reaction time (B). The twenty-two experiments and their respective responses are shown in Table 3. Model fitting was performed in the Design-Expert® (Version 7.1.4) software using a second-order polynomial model. The model adequacy was further verified using ANOVA (Table 2). The ANOVA for the [TOPSip-OH/APTES] showed that the model is highly significant. The quadratic regression model in un-coded terms obtained from the experimental data of Table 3 is given in Eqn. 2.

$$Y = -11.0575 + 0.2249A + 0.1146B - 0.0009A^2 + 0.0014B^2 \quad (2)$$

where Y is the [TOPSip-OH/APTES] ($\mu\text{mol mg}^{-1}$), A is reaction temperature ($^{\circ}\text{C}$), and B is reaction time (min).

For this analysis, the estimated determination coefficient (R^2) was 0.77; indicating that approximately 77% of the parameter's variability is accounted for in the statistical model. In this framework, R^2 explains the observed variation in the dependent variables attributed to all the combined independent variables; hence, although an acceptable fit has an R^2 close to 1.0, [34] this number alone cannot determine whether predictions are biased since this value can be consequence of latent variables that caused noise at the moment of experimentation.

Table 3. 2² factorial central composite design with coded and uncoded variables.
Experimental and predicted values for the [TOPSip-OH/APTES].

STD	BLK	Variables in coded levels		Variables in uncoded levels		[TOPSip-OH/APTES] (Y)/ $\mu\text{mol mg}^{-1}$		Error (%)
		A	B	A	B	Exp	Pred	
1	1	-1	-1	86	9	0.98	1.01	3.56
2		-1	-1	86	9	0.92	1.01	10.17
3		1	-1	114	9	1.33	1.48	10.76
4		1	-1	114	9	1.23	1.48	19.71
5		-1	1	86	26	1.57	1.69	7.88
6		-1	1	86	26	1.50	1.69	12.89
7		1	1	114	26	1.10	1.40	27.11
8		1	1	114	26	1.15	1.40	21.59
9		0	0	100	17.5	1.37	1.49	8.60
10		0	0	100	17.5	1.44	1.49	3.11
11		0	0	100	17.5	1.42	1.49	4.34
12	2	-1.4	0	80	17.5	0.88	1.03	17.03
13		-1.4	0	80	17.5	1.37	1.03	24.20
14		1.4	0	120	17.5	1.44	1.15	19.94
15		1.4	0	120	17.5	1.40	1.15	17.55
16		0	-1.4	100	5.0	1.86	1.49	19.89
17		0	-1.4	100	5.0	1.38	1.49	7.83
18		0	1.4	100	30	2.19	1.91	12.53
19		0	1.4	100	30	2.14	1.91	10.69
20		0	0	100	17.5	1.71	1.49	12.91
21		0	0	100	17.5	1.37	1.49	8.76
22		0	0	100	17.5	1.60	1.49	7.22

It is usually necessary to verify that the quadratic regression model provides an adequate approximation to the [TOPSip- OH/APTES] response. In this sense, the statistical model could be used to predict future behaviour when changing the values of the independent variables studied (RT and Rt). To prove this fact, a graphical method was used as tool to validate the model obtained. Fig. 4 shows the experimental data obtained from the [TOPSip-OH/APTES] response when performing the CCD and the predicted values from the second-order polynomial model (Eqn. 1). The predicted responses show small to moderate deviations compared to the experimental data. As mentioned above, the value of the estimated determination coefficient (R^2) was 0.77. In agreement with this value, the predicted responses show a variability of ~23%. In addition, an insignificant lack of fit ($P = 0.2009$) was found in the second-order polynomial model for the [TOPSip-OH/APTES], which implies a low variation of the calculated data. [35] All the above results indicate that the statistical model could adequately predict the response.

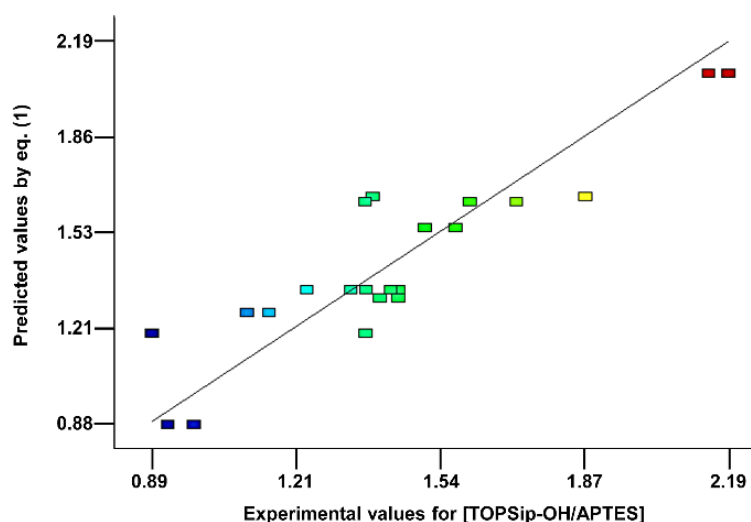


Fig. 4. [TOPSip-OH/APTES] experimental values plotted against predicted values from the regression model in uncoded values.

3.6 Response surface analysis and optimization process

The effects of RT and Rt and their cross-interaction on [TOPSip- OH/APTES] were studied by response surface analysis. According to Fig. 5, it can be observed that an increase in Rt promotes higher concentration of APTES on the TOPSip-OH surface, which demonstrates the significant linear contribution of this variable during the functionalization procedure. Although these results suggest that maximum coverage of the functional molecule on the TOPSip-OH surface can be reached when increasing Rt; there is a limit, determined by the chemical nature of APTES that tends to polymerize at longer Rt (> 1 h); resulting in multilayers and non-uniform coverage. [20,36,37] Thus, the Rt obtained in the MW-assisted method (~ 26 min) is optimal to avoid the negative effects mentioned.

There is also a significant influence of RT on promoting the APTES chemical reaction. Higher RT produced an increase in TOPSip-OH coverage. However, it should be noticed that the maximum APTES surface grafting was obtained at middle-temperature values; denoting the quadratic influence of this variable in the chemical process. This behaviour could be attributed to the increment in the hydrolysis rate of APTES molecules (caused by the physisorbed water on TOPSip-OH) promoted by the increase in the Brownian motion of organic molecules in the solution. Under this scenario, the hydrolyzed ethoxy groups from APTES react faster with the surface of TOPSip-OH resulting in the formation of a denser and more ordered monolayer. [37,38] Nevertheless, at the highest RT; the reduction of APTES surface coverage compared to that obtained for middle-temperature values can be attributed to the formation of siloxane bonds (Si-O-Si), induced by the proximity of grafted molecules. The formation of siloxane bonds can produce various molecular configurations (horizontal and vertical reticulation), which make difficult to control the structure of the surface silane layer. [37–40] Therefore, this effect should be avoided since it produces pore blocking and, in fact, it could explain the similar values of the [TOPSip-OH/APTES] obtained at any Rt; maintaining constant the RT at its highest value.

The response surface plot (Fig. 5) reveals a visual interpretation of the interaction between Rt and RT that allowed localizing the optimal experimental conditions (overlaid contour, Fig. 5). By analysing the response surface and the derivative of the second- order polynomial model (Eqn. 1), the maximum APTES surface coverage on TOPSip-OH was found at $1.7786 \mu\text{mol mg}^{-1}$. The optimal values of RT and Rt predicted by the model are 95°C and 26 min, respectively.

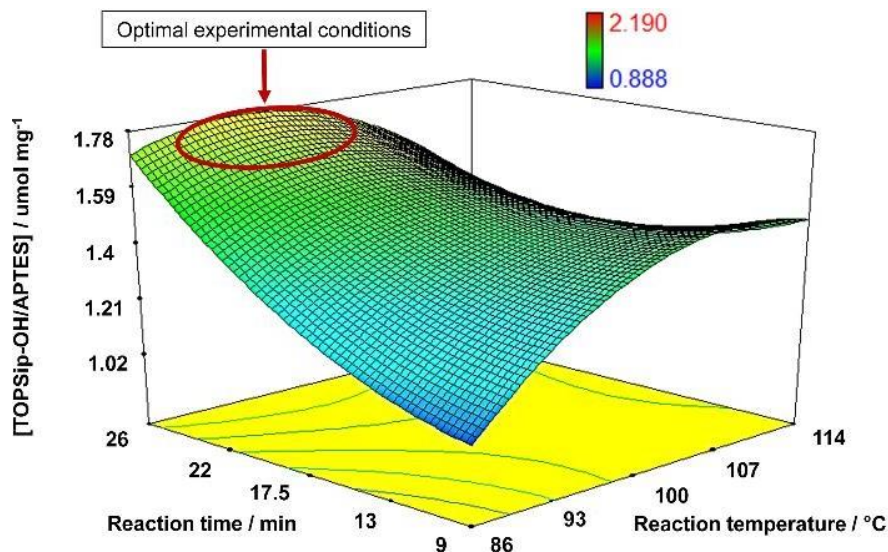


Fig. 5. Response surface plot of [TOPSip-OH/APTES] in uncoded values. Overlaid contour at optimal experimental conditions.

3.7 Thermogravimetric Analysis

The quantification of the amount of APTES grafted on the surface of three different samples of TOPSip-OH/APTES from the CDD was obtained by thermogravimetric analysis, the decrease in weight can be attributed to the organic degradation of APTES. The results are summarized in Table 4, while Fig. 6 shows the TGA curve for sample 1. The first amount of weight loss ($\sim 2.6\%$) derives from the removal of molecules with small molecular weight such as water, while the second major weight loss ($\sim 6.7\%$) involves the thermal decomposition of the APTES grafted on TOPSip-OH/APTES.

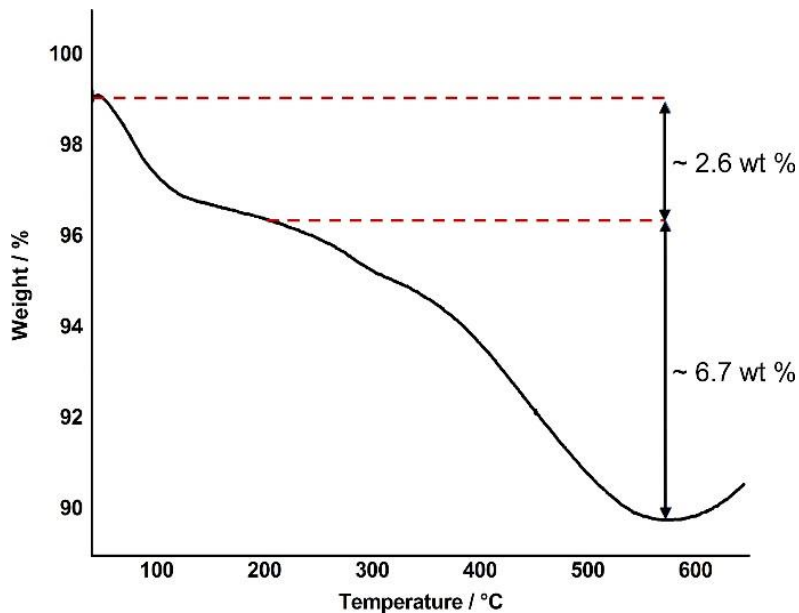


Fig. 6. Thermogravimetric analysis (TGA) curve of TOPSip-OH/APTES corresponding to sample 1 from Table 4.

The results from TGA were compared to those from NIHM quantification. The NIHM provides an estimate of the content of accessible amines, which may differ from the total amine content measured by TGA, resulting in differences ranging from 5 to 25 % (Table 4). Statistical significance between both methods was evaluated by paired t-test, with a level of significance $\alpha = 5\%$ ($P\text{-value} < 0.05$). The determination of the concentration of amino groups attached to the PSip surface by NIHM and TGA is not significantly different. This result was statistically confirmed with the $P\text{-value}$ obtained, which was higher than 0.05 ($P\text{ (to)} = 0.3719$). However, the differences obtained may be associated to two closely related events on the TOPSip-OH/APTES surface: slow diffusion flow of Ruhemann's purple through the smallest pores and APTES polymerization.

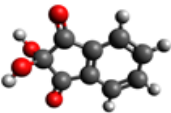
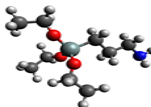
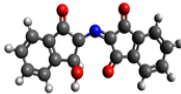
Table 4. $\mu\text{mol APTES g}^{-1}$ TOPSip-OH calculated by NIHM and TGA.

Sample	$\mu\text{mol APTES g}^{-1}$ TOPSip-OH		Difference (%)
	Ninhydrin method	Thermogravimetric analysis	
1	954	1153	17.25
2	1658	2203	24.73
3	2168	2065	4.96

Steric hindrance may be caused by some factors such as accumulation of Ruhemann's purple complex inside the pores. Ninhydrin is a small molecule and thus unable to induce pores blockage (Table 5). However, once ninhydrin reacts with APTES; the size of the formed complex is significantly bigger. The statistical pore size distribution in TOPSip-OH/APTES ranges from 30 to 80 nm (Fig. 1). However, pores with smaller diameter (< 30 nm) are susceptible to be blocked by Ruhemann's purple. We hypothesize that the purple complex moves outside the pore, but at the same time ninhydrin is diffusing into the pore to react with amino groups. This dynamic behaviour causes double flow inside the pore, which blocks or keeps inside some Ruhemann's molecules that are not completely released from TOPSip-OH/APTES and therefore are not measured during quantification. Similar observations were made in previous studies with non-porous particles. [41] In addition, the previously reported APTES polymerization has a significant influence. Typically, APTES is considered to attach to the surface as a monolayer, but a higher polymerization degree produces complex structures increasing steric hindrance inside the pore; as well as APTES reticulation causing interference in amino group quantification. [39,40] Hence it is likely that the combination of the factors discussed above contributes to the difference obtained by

TGA and NIHM measurements. Nevertheless, it is important emphasize that quantification of amino groups via NIHM evidences a more realistic accessibility; given that amino groups quantified by this technique demonstrates their availability to react with other molecules, which is important as they will be eventually used for posterior functionalization.

Table 5. Molecular structure and physicochemical properties.

Compound	Structure	M.W. (g mol ⁻¹) []]	Size X, Y, Z (Å) ^[a]	Volume (Å ³) ^[a]
Ninhydrin, C ₉ H ₄ O ₃		178.14	X= 8.97 Y= 7.61 Z= 5.28	135.82
APTES, C ₉ H ₂₃ NO ₃ Si		221.37	X=11.99 Y= 8.72 Z= 7.53	215.82
Ruhemann's purple, C ₁₈ H ₉ NO ₄		303.27	X= 15.74 Y= 7.84 Z= 4.63	215.82
[a] Data from UCSF Chimera. ⁴²				

4. CONCLUSIONS

In this work, the APTES functionalization of PSip under different reaction conditions using the classical and MW-assisted silanization methods was performed for comparison purposes. The main advantage of the MW-assisted method is the significant reduction in *R*_t when compared to the traditional method, moreover APTES surface coverage increased by 39 % using MW irradiation. It was found that silanol groups (Si-OH) promote higher efficiency of the amino silanization reaction.

The amino surface coverage increased 3-fold in hydroxylated microparticles when using a 5 % APTES solution. Surface modification was evidenced by FT-IR, STEM, and elements mapping; as well as ζ potential measurements. The optimization and modelling of APTES functionalization on TOPSip-OH were performed using a CCD. The observation of the surface contour plot of [TOPSip-OH/APTES] allows choosing the optimal experimental conditions to obtain the maximum APTES surface coverage on TOPSip-OH. APTES surface functionalization was found to strongly depend on the reaction time, reaction temperature and percentage of APTES. The optimal functionalization was obtained at middle-temperature values (95 °C); using 5 % APTES solution in dry toluene for 26 min.

The concentration of amino functional groups was quantified by the NIHM and confirmed by TGA. Comparing both results, we conclude that the former is an excellent alternative for amino groups quantification having several advantages over TGA such as the small amount of sample required, the low cost of the reagents, and the simpler equipment used. Besides, NIHM is highly reproducible and implies a relatively easy experimentation and data analysis. Since NIHM involves the direct reaction with amino groups; this method evidences a more realistic amine accessibility. Which is relevant since the quantified amino groups are further targeted in posterior functionalization reactions.

REFERENCES

1. W. Yan, M. Hu, D. Wang and C. Li, *Appl Surf Sci.*, 2015, 346, 216-222.
2. L. S. Jiao, J. Y. Liu, H. Y. Li, T. S. Wu, F. Li, H. Y. Wang and L. Niu, *J Power Sources*, 2016, 315, 9-16.
3. L. Meng, X. Zhang, Y. Tang, K. Su and J. Kong, *Sci Rep.*, 2015, 5, 7910.
4. J. Jiao, J. Cao, Y. Xia and L. Zhao, *Chem. Eng. J.*, 2016, 94, 223313.
5. H. A. Santos, L. M. Bimbo, B. Herranz, M. A. Shahbazi, J. Hirvonen and J. Salonen, *J. Mater. Res.*, 2103, 28, 152–164.

6. T. Tieu, M. Alba, R. Elnathan, A. Cifuentes-Rius and N. H. Voelcker, *Adv Ther.*, 2019, 2, 1800095.
7. D. Rocha-García, M. de L. Betancourt-Mendiola, A. Wong- Arce, S. Rosales-Mendoza, J. Reyes-Hernández and O. González-Ortega, G. Palestino, *Eur. Polym. J.*, 2018, 108, 485– 497.
8. W. Li, Z. Liu, F. Fontana, Y. Ding, D. Liu, J. T. Hirvonen and H. A. Santos, *Adv Mater.*, 2018, 30, 1703740.
9. R. Boukherroub, J. T. C. Wojtyk, D. D. M. Wayner and D. J. Lockwood, *J. Electrochem. Soc.*, 2002, 149, H59.
10. J. M. Buriak, *Chem Mater.*, 2014, 26, 763–772.
11. A. J. Nijdam, M. Cheng, D. H. Geho, R. Fedele, P. Herrmann, K. Killian, V. Espina, E. F. Petricoin, L. A. Liotta and M. Ferrari, *Biomaterials*, 2007, 28, 550–558.
12. M. P. Schwartz, F. Cunin, R. W. Cheung and M. J. Sailor, *Phys. Status Solidi Appl. Mater. Sci.*, 2005, 202, 1380–1384.
13. N. Majoul, S. Aouida and B. Bessaïs, *Appl. Surf. Sci.*, 2015, 331, 388-391.
14. D. Warther, Y. Xiao, F. Li, Y. Wang, K. Huffman, R. Freeman, M. Sailor, L. Cheng and R. Freeman, *Drug Deliv.*, 2018, 25, 1537– 1545.
15. E. Ma, L. M. Bimbo, M. Kaasalainen, B. Herranz, A. J. Airaksinen, M. Heinonen, E. Kukkk, J. Hirvonen, H. D. A. Santos and J. Salonen, *Langmuir*, 2012, 28, 14045-14054.
16. B. Xia, Q. Zhang, J. Shi, J. Li, Z. Chen and B. Wang, *Colloids Surfaces B Biointerfaces*. 2018, 164, 291–298.
17. A. Chaix, E. Cueto-diaz, A. Delalande, N. Knezevic, P. Midoux, J. Durand and F. Cunin, *RCS Adv.*, 2019, 5, 31895–31899.
18. M. Hiraoui, M. Guendouz, N. Lorrain, A. Moadhen, L. Haji and M. Oueslati, *Mater. Chem. Phys.*, 2011, 128, 151–156.
19. R. G. Acres, A. V. Ellis, J. Alvino, C. E. Lenahan, D. A. Khodakov, G.F. Metha and G. G. Andersson, *J. Phys. Chem. C.*, 2012, 116, 6289–6297.

20. K. Uvdal, R. Erlandsson and H. Elwing, *J. Colloid. Interf. Sci.*, 1991, 147, 103-118.
21. F. Kunc, V. Balhara, A. Brinkmann, Y. Sun, D. M. Leek and L. J. Johnston, *Anal. Chem.*, 2018, 90, 13322–13330.
22. A. Hennig, P. M. Dietrich, F. Hemmann, T. Thiele, H. Borchering, A. Hoffmann, U. Schedler, C. Jäger, U. Resch- Genger and W. E. S. Unger, *Analyst.*, 2015, 140, 1804–1808.
23. P. M. Dietrich, A. Hennig, M. Holzweber, T. Thiele, H. Borchering, A. Lippitz, U. Schedler, U. Resch-Genger and W. E. S. Unger, *J. Phys. Chem. C.*, 2014, 118, 20393–20404.
24. A. Hennig, H. Borchering, C. Jaeger, S. Hatami, C. Würth, A. Hoffmann, K. Hoffmann, T. Thiele, U. Schedler and U. Resch- Genger, *J. Am. Chem. Soc.*, 2012, 134, 8268–8276.
25. S. W. Sun, Y. C. Lin, Y. M. Weng and M. J. Chen, *J. Food. Compos. Anal.*, 2006, 19, 112–117.
26. M. Friedman, *J. Agric. Food. Chem.*, 2004, 52, 385–406.
27. S. Padmanabhan, J. E. Coughlin and R. P. Iyer, *Tetrahedron Lett.*, 2005, 46, 343–347.
28. F. Benyettou, E. Genin, Y. Lalatonne and L. A. Motte, *Nanotechnology*. 2011, 22, 055102.
29. M. E. Mahmoud, M. F. Amira, A. A. Zaghloul and G. A. A. Ibrahim, *Chem. Eng. J.*, 2016, 293, 200–206.
30. M. J. Sweetman, C. J. Shearer, J. G. Shapter and N. H. Voelcker, *Langmuir*, 2011, 27, 9497–9503.
31. G. Navarro-Tovar, D. Rocha-Garcia and A. Wong-Arce, *Materials*, 2018, 11, 1083.
32. C. B. Bottom, S. S. Hanna and D. J. Siehr, *Biomedical Education*, 1978, 6, 4-5.
33. G. Palestino, R. Legros, V. Agarwal, E. Pérez and C. Gergely, *B Chem.*, 2008, 135, 27–34.
34. C. P. Sreena, D. Sebastian and J. Genet. *Eng. Biotechnol.*, 2018, 16, 9-16.

35. T. K. Trinh and L. S. Kang, *Env. Eng. Res.*, 2010, 15, 63–70.
36. J. A. Howarter and J. P. Youngblood, *Langmuir*, 2006, 22, 11142–11147.
37. E. A. Smith and W. Chen, *Langmuir*, 2009, 24, 12405–12409.
38. R. M. Pasternack, S. R. Amy and Y. J. Chabal, *Langmuir*, 2008, 24, 12963–12971.
39. S. Lechevallier, P. Hammer, J. M. A. Caiut, S. Mazeret, R. Mauricot, M. Verelst, H. Dexpert, S. J. L. Ribeiro and J. Dexpert-Ghys, *Langmuir*, 2012, 28, 3962–3971.
40. Y. Chen and Y. Zhang, *Anal. Bioanal. Chem.*, 2011, 399, 2503–2509.
41. Y. Sun, F. Kunc, V. Balhara, B. Coleman, O. Kodra, M. Raza, M. Chen, A. Brinkmann, G. P. Lopinski and L. J. Johnston, *Nanoscale Adv.*, 2019, 1, 1598–1607.
42. E. F. Pettersen, T. D. Goddard, C. C. Huang, G. S. Couch, D. M. Greenblatt, E. C. Meng and T. E. Ferrin, *J. Comput. Chem.*, 2004, 25, 1605–1612.

CHAPTER 3

Design of functional P*Si*/CH composites: synthesis, characterization, and evaluation in therapeutics

ABSTRACT

In this work, the properties of chitosan were combined with those of porous silicon microparticles to design hybrid composites that can act as vehicles for transportation and sustained release of tramadol hydrochloride (TR), a potent analgesic. Porous silicon microparticles (PSip) with porosity of $87 \pm 3\%$, average pore size of 67 ± 17 nm, average size of 1 ± 0.31 μm and thickness of 0.5 ± 0.08 μm , were used as nanostructured material. Aldehyde or carboxylic acid functionalized PSip were mixed with a chitosan biopolymer to obtain chemically bonding composites. The physicochemical and morphological properties of UnPSip/CH and TOPSip-OH/A/G/CH nanostructured composites were characterized by Fourier transform infrared spectrometry (ATR-FTIR), ζ -potential techniques, transmission electron microscopy (TEM), and scanning electron microscopy (SEM). TR loading capacity in TOPSip-OH was quantified by UV-Vis spectroscopy obtaining 11 and 13 % for TOPSip-OH/A/G/CH and UnPSip/CH, respectively. TR release was carefully studied in simulated gastric fluid (pH 1.2) and simulated intestinal fluid (pH 6.8). From TR released profiles, it was observed that UnPSip/CH composite exhibited a more sustained release during 30 h when compared to TOPSip-OH/A/G/CH, showing a burst effect depending on pH. TR cumulative release data were fitted using Korsmeyer-Peppas model for both simulated fluids. Mucoadhesive studies of UnPSip/CH and TOPSip-OH/A/G/CH composites demonstrated a high interaction with mucin (mainly at pH 4.6) allowing absorption and effectiveness of TR.

1. INTRODUCTION

Drug delivery technology is a novel area for healthcare and its main objective is to approach the deficiencies of conventional drug delivery methods. The need to develop innovative technologies to improve the delivery of drugs to the body has been widely recognized. Based on this, nanotechnology has focused on the study of new novel strategies that may be useful for the oral administration of drugs [1]. It has been

observed that systems designed based on nanotechnology have presented better properties and several benefits, among them and one of the most important is the controlled release of drugs at a specific site. Other benefits are the modification of the systems surface with the aim of acquiring advantageous cellular interactions, providing a dual therapy with high synergistic therapeutic results, and protecting them from the harsh gastric conditions to which the drugs are exposed [2-4]. These new technologies are called drug delivery systems (DDS). Comparing these systems with conventional drug delivery methods, DDS allows to improve the efficacy of drugs due to their efficient and controlled administration [5]. The main objective in the development of DDS has focused on improving the dosage of the drug for prolonged periods, keeping its concentrations within the therapeutic window, improving patient compliance, safety, efficacy, and shelf life of the product [6]. In recent years, considerable research efforts have been directed to the development of drug delivery systems aimed at preventing and treating diseases such as Type II Diabetes mellitus [7], neurodegenerative diseases such as Parkinson's [8] and Alzheimer's [9], different types of cancer such as breast [10] and liver [11], SARS-COV-2 [12], among others.

In the last 10 years, mesoporous materials have shown high potential as DDS [13-15]. Mainly clays [16], silicas [17], graphene [18], carbon nanotubes [19], and porous silicon [20]. Porous silicon (PSi) is a mesoporous material with a high potential in drug delivery applications. This useful application is due to its physicochemical properties such as particle size modification, ranging from a few nanometers to microns, pore size adjustment, high surface area and degree of porosity, biodegradability and biocompatibility, and highly modifiable chemical surface [21]. Another advantage of this material is to protect the drugs from possible degradation, the drug loading process is carried out with minimal harsh conditions [15]. This advantage allows a wide variety of molecules to be incorporated into the PSi particles (PSip), ranging from proteins and peptides to drugs that are poorly and highly soluble in water. PSip have been shown to exhibit controlled drug release profiles with high payloads [22-24]. This information has been demonstrated in previous works. García-Briones et al., reported the design of nanostructured oxidized PSi microparticles were

successfully used as a sustained release vehicle for metformin (MET). The successful incorporation of MET was observed with an average loading percentage of 48% and a sustained release of MET was achieved over 26 h [7]. On the other hand, Salonen et al., demonstrated the loading of five drugs (ranitidine, griseofulvin, ibuprofen, antipyrine, and furosemide) onto thermal carbonization porous silicon microparticles (TCPSi). They investigated drug loading and release profiles in different media. Their results demonstrated that the chemical nature of the drugs is an important factor in loading efficiency, ranging from 9 to 45%. In contrast, dissolution of the drug affected the release rate of drugs loaded in TCPSi. The release rate was fast, reaching only 350 min [24]. The results of these works showed that a sustained drug release depends on the properties (particle size, pore size, surface chemistry) of the PSi particles and the chemical nature of the drug. In this framework, to obtain more controlled drug release profiles, different alternatives have been developed. One of them is the design of composites based on PSip with the addition of biopolymers [25]. Composites, also known as hybrid systems, are the result of the combination of at least two different materials. The new composites show a combination of advantageous properties that the individual components do not have [26].

One of the most widely used biopolymers is chitosan (CH). CH is a cationic polysaccharide, it has excellent biocompatibility, low toxicity, good delivery ability for hydrophilic molecules, and high loading, has excellent mucoadhesiveness, as well as antimicrobial properties [27]. Thus, CH modification of the PSip renders them mucoadhesive properties. This property allows the composites to remain in the mucosa (nasal/intestinal) for prolonged periods and thus improve the absorption of the drug in the mucosa. Besides, by increasing the mucoadhesion, CH enhances the intestinal permeability of biomacromolecules [28]. The combination of advantageous characteristics of PSip and CH allows to obtain a novel hybrid material tailored to applications in controlled drug delivery. In this sense, there are different investigations that demonstrate the applications and novel properties of PSip/CH hybrid composites with special interest in the controlled administration of drugs. Shrestha et al., designed hydrocarbonized thermally annealed PSi (AnnTHCPSi) microparticles and undecylenic

acid modified AnnTHCPSi (AnnUnTHCPSi) as vehicles for oral administration of insulin. AnnUnTHCPSi were modified with CH to increase intestinal permeation of insulin. Studies performed on Caco-2/HT-29 cell monolayers showed that CH-conjugated microparticles significantly increased insulin permeability, compared to pure insulin. Likewise, these materials were able to improve the absorption of insulin through intestinal cells, this result shows that microparticles conjugated with chitosan are an alternative for the oral administration of drugs, proteins, and peptides, through the intestinal cell membrane [29]. Additionally, Kafshgari et al., developed thermally hydrocarbonized pSiNPs (THCpSiNPs) and CH-coated THCpSiNPs for therapeutic oligonucleotide delivery. Oligonucleotide loading before CH coating was shown to provide sustained release oligonucleotide profiles with low burst effects. Furthermore, the chemical addition of CH improved the absorption of oligonucleotides through the cell membrane when they were loaded on THCpSiNPs [30].

In this study, two novel drug delivery systems based on PSip/CH were developed for the oral administration of tramadol: UnPSip/CH and TOPSip-OH/A/G/CH. Two different modification approaches were studied to obtain the composites. First, UnPSip were prepared by hydrosilylation of native porous silicon layers with UA, the presence of the carboxyl groups on the surface of UnPSip allowed further surface modification with CH via EDC/NHS coupling chemistry. Second, TOPSip surface was modified by a silanization process using APTES and GTA, the aldehyde groups on the surface of TOPSip-OH/A/G allowed surface modification with CH by direct reaction. The aim of this study was to investigate the effect of PSi/CH composites using different bridge (UA, APTES-GTA) to couple CH, on tramadol loading and in vitro tramadol cumulative release profiles. Furthermore, the mucoadhesive strength of the UnPSip/CH and TOPSip-OH/A/G/CH composites by mucin adsorption at different concentrations was evaluated. The physicochemical and morphological properties of UnPSip/CH and TOPSip-OH/A/G/CH composites were characterized by Fourier transform infrared spectrometry (ATR-FTIR), zeta potential, transmission electron microscopy (TEM), and scanning electron microscopy (SEM). TR release

profiles were studied under two different simulated fluids: gastric (pH 1.2) and intestinal (pH 6.8).

2. EXPERIMENTAL SECTION

2.1 Materials

Single-crystal boron-doped p-type Si wafers with resistivity $<0.005 \Omega \text{ cm}$ and crystallographic orientation of $\langle 100 \rangle$ were purchased from WRS materials. Aqueous hydrofluoric acid (HF, 48 %) and absolute ethanol (EtOH, 95.5 %) were acquired from Golden Bell Chemicals (Mexico) and Monfel Industries (Mexico), respectively. Sulfuric acid (H_2SO_4 , 98 %) and hydrogen peroxide (H_2O_2 , 30 %) were purchased from Karal (Mexico) and Avantor (Mexico). Tramadol hydrochloride (TR, 99 %) was supplied from Sigma-Aldrich (Mexico). 3-(Aminopropyl) triethoxysilane (APTES, $\geq 98 \%$) and glutaraldehyde (GTA, 25 % in water), N-Hydroxysuccinimide (NHS, $\geq 97 \%$) and 1-Ethyl-3-(3-dimethylaminopropyl) carbodiimide (EDC, $\geq 98 \%$), Medium molecular weight chitosan (CH, 75 - 85% deacetylated), 10-Undecenoic acid (UA, 98 %) and Mucin type III (0.5 – 1.5 % sialic acid) were purchased from Sigma-Aldrich (Mexico). Glacial acetic acid (AA, $\geq 99.7 \%$) was acquired from Jalmek. All reagents and solvents were used as received without any further treatment.

2.2 Synthesis of thermally oxidized porous silicon particles (TOPSip)

TOPSip were prepared by electrochemical anodization of p^{++} type boron-doped (100) oriented single crystal silicon wafer ($\leq 0.005 \Omega \text{ cm}$ resistivity) in an electrolyte solution of a 3:7 (v/v) mixture of HF (48%) and ethanol (99 %). The synthesis of TOPSip was performed in three steps: first porous silicon (PSi) layers were obtained by introducing a series of perforations in PSi layers during the electrochemical method. Electrochemical etching consisted in successively applying 40 cycles of two different current densities: a lower current density of 15 mA/cm^2 during 73 s and a higher current density of 50 mA/cm^2 for 3 s. PSi layers were lifted-off from the Si wafer via an

electropolishing step using ten pulses of 184 mA/cm² for five s each in 3.8 cm² area. After etching, the PSi layers were rinsed three times with EtOH. Second, free-standing PSi layers were fractured in fresh EtOH using an ultrasonic tip (SONICS Vibra-Cell, 30% amplitude) for 60 min at 25 °C. Finally, the obtained porous silicon particles (PSip) were stabilized by thermal oxidation (TOPSip) in a furnace (Carbolite) for 45 min at 450°C under ambient air; with a ramp rate of 10 °C/min [31].

2.3 Surface modification

2.3.1 Modification P*Si* layers with UA

Native P*Si* layers were modified by hydrosilylation method using UA as described below to obtain UnPSip. In this case, approximately 60 mg of freshly prepared P*Si* layers, slightly dried at room temperature, were placed in 50 mL of UA and allowed to react at 120 °C for 16 h using mechanical stirring and reflux. After hydrosilylation, the UA functionalized porous layers were rinsed with absolute ethanol (five times) to remove excess UA that did not react [32]. In this reaction, through the application of heat, Si-C bonds are formed between the hydrides (Si-H_x) of the newly synthesized P*Si* layers and the unsaturated bond (C=C) of UA. Hydrosilylation of porous layers provides carboxylic acid functional groups that can react covalently, by activation, with the primary amino groups of chitosan [33]. For obtain UA functionalized P*Si* microparticles (UnPSip), UA functionalized P*Si* layers were fractured in fresh EtOH using an ultrasonic tip (SONICS Vibra-Cell, 30% amplitude) for 60 min at 25 °C (Fig. 1A).

Finally, acid-base titration was used to determine total carboxyl acids content of the UnPSip adapting the method for hydrogel films introduced by Mali [34]. About 2.5 mg of UnPSip was dissolved in 1 mL 0.1 N NaOH for 24 h with magnetic shaking. Subsequently, phenolphthalein was added as an indicator and the excess NaOH was titrated with 0.1 N HCl. The carboxyl acids content in equivalents/mg of UnPSip was calculated using the following eq. (1):

$$\text{Carboxyl acids content} = \frac{(V_b - V_a) \times N}{W} \quad (1)$$

where, N is the normality of HCl (eq/L), V_b and V_a are the volumes of HCl without and with of sample, and W is the weight of sample (g).

2.3.2 Modification TOPSip with APTES and GTA

The surface of the TOPSip was further modified by silanization method using APTES as described below to obtain TOPSip-OH/A. To promote a high efficiency of chemical binding between TOPSip and APTES, TOPSip were modified through a hydroxylation process. The silanization method and the conditions used were described in our previous report [31]. After silanization, TOPSip-OH/A were functionalized with GTA. The objective of this second functionalization is to introduce aldehyde functional groups, these groups can react directly, through covalent bonding, with the primary amino groups of CH. 20 eq of GTA were added for each eq of primary amino groups present in the TOPSip-OH/A. The reaction mixture was stirred at 130 rpm for 30 min at room temperature. Subsequently, the reaction mixture was centrifuged and the TOPSip-OH/A/G were recovered, three rinses with deionized water (DI) were carried out to eliminate the unreacted GTA. In each rinse, the TOPSip-OH/A/G were centrifuged at 5500 rpm for 5 min. Fig. 1B shows the functionalization steps to produce TOPSip-OH/A/G.

Quantification of amino groups grafted on the TOPSip-OH/A surface before and after the functionalization with GTA was performed by the ninhydrin method. The same procedure was performed as in our previous report [31].

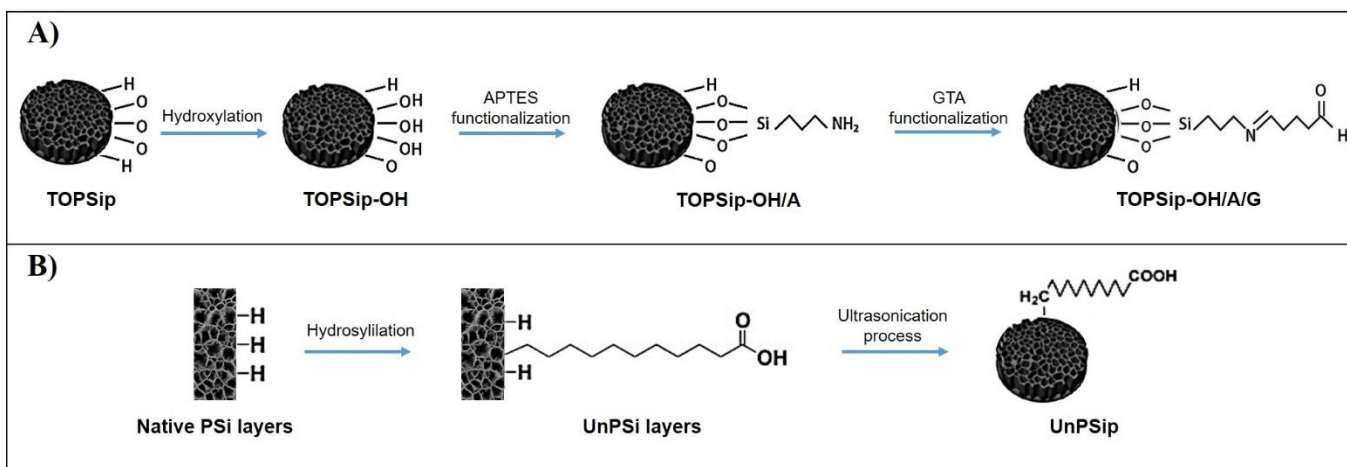


Fig. 1. Functionalization steps of A) TOPSip-OH (thermal oxidation), TOPSip-OH/A (silanization), and TOPSip-OH/A/G (functionalization with glutaraldehyde). B) UnPSi layers (hydrosilylation) and UnPSip (ultrasonication process).

2.4 Drug loading

For the drug loading, a ratio of 5:1 (w/w) was used for tramadol-loaded UnPSip (UnPSip/TR) and tramadol-loaded TOPSip-OH/A/G (TOPSip-OH/A/G/TR). The tramadol loading was performed by dispersing 5 mg of UnPSip or TOPSip-OH/A/G in 1 mL of a tramadol solution (25 mg/mL in aqueous solution). The suspensions were stirred using an orbital shaker at 130 rpm 24 h. Tramadol adsorption on the UnPSip and TOPSip-OH/A/G surface and pores was promoted by intermolecular interactions between the functional groups of TR (-OH, -NHR₃⁺-) and surface UnPSip groups (SiO⁻, -COOH) (Fig. 2A) and surface TOPSip-OH/A/G groups (OH, -CHO, -NH₂) (Fig. 2B). At the end of the tramadol adsorption, TOPSip-OH/A/G/TR and UnPSip/TR were functionalized with chitosan without previous centrifugation.

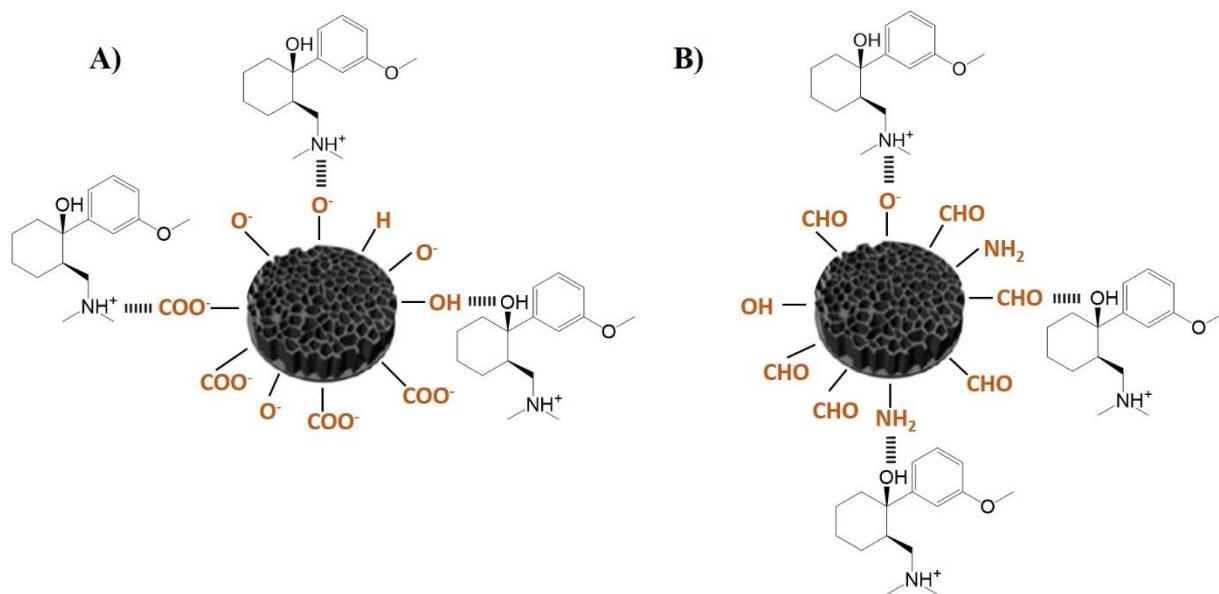


Fig. 2. Intermolecular interactions between the functional groups of TR and A) surface UnPSip groups and B) surface TOPSip-OH/A/G groups.

2.5 Synthesis of PSip/CH Composites

The synthesis of PSip/CH composites was performed by evaluating two methods: in the first, the PSi layers were functionalized with UA to promote chemical binding with the polymeric chains of chitosan. The second method was carried out by functionalizing the TOPSip with APTES and GTA. This was done to compare the performance of the chitosan layer in the release of tramadol.

2.5.1 Synthesis of UnPSip/CH composites

The chemical binding between the free primary amine groups in the chitosan structure with the carboxylic acid groups of UnPSip/TR was carried out in acetate buffer (pH 5) using EDC/NHS as activators. In this case, 2.5 mL of acetate buffer (pH 5) was added to the UnPSip/TR loading solution (~ 5 mg UnPSip and 1 mL tramadol solution). Then, 3 eq of EDC and NHS were added to this dispersion for each eq of carboxylic acid and mixed for 2 h at room temperature to activate the carboxylic acids on the

UnPSip. After activation, 2.5 mL of the chitosan solution (4 mg/mL) was added and stirred overnight at 130 rpm and room temperature to allow conjugation. The UnPSip/TR/CH were then centrifuged at 4000 rpm for 2 min to remove the unreacted CH. Next, UnPSip/TR/CH were washed two times with 0.01% acetic acid and deionized water (DI). Finally, the UnPSip/TR/CH composites were dried at room temperature. Using this methodology, a part of the TR was adsorbed in the UnPSip and another part was encapsulated in the polymeric chains of the CH.

2.5.2 Synthesis of TOPSip-OH/A/G/CH composites

The chemical binding between the free primary amine groups in the chitosan structure with the aldehyde groups of TOPSip-OH/A/G/TR was performed in acetate buffer (pH 5). In this case, 5 mL of the chitosan solution (2 mg/mL in buffer pH 5) was added to the TOPSip-OH/A/G/TR loading solution (~ 5 mg TOPSip-OH/A/G and 1 mL tramadol solution). The reaction mixture was stirred overnight at 130 rpm and room temperature. The TOPSip-OH/A/G/TR/CH were then centrifuged at 4000 rpm for 2 min to remove the unreacted CH. Next, TOPSip-OH/A/G/TR/CH were washed two times with 0.01% acetic acid and deionized water (DI). Finally, the TOPSip-OH/A/G/TR/CH composites were dried at room temperature. Using this methodology, a part of the TR was adsorbed in the TOPSip-OH/A/G and another part was encapsulated in the polymeric chains of the CH.

2.6 In vitro drug release study

TR release profiles were performed by dispersing 2 mg of each set of TOPSip-OH/A/G/TR/CH or UnPSip/TR/CH in 0.5 mL of KCl/HCl buffered solution (pH 1.2) or acetates buffered solution (pH 6.8) under sink conditions at $37 \text{ }^{\circ}\text{C} \pm 2 \text{ }^{\circ}\text{C}$, simulating the TR process desorption in the human organism. At different times, a buffered solution with TOPSip-OH/TR was centrifuged at 12,000 rpm to separate the released TR from composites, and sampled aliquots from the supernatant (0.4 mL) were

collected. The concentration of the released TR was measured spectrophotometrically (Agilent Technologies, Cary 60 UV–Vis) at 271 nm (maximum absorption of TR) using external standard calibration curves in both buffered solution in the range from 5 to 100 ppm ($R^2 = 0.999$). Based on the sink conditions protocol, aliquots were replaced with fresh buffer (0.4 mL) after measurement.

2.7 Adsorption of mucin on PSi/CH composites

Mucoadhesiveness was calculated as the amount of mucin adsorbed by each set of PSi/CH composites in a determined time. The % binding efficiency of PSi/CH composites to mucin was determined by mixing 1 mL of type III porcine mucin solution (1, 3 and 5 mg/mL) with the same volume of PSi/CH composites suspensions (1 mg/mL). Equal volumes of PSi/CH composites suspensions and porcine mucin solution were incubated at $37\text{ }^\circ\text{C} \pm 2\text{ }^\circ\text{C}$ for 5 h until equilibrium was reached. The adsorptions were carried out in KCl/HCl buffered solution (pH 1.2) or acetates buffered solutions (pH 4.6 and 6.8). At different time, the suspensions were centrifuged at 12000 rpm and free porcine mucin in the supernatant was measured by spectrophotometrically (Agilent Technologies, Cary 60 UV–Vis) at 260 nm (maximum absorption of porcine mucin) using external standard calibration curves in both buffered solutions. The % mucin binding efficiency of composites was calculated from the following eq. (2) [35, 28]:

$$\text{Mucin binding efficiency (\%)} = \frac{\text{Total mucin} - \text{Free mucin}}{\text{Total mucin}} \times 100 \quad (2)$$

2.8 Physicochemical characterization of PSi microparticles and composites

2.8.1 Scanning electron microscopy (SEM)

High-resolution scanning electron microscopy (HR-SEM) micrographs of TOPSip, TOPSip-OH/A/G/CH and UnPSip/CH were obtained using a field emission microscope (Dual Beam FIB/SEM FEI-Helios Nanolab 600) at accelerating voltage of

5 kV and 86 pA with a spot size of 4.0 mm and backscattered and secondary electrons. 100000 × magnifications were used.

2.8.2 Transmission electron microscopy (TEM)

High-resolution transmission electron microscopy micrographs and elements mapping analyses of TOPSip, TOPSip-OH/A/G/CH and UnPSip/CH were obtained using a microscope HRTEM/STEM JEOL JEM-2100 operated with acceleration voltage at 200 kV and resolution of 0.14 nm at 40000 x magnification.

2.8.3 Fourier transform infrared spectrometry (ATR-FTIR)

Attenuated total reflectance Fourier transform infrared (ATR-FTIR) spectroscopy was used to characterize the functional groups on the PSi layers and TOPSip surface, and in each synthesis step to produce UnPSip/TR/CH and TOPSip-OH/A/G/TR/CH. Agilent Cary 600 Series FTIR instrument equipped with a Slide-On diamond ATR device were used to record the spectra. The recording was performed with a resolution of 4 cm⁻¹, 32 scans, in an interval of 4000 and 500 cm⁻¹, and at room temperature.

2.8.4 ζ-potential

Stability and the surface zeta potential distribution (ζ-potential) of each synthesis step of composites were measured as a function of pH on a Zetasizer Nano ZS (Malvern Instruments) using electrophoretic light scattering (ELS). Isoelectric points (IEP) were determined in the pH value where potential reaches a neutral charge (zero value). Zeta potential measurements were performed by adding 2 mg of each set of microparticles in different vials, then 1 mL of the desired buffer solution was added: KCl/HCl (pH 1 – 2), acetates (pH 3 – 6), phosphates (pH 7 – 8), borax/HCl (pH 9), carbonates (pH 10 – 11) and KCl/NaOH (pH 12). All suspensions were strongly mixed,

using an ultrasonic bath (Branson) for 20 minutes to disperse the particles and 4 hours later, the supernatants of each vial were measured. Isoelectric point analysis was carried out in triplicate for each sample at room temperature.

Stability and the surface zeta potential distribution (ζ -potential) were measured as a function of pH using electrophoretic light scattering (ELS) on a Zetasizer Nano ZS (Malvern Instruments), of each synthesis step of composites. Isoelectric points (IEP) were determined in the pH value where potential shows a zero value (neutral charge). ζ -potential measurements were carried out in different vials, 2 mg of each set of microparticles and 1 mL of the desired buffer solution were added: pH 1 (KCl/HCl), pH 3 (acetates), pH 7 (phosphates), and pH 9 (borax/HCl). All suspensions were strongly mixed, using an ultrasonic bath (Branson) for 20 minutes to disperse the particles, and 4 hours later, the supernatants of each vial were measured. Isoelectric point analysis was carried out at room temperature; measurements were acquired in triplicate for each sample.

3. RESULTS AND DISCUSSION

In this study, two different chemical conjugation techniques used to modify the surface of PSi microparticles were compared. In the first technique, the activated carboxylic groups of the UnPSip were attached, by chemical conjugation, to the primary amine groups of CH, this reaction provides amide bonds using EDC/NHS coupling. In the second technique, the aldehyde groups of TOPSip-OH/A/G react covalently with the primary amino groups of CH, forming imine bonds.

3.1 Morphological characterization of TOPSip and PSip/CH composites

The morphological characterization of TOPSip is shown in Chapter 2, Section 3.1. In summary, TOPSip shows irregularly shaped microparticles, with an average size of $1.02 \pm 0.41 \mu\text{m}$. The TOPSip thickness was found to be $0.48 \pm 0.08 \mu\text{m}$, while the average porosity was calculated as $87 \pm 3 \%$. Moreover, it was demonstrated that

TOPSip surface was composed of a porous network of straight pores with an average pore size of 67.43 ± 28.64 nm (Fig. 3A).

To evaluate the structure of the composites, samples of the UnPSip/CH and TOPSip-OH/A/G/CH composites were analyzed by Scanning Electron Microscopy. From Fig. 3B,C it is observed that the UnPSip/CH and TOPSip/A/G/CH composites exhibit a similar porous structure like to the TOPSip. Although significant changes were made to the surfaces of the UnPSip/CH and TOPSip-OH/A/G/CH, the SEM images of the composites did not reveal any remarkable changes in morphology of the composites and absence of pore blockage was observed after chemically grafting CH to the surface of UndPSip and TOPSip-OH/A/G.

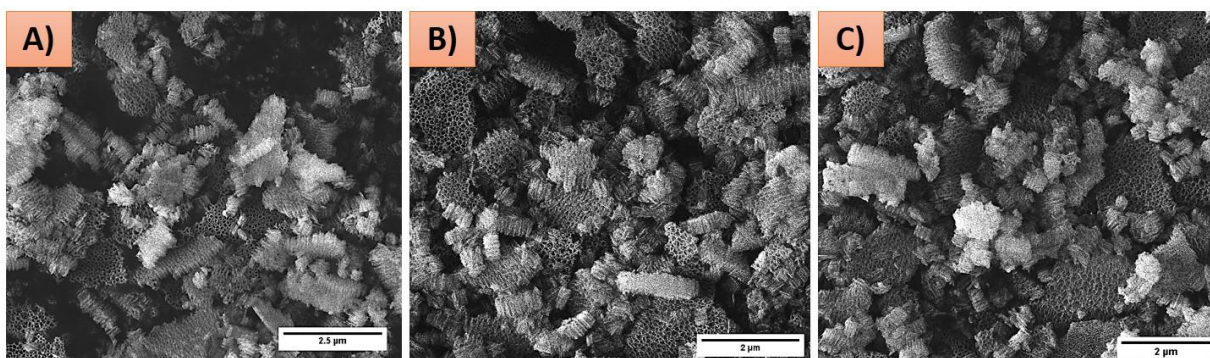


Fig. 3. HR-SEM micrographs of A) TOPSip, B) UnPSip/CH and C) TOPSip-OH/A/G/CH composites.

The element mapping analyses by scanning transmission electron microscope (STEM) of TOPSip and UnPSip/CH and TOPSip-OH/A/G/CH composites are shown in Fig. 3. This study was carried out to confirm the chemical grafting of CH in PSip. Fig. 4A evidences the structure and element distribution of TOPSip. The bright blue and green spots indicate the presence of silicon and oxygen, respectively; the characteristic elements of TOPSip, and absence of carbon and nitrogen. After chemical grafting of CH in UnPSip (Fig. 4B) and TOPSip-OH/A/G (Fig. 4C), changes in the morphology of the composites were observed. Fig. 3b and 3c demonstrated that the composites surface presents an organic layer of CH that unfocus the porous structure of the PSip.

Carbon and nitrogen are observed over the surface of UnPSip/CH and TOPSip-OH/A/G/CH; these findings confirm that CH was homogeneously chemical grafted all over the PSip surface.

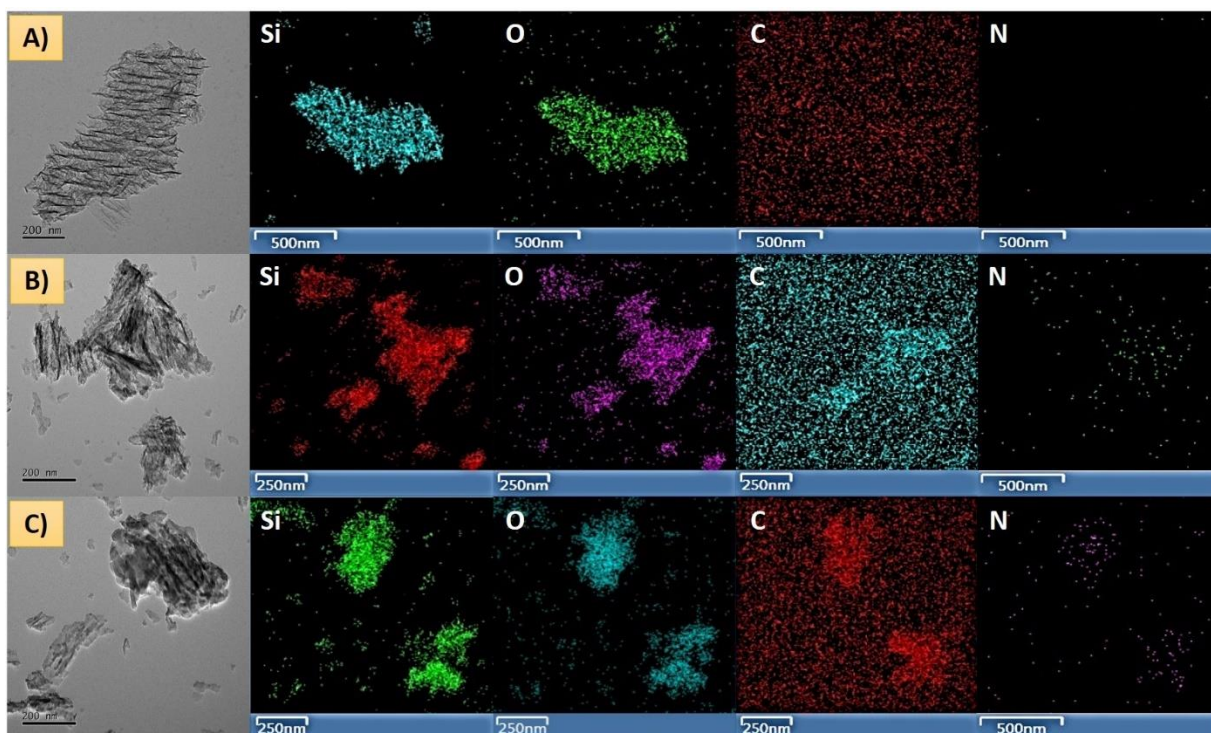


Fig. 4. STEM image and elemental mapping of A) TOPSip, B) UnPSip/CH and C) TOPSip-OH/A/G/CH.

The total carboxyl acids content of UnPSip was found to be 1.6 mEq/g of UnPSip. This result was used to calculate the amount of EDC and NHS required to activate the carboxylic acids of UnPSip. On the other hand, quantification of primary amino groups grafted on the TOPSip-OH/A and TOPSip-OH/A/G surface after functionalization with GTA was performed by the ninhydrin method. The concentration of primary amino groups grafted on the TOPSip-OH/A and TOPSip-OH/A/G was 1.8 ± 0.09 and 0.34 ± 0.07 $\mu\text{mol}/\text{mg}$, respectively [31]. Finally, an efficiency of functionalization of primary amino groups with GTA of 81% was obtained.

3.2 FT-IR of UnPSip/CH and TOPSip-OH/A/G/CH before and after TR loading

Chemical modifications on PSip surface after each synthetic step and the TR loading were confirmed by Fourier transform infrared spectroscopy (ATR-FTIR).

Fig. 5A shows the FTIR spectra of the synthesis steps of the UnPSip/CH composite. Native PSi layers exhibit several vibration bands: at 2136, 2085 and 2107 cm^{-1} assigned to $\nu(\text{SiSiH}_3)$, $\nu(\text{Si}_2\text{SiH}_2)$ and $\nu(\text{Si}_3\text{SiH})$, respectively. Other vibration bands assigned to $\delta(\text{SiH}_2)$, $\delta(\text{SiH}_x)$ and bulk $\nu(\text{Si-Si})$ are observed at 907, 660, 621 cm^{-1} [36]. After hydrosilylation of the PSi layers with UA, the UnPSip spectra displays several vibration bands: at 1711 cm^{-1} characteristic to the $\nu(\text{C=O})$ of the carboxylic acid, at 1460, 2927 and 2857 cm^{-1} assigned to $\delta(\text{CH}_2)$, $\nu_{\text{sym}}(\text{CH}_2)$ and $\nu_{\text{asym}}(\text{CH}_2)$ of the aliphatic groups, respectively. Besides, at 1066 cm^{-1} a characteristic band of silicon oxide formed during hydrosilylation is observed [37]. The appearance of the vibrational bands characteristic of amide I and II bands at 1654 and 1561 cm^{-1} , respectively, confirm the covalent binding of CH to UnPSip. Due to the reaction of the carboxylic acid groups of the UnPSip with the primary amino groups it is observed that the band at 1708 cm^{-1} assigned to $\nu(\text{C=O})$ weakens. The appearance of $\delta(\text{NH}_2)$ band at 1542 cm^{-1} also confirms the presence of amine groups in the UnPSip/CH. The band formed at 3377 cm^{-1} is associated to both the $\nu(\text{OH})$ from the CH, and the $\nu(\text{NH})$ from the amine functions on CH that remained unreacted, as well as $\nu(\text{NH})$ from the secondary amides. The strong band at 1047 cm^{-1} is assigned to the $\nu(\text{Si-O})$, although the contribution of the $\nu(\text{C-O})$ in the CH, which appears in the same region, cannot be excluded [37, 38]. The spectrum of TR loaded UnPSip shows bands attributed to characteristic groups of TR. Absorption bands at 701 and 1488 cm^{-1} corresponds to $\delta(\text{OH})$ and $\delta(\text{CH}_3)$, respectively. The absorption band at 1290 cm^{-1} corresponds to $\nu(\text{C-N})$, while at 1246 cm^{-1} is characteristic of $\nu(\text{CO})$. In addition, bands attributed to aromatic compounds: at 1579 cm^{-1} $\nu(\text{CH})$ and at 1601 cm^{-1} $\nu(\text{C=C})$ [39, 40].

On the other hand, Fig. 5B shows the FTIR spectra of the synthesis stages of the TOPSip-OH/A/G/CH composite. After silanization of TOPSip-OH with APTES, the TOPSip-OH/A spectra exhibits bands attributed to the presence of the amino-silane

molecule: 3356 cm^{-1} $\nu_{\text{asym}}(\text{N-H})$, 3282 cm^{-1} $\nu_{\text{sym}}(\text{N-H})$, 1564 and 1484 cm^{-1} $\delta(\text{N-H})$ belonging to NH_2 , and 2922 cm^{-1} $\nu_{\text{sym}}(\text{C-H})$ and 2874 cm^{-1} $\nu_{\text{asym}}(\text{C-H})$ characteristic of CH_2 groups confirming the total functionalization of the TOPSip-OH [31]. The spectrum of TOPSip-OH/A/G shows a specific vibration band at 1639 cm^{-1} suggested to the imine groups (C=N) [41]. The vibration bands associated with $\nu(\text{NH}_2)$ weaken, indicating that GTA functionalization was not fully carried out. The appearance of $\delta(\text{NH}_2)$ band at 1550 cm^{-1} and the preservation of the band attributed to the presence of the imine groups (1639 cm^{-1}) confirm the covalent binding of CH to the aldehyde groups of TOPSip-OH/A/G. The broad band formed at 3383 cm^{-1} is associated to the $\nu(\text{OH})$ from the CH and the absorption band at 1408 cm^{-1} corresponds a $\nu(\text{C-N})$ of CH. The strong band at 1055 cm^{-1} can be assigned to the contribution of $\nu(\text{Si-O})$ of the TOPSip-OH/A/G and $\nu(\text{C-O})$ in the CH [38, 42]. The spectrum of TR loaded TOPSip-OH/A/G/TR shows new bands attributed to characteristic groups of TR. Absorption bands at 1581 and 1602 cm^{-1} corresponds to $\nu(\text{CH})$ and $\nu(\text{C=C})$, respectively, which are attributed to aromatic compounds [39, 40].

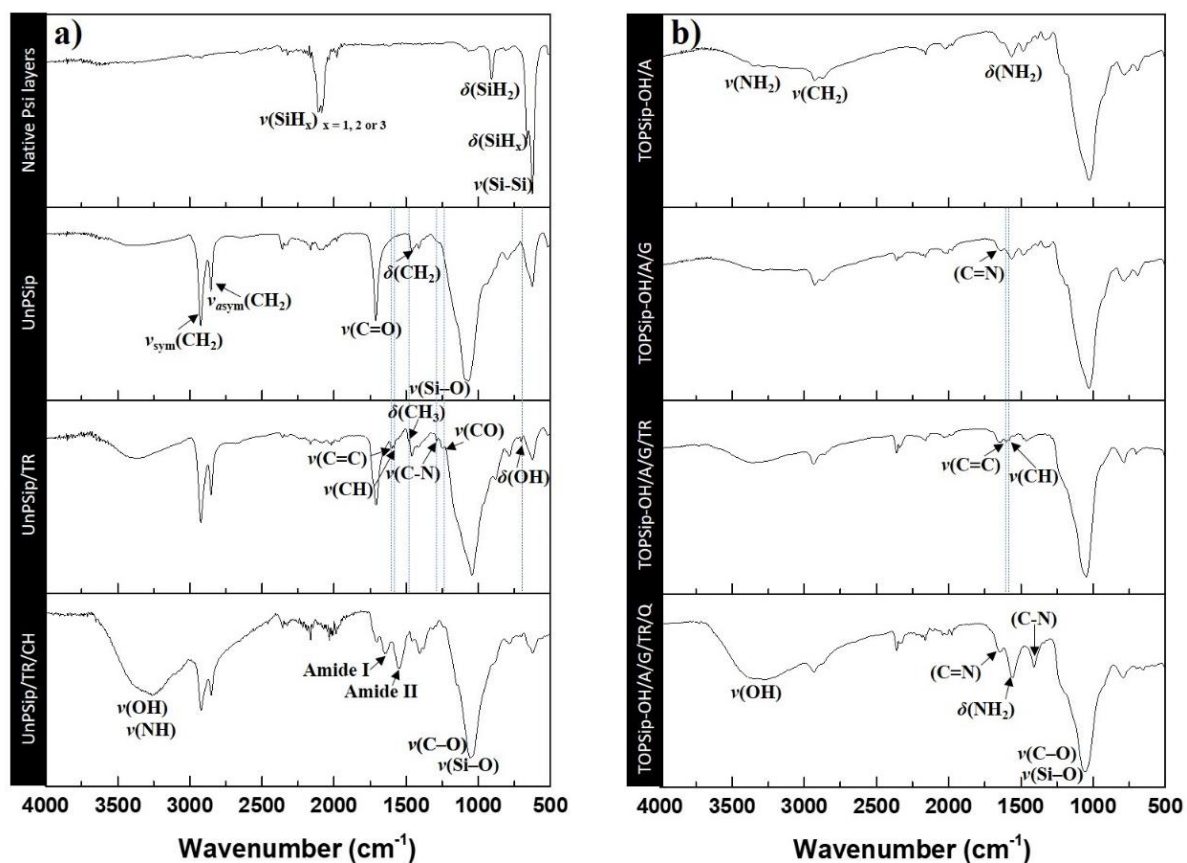


Fig. 5. ATR Fourier transform infrared spectra of each synthetic step in the synthesis of composites as well as TR loading: A) UnPSip/TR/CH and B) TOPSip-OH/A/G/TR/CH.

3.3 ζ -potential analysis

ζ -potential as a function of pH and surface chemistry was studied by using different buffered PSl microparticles suspensions. Fig. 6 presented the characteristic curves and the isoelectric points (IP). The titrations were made in each synthetic step and after TR loading. The results show differences in the IPs between PSl microparticles with different surface chemistries.

Fig. 6A shows the titration curves of the synthesis steps of the UnPSip/TR/CH composite. In the case of UnPSip, no IP value was observed compared to that reported for surfaces that have been hydrosilylated with UA [43]. UA has a pKA of 5.02 [44],

however, the variation between the reported value and the obtained value in this case, can be attributed to a poor reaction between native PSi layers coated with hydrides and AU chains; due to the length of the chains and the diameter of the pores, steric impairment may have occurred, which may have resulted in a low hydrosilylated and oxidized SiP surface due to hydrosilylation conditions. In this way, the potential is a function of the -OH, -O, and -H groups corresponding to surface oxidation and -COOH groups present at the end of the UA chain. So, the presence of -COOH and -OH groups on the UnPSip surface provided a strongly negative charge. After chemical binding between the carboxylic acid groups of UnPSip and the free primary amine groups in the CH shifted the IP of the composites to higher (~ 6) values. This important change is attributed to the protonation of the primary amino groups of the CH in acid solutions [45]. The features of the ζ -potential curve for UnPSip/CH show ζ -values lower than ± 30 mV from pH 1 to 9, denoting unstable suspensions. TR physical adsorption in UnPSip (UnPSip/TR) displays changes in ζ -potential. An IP value was observed of 3.4, this change is attributed to the physical adsorption of TR molecules on UnPSip surface. Silanol (Si-OH), siloxane (SiO⁻) and carboxylic (-COOH) surface groups from UnPSip can form intermolecular physical bonds with hydroxyl (OH) and protonated tertiary amino (R-NH⁺(CH₃)₂) functional groups from TR depending on the medium pH. Finally, addition of CH to UnPSip/TR (UnPSip/TR/CH) did not cause a significant change in ζ -value comparative with UnPSip/CH. These results indicate that the TR molecules are covered by the CH layer.

Fig. 6B shows the titration curves of the synthesis steps of the TOPSip-OH/A/G/TR/CH composite. Titration curves of the TOPSip-OH and TOPSip-OH/A were already discussed in our previous report [31]. After the silanization of TOPSip-OH with APTES shifted the IP of the TOPSip-OH to higher (6.3) values. This behavior is explained by the decrease in the number of free silanol groups (Si-OH) that were coupled through the formation of siloxane bonds with APTES molecules. The primary amine groups on the surface of TOPSip-OH/A are protonated, which appears to be highly favored at acidic pH values [46]. After covalent binding of GTA to TOPSip-OH/A through imine bond formation, the IP value of TOPSip-OH/A/G shifted to lower values

(~ 5.9). For these structures, the curve remains positive at pH below 5.9. The TOPSip-OH/A/G surface is terminated by aldehyde groups, a non-ionizable functional group [47]. However, although the aldehyde group is not ionizable, the presence of IP at 5.9 and slightly positive charges are attributed to a small amount of unreacted NH_2 groups that remain free on the TOPSip-OH/A/G surface after GTA binding, as shown described in section 3.1. After pH 5.9, TOPSip-OH/A/G became negative due to the free Si-O^- that were not attached by siloxane bond with amino-silane molecules. Finally, chemical binding between the imine groups of TOPSip-OH/A/G with the free primary amine groups in the chitosan structure does not show significant shift in IP, which is ~ 6. In contrast, for TOPSip-OH/A/G/CH composites, the titration curve is more positive at pH below 6. After chemical binding between TOPSip-OH/A/G and CH, TOPSip-OH/A/G/CH surface displays primary amino groups that are protonated in acid solutions [45]. Although it was expected that these composites would show highly positive charges and a shifted at higher IP, a small amount of unreacted aldehyde groups that remain free on the TOPSip-OH/A/G/CH surface do not allow further protonation. The features of the ξ -potential curve for UnPSip/CH show ξ -values lower than ± 30 mV from pH 1 to 9, denoting unstable suspensions. TR physical adsorption on TOPSip-OH/A/G (TOPSip-OH/A/G/TR) does not show significant shift in IP. An increase in positive charges was observed at pH values lower than 5. This change is attributed to the physical adsorption of TR molecules on the surface of TOPSip-OH/A/G. Aldehyde, silanol and amino surface groups from TOPSip-OH/A/G can form intermolecular physical bonds with hydroxyl (OH) and protonated tertiary amino ($\text{R-NH}^+(\text{CH}_3)_2$) functional groups from TR depending on the medium pH. The addition of CH to TOPSip-OH/A/G/TR (TOPSip-OH/A/G/TR/CH) shifted the IP to higher (~ 6.2) values cause a change in ζ -value comparative with TOPSip-OH/A/G/CH. These results show that not all TR molecules are covered by the CH layer, some of them are found on the surface of the composite.

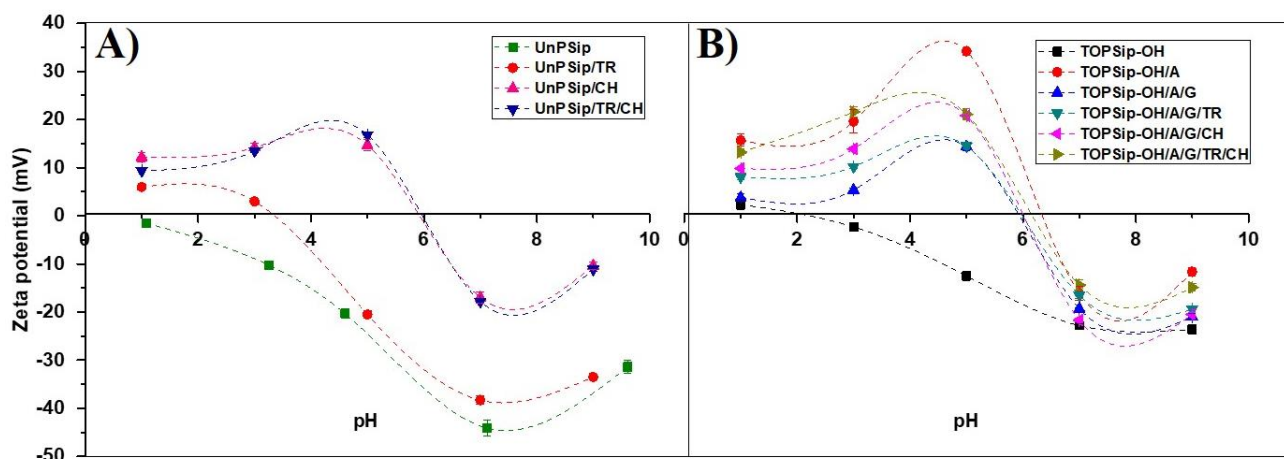


Fig. 6. ζ -potential curve vs pH for each synthetic step as well as TR loading for A) UnPSip-/TR/CH and B) TOPSip-OH/A/G/TR/CH.

3.4 Mucoadhesive strength of UnPSip/CH and TOPSip-OH/A/G/CH composites

The mucoadhesive strength of UnPSip/CH and TOPSip-OH/A/G/CH composites to bind to the mucosal surfaces was estimated by calculating binding efficiency of mucin to composites. The mucoadhesive strength was determined in SGF, in SIF and acetates buffered solution pH 4.6.

As shown in Fig. 7, the highest mucoadhesive strength was obtained in buffered solution pH 4.6, followed by SGF and finally in SIF, for both composites. The decrease in the mucoadhesive strength of composites in SIF compared to other fluids is mainly due to electrostatic repulsion force between composites and the mucosal surface. Mucins, highly glycosylated proteins, are the main component of mucosal surface [48]. They have an IP between 2 and 3 [49], so in solutions where pH > IP are negatively charged (mainly by sialic acid), promoting electrostatic repulsion forces between them, and giving rise to a more extended conformation of the chain [50]. On the other hand, UnPSip/CH and TOPSip-OH/A/G/CH composites are negatively charged as demonstrated by ζ -potential in Fig. 6. These composites are covered by a layer of CH. CH has, in general, a pKa around 6.1, therefore, at a pH higher than pKa, the amine group in the N-acetyl-glucosamine units is not protonated [51]. Therefore, in SIF,

UnPSip/CH shows a negative charge due to residues of unreacted carboxylic acid groups (-COOH) that are dissociated as carboxylate ion (-COO⁻) and to some siloxane groups (SiO⁻). In the case of TOPSip-OH/A/G/CH the negative charge comes from residues of siloxane groups (SiO⁻) after silanization. Consequently, the negative charges of composites cause electrostatic repulsion when they are into contact with negatively charged mucin. However, the mucoadhesive strength obtained could be due to the hydrophobic interactions between the hydrophobic domains in mucins and the acetyl groups in chitosan, as has been studied in other works [52].

On the other hand, an increase in the mucoadhesive strength of composites was observed in SGF (Fig. 7). In SGF, where pH < IP the mucin is in its neutral form, giving rise to a more compact conformation of the chain. At this pH, UnPSip/CH and TOPSip-OH/A/G/CH composites present a positive charge due to the protonation of primary amino groups of CH and of unreacted from APTES. The mucoadhesive strength obtained due to the hydrophobic interactions between the hydrophobic domains in mucins and the acetyl groups in chitosan.

Finally, the mucoadhesive strength was evaluated in acetates buffered solution pH 4.6 simulating the pH of the duodenum. The duodenum is the initial portion of the small intestine and is where absorption begins [53]. Therefore, it was considered to study the interaction between UnPSip/CH and TOPSip-OH/A/G/CH composites and the mucin. The increase in the mucoadhesive strength of composites at this pH is mainly due to electrostatic attraction force between composites and the mucin. Electrostatic interaction between UnPSip/CH and TOPSip-OH/A/G/CH composites and mucin is favored at a pH between 3 and 6, in this pH range the composites are protonated and the mucin is negatively charged.

In addition, the higher mucoadhesive strength of the TOPSip-OH/A/G/CH composite could be due to the presence of a higher amount of CH available to interact with mucin compared to UnPSip/CH. Finally, the mucoadhesive strength increased with mucin concentration.

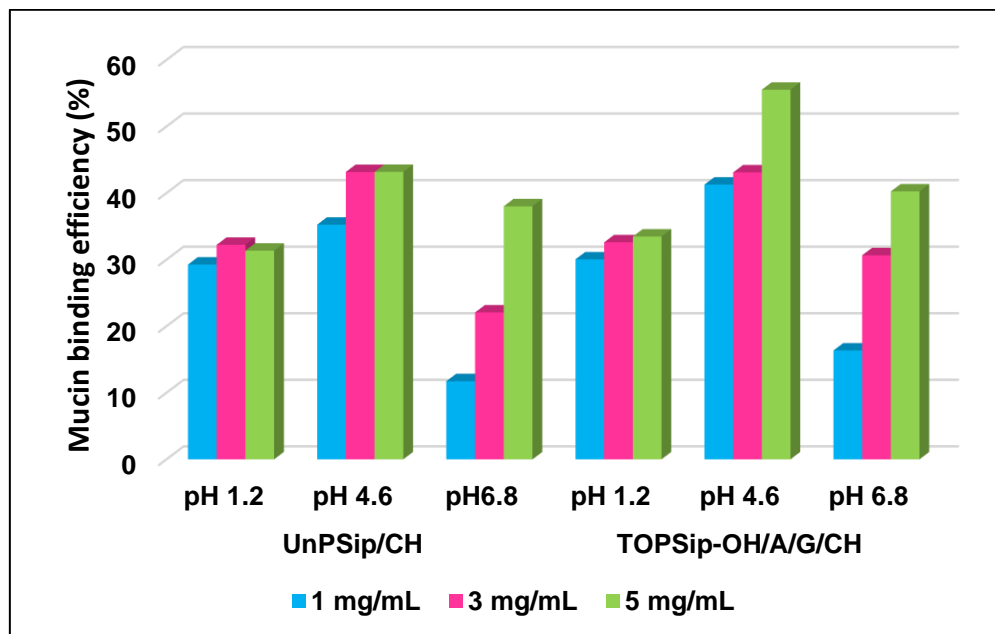


Fig. 7. Mucoadhesive strength of UnPSip/CH and TOPSip-OH/A/G/CH composites as a function of pH and mucin concentration.

3.5 TR loading and in vitro TR release study in UnPSip/CH and TOPSip-OH/A/G/CH

TR loading was performed in UnPSip and TOPSip-OH/A/G before to chemical bonding of the chitosan layer. The TR loading percentages obtained are 13 ± 1.7 % for UnPSip/CH and 11.5 ± 0.35 % for TOPSip-OH/A/G/CH. The low percentages of TR loading are mainly due to the rinses carried out with water after the synthesis of the composites. Although all the TR was expected to be trapped by the chitosan layer, the high solubility of TR in aqueous solution did not allow this.

The TR in vitro cumulative release profiles from UnPSip/CH and TOPSip-OH/A/G/CH composites were evaluated in SGF and SIF at 37 °C, under sink conditions. The TR release kinetics was evaluated for 30 h. Results are shown in Fig. 8.

The TR in vitro cumulative release profiles from UnPSip/CH and TOPSip-OH/A/G/CH were compared with the profiles obtained for bare TOPSip-OH₄₀ (Chapter 1, Section 3.5). The inspection of UnPSip/CH and TOPSip-OH/A/G/CH composites show more sustained and controlled TR release profiles (over 30 h) in comparison with TOPSip-OH in both simulated fluids. In SGF TOPSip-OH/TR composites behave similarly, releasing by burst effect, approximately 54 – 57 % of TR during the first 30 min. Initial burst release from composites can be explained in terms of low binding affinity between UnPSip/CH and TOPSip-OH/A/G/CH surface and TR in strong acid media. TR molecule has two pKa values, 9.41 and 13.1 [54]. At pH below 9.41 provides a positive charged molecule, mainly due to the protonation of tertiary amine. On the other hand, as observed in ξ -potential (Fig. 5), UnPSip/CH and TOPSip-OH/A/G/CH are positively charged due to the protonation of primary amino groups (-NH₂) and silanol (Si-OH) groups [36]. However, although the TOPSip-OH were covered with a CH layer after TR loading, the spontaneous desorption of TR occurred, mainly due to electrostatic repulsion force.

A different behavior was observed when releasing TR in SIF. In SIF, the burst effect is lower (8 - 31 %), which is attributed to a higher binding affinity between TR and UnPSip/CH and TOPSip-OH/A/G/CH surface. In SIF, TR has a positive charge and UnPSip/CH and TOPSip-OH/A/G/CH composites are negatively charged due to siloxane groups (SiO⁻) and carboxylic acid groups (-COOH) that are dissociated as carboxylate ion (-COO⁻), therefore intermolecular forces between UnPSip/CH and TOPSip-OH/A/G/CH surface and TR are favored, leading to less TR desorption.

TR cumulative release profiles were evaluated in two different composites, UnPSip/CH and TOPSip-OH/A/G/CH. By comparing the cumulative release profiles of both composites, a difference was observed in the percentage of released TR in SIF, the UnPSip/CH composites showed a more sustained release profile, while in SGF the release profile was like TOPSip-OH/A/G/CH. This is attributed to intermolecular interactions between the siloxane groups (SiO⁻) and carboxylate ion (-COO⁻) present in UnPSip/CH with TR, compared to only the present siloxane groups (SiO⁻) from TOPSip-

OH/A/G/CH. In addition, in UnPSip/CH, TR remains trapped inside the microstructure making it difficult for its diffusion towards the SIF. On the other hand, it seems that covalent bonds formed in TOPSip-OH/A/G/CH provide less stiffness to the polymeric chain allowing a higher drug diffusion.

Comparing the composites designed in this work with the TR delivery systems designed by other authors (Chapter 1, Table 4), UnPSip/CH composite may be suitable for efficient release with a TR dosage over 30 h.

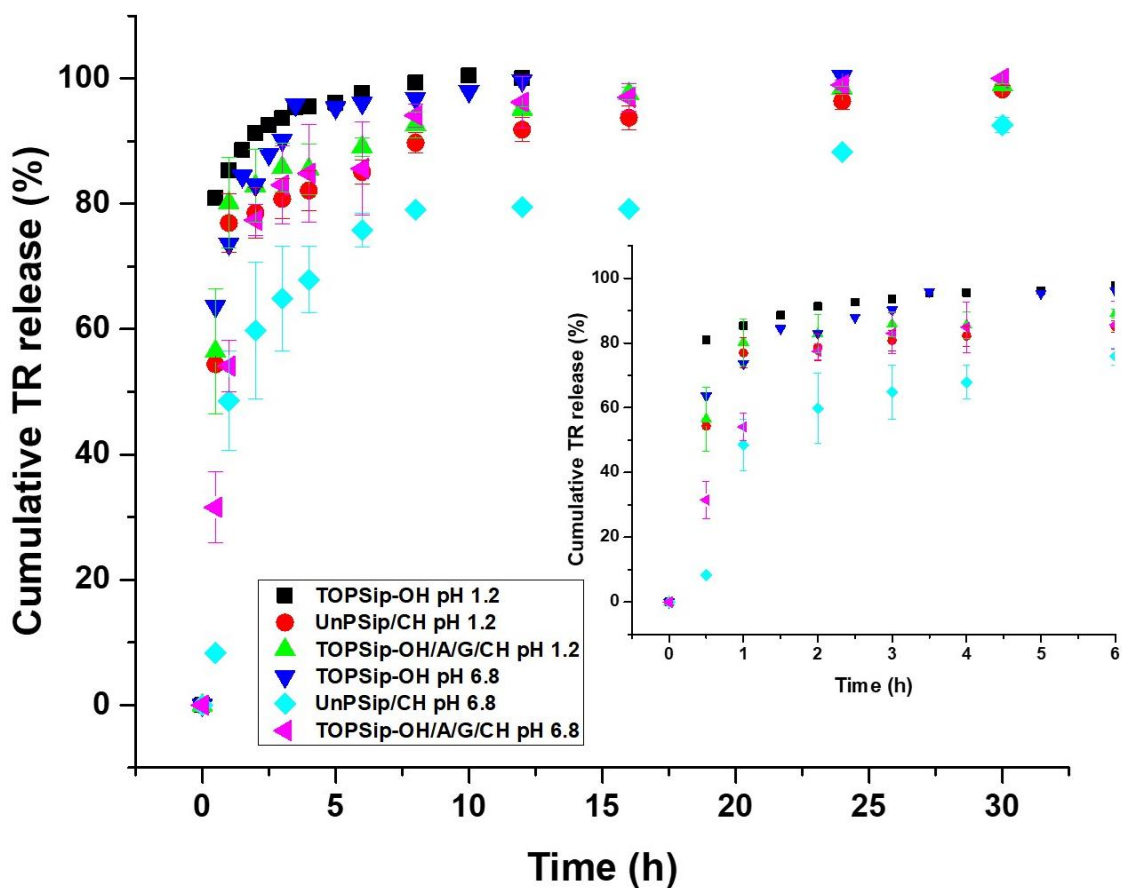


Fig. 8. In vitro cumulative TR release profiles of UnPSip/CH and TOPSip-OH/A/G/CH at 37 °C in simulated gastric fluid (pH 1.2) and simulated intestinal fluid (pH 6.8). Comparison with the cumulative TR release profiles of TOPSip-OH₄₀ (Chapter 1).

3.6 TR release kinetics modeling

The drug release mechanism for each composite was obtained by using the Korsmeyer-Peppas model (eq. 3). This model is generally applied when there is more than one mechanism governing the drug release profile (Eq. 3) [55].

$$\frac{M_t}{M_\infty} = k_{K-P} t^n \quad 3$$

In this mathematical expression, M_t/M_∞ is the fraction of drug released at time t , k_{K-P} is the Korsmeyer-Peppas kinetic release constant that incorporates the structural and geometrical characteristics of the release form. The n is the diffusional exponent describing the drug release mechanism [56, 57]. The release mechanism is determined according to the following values: $n \leq 0.5$ for Fickian diffusion, $0.5 < n < 1$ for anomalous transport, and $n = 1$ for a zero-order [58].

Cumulative release kinetic parameters and regression coefficients calculated from the Korsmeyer-Peppas model for both simulated fluids are presented in Table 1. At comparing the release rate constants (k_{K-P}) of UnPSip/CH and TOPSip-OH/A/G/CH composites, it was observed that the lowest k_{K-P} values were found for UnPSip/CH in both simulated fluids. These results agree with those explained above in vitro cumulative release profiles. Finally, these results confirm the sustained TR release and suggest that the TR release rate can be controlled by higher formation of intermolecular interactions between UnPSip/CH and TR, and a high stiffness to the polymeric chain allowing a less TR diffusion. The n values for all TOPSip-OH/TR composites were found < 0.5 suggesting a mechanism controlled by Fickian diffusion, which is mainly governed by the TR concentration gradient. However, there are several factors that can decrease TR release from composites, the main factor being the double release control due to the added CH layer. This layer can cover the pores of the PSip and delay the TR release, thus, in addition to the diffusion of TR through the nanostructured microparticle, it must also diffuse through the polymeric chains of the CH.

Table 1. Kinetic parameters of the UnPSip/CH and TOPSip-OH/A/G/CH composites at 37 °C and pH 1.2 and 6.8.

Kinetic parameters	SGF			SIF		
	k	n	R ²	k	n	R ²
UnPSip/CH	0.60 ± 0.046	0.17 ± 0.031	0.90	0.44 ± 0.05	0.23 ± 0.045	0.85
TOPSip-OH/A/G/CH	0.74 ± 0.024	0.09 ± 0.014	0.96	0.70 ± 0.021	0.10 ± 0.013	0.97

4. CONCLUSIONS

In this study, biodegradable and biocompatible composites based on chitosan and porous silicon microparticles was developed. APTES and GTA, and UA were successfully used as bridges to couple CH to PSi microparticles. FTIR spectroscopy and ξ -potential demonstrated the chemical modifications carried out at each step of the synthesis of composites. Drug release in UnPSip/CH and TOPSip-OH/A/G/CH composites were mediated by stiffness to the polymeric chain and intermolecular forces (electrostatic and/or van der Waals) created between composites surface and TR. Through this strategy, a sustained release of TR was achieved along 30 h. TR release was also mediated by pH. UnPSip/CH and TOPSip-OH/A/G/CH composites showed a high burst effect in SGF due to electrostatic repulsion forces between composites and TR. On the other hand, in SIF, a sustained release of TR was obtained due to the high affinity between TR (positive charge) and UnPSip/CH and TOPSip-OH/A/G/CH composites (negative charge) promoted in this physiological condition. It is essential to highlight that in SGF a low burst effect and a more sustained release profile were observed for UnPSip/CH. The cumulative TR release kinetic parameters in simulated fluids were determined. It was found that TR transport is mainly controlled by drug concentration gradient (Fickian diffusion) and coverage with CH. In addition, UnPSip/CH and TOPSip-OH/A/G/CH composites presented relevant mucoadhesive

properties, interacting with mucin, which is desirable to improve the absorption and effectiveness of TR. Mucoadhesive properties were higher at pH 4.6 (duodenum pH). These results suggest that mainly the composites will remain for an extended period in duodenum, where the absorption of TR begins. Finally, UnPSip/CH is a promising TR delivery system for oral therapy, increasing TR residence in intestine and maintaining a sustained release.

REFERENCES

1. Parveen S., Misra R. and Sahoo S. K. Nanoparticles: a boon to drug delivery, therapeutics, diagnostics and imaging. *Nanomedicine*, 2012, 8, 147-66.
2. Plapied L., Duhem N., des Rieux A. and Pr eat V. Fate of polymeric nanocarriers for oral drug delivery. *Curr Opin Colloid Interface Sci*, 2011, 16, 228-37.
3. Fonte P., Araujo F., Reis S. and Sarmento B. Oral insulin delivery: how far are we?. *J Diabetes Sci Technol*, 2013, 7, 520-31.
4. Shahbazi M. A. and Santos H. A. Improving Oral Absorption Via Drug-Loaded Nanocarriers: Absorption Mechanisms, Intestinal Models and Rational Fabrication. *Curr Drug Metab*, 2013, 14, 28-56.
5. Hamidi M., Azadi A., Rafiei P. and Ashrafi H. A Pharmacokinetic overview of nanotechnology-based drug delivery systems: an ADME-oriented approach, *Crit. Rev. Ther. Drug Carrier Syst.* 2013, 30, 435–467.
6. Janssen M., Mihov G., Welting T., Thies J. and Emans P. Drugs and Polymers for Delivery Systems in OA Joints: Clinical Needs and Opportunities. *Polymers*, 2014, 6, 799-819.
7. Garc a-Briones G. S., Ocampo-P erez R., G omez-Dur an C. F. A., Neri-G omez T. and Palestino G. Porous silicon microcarriers for extended release of metformin: Design, biological evaluation and 3D kinetics modeling, *Chem. Eng. J.* 2019, 365, 415–428.

8. Karthivashan G., Ganesan P., Park S. Y., Kim J. S. and Choi D. K. Therapeutic strategies and nano-drug delivery applications in management of ageing Alzheimer's disease. *Drug Delivery*, 2018, 25, 307-320.
9. Haney M. J., Klyachko N. L., Zhao Y., Gupta R., Plotnikova E. G., He Z., Patel T., Piroyan A., Sokolsky M., Kabanov A. V. and Batrakova E. Exosomes as drug delivery vehicles for Parkinson's disease therapy. *Journal of Controlled Release*, 2015, 207, 18-30.
10. Hani U., Rahamathulla M., Osmani R. A., Kumar H. Y., Urolagin D., Ansari M. Y., Pandey K., Devi K. and Yasmin S. Recent advances in novel drug delivery systems and approaches for management of breast cancer: A comprehensive review. *Journal of Drug Delivery Science and Technology*, 2020, 56, 101505.
11. Ruman U., Fakurazi S., Masarudin M. J. and Hussein M. Z. Nanocarrier-Based Therapeutics and Theranostics Drug Delivery Systems for Next Generation of Liver Cancer Nanodrug Modalities. *Int J Nanomedicine*, 2020, 15, 1437–1456.
12. Mehta M., Prasher P., Sharmad M., Shastrie M. D., Khurana N., Vyas M., Dureja H., Gupta G., Anand K., Satija S., Chellappan D. K. and Dua K. Advanced drug delivery systems can assist in targeting coronavirus disease (COVID-19): A hypothesis. *Medical Hypotheses*, 2020, 144, 110254.
13. Wang S. B. Ordered mesoporous materials for drug delivery. *Microporous Mesoporous Mater.* 2009, 117, 1-9.
14. Santos H. A., Bimbo L. M., Lehto V. P., Airaksinen A. J., Salonen J. and Hirvonen J. Multifunctional porous silicon for therapeutic drug delivery and imaging. *Curr Drug Discov Technol*, 2011, 8, 228-49.
15. Salonen J., Kaukonen A. M., Hirvonen J. and Lehto V. P. Mesoporous silicon in drug delivery applications. *J Pharm Sci*, 2008, 97, 632-53.
16. Kevadiya B. D., Joshi G. V., Mody H. M. and Bajaj H. C. Biopolymer–clay hidrogel composites as drug carrier: Host–guest intercalation and in vitro release study of lidocaine hydrochloride, *Appl. Clay Sci.*, 2011, 52, 364–367.
17. Zúñiga E., Belmar L., Toledo L, Torres C., Rivas B. L., Sánchez S. A. and Urbano B. F. Rhodamine-loaded surface modified mesoporous silica particles

- embedded into a thermoresponsive composite hydrogel for prolonged release, *Eur. Polym. J.* 2017, 95, 358–367.
18. Rasoulzadeh M. and Namazi H. Carboxymethyl cellulose/graphene oxide bio-nanocomposite hydrogel beads as anticancer drug carrier agent, *Carbohydr. Polym.* 2017, 168, 320–326.
 19. Dong X., Wei C., Liang J., Liu T., Kong D. and Lv F. Thermosensitive hydrogel loaded with chitosan-carbon nanotubes for near infrared light triggered drug delivery. *Colloids Surf. B Biointerf.* 2017, 154, 253–262.
 20. Rocha-García D., Guerra-Contreras A., Rosales-Mendoza S. and Palestino G. Mini Review Open Access Role of porous silicon/hydrogel composites on drug delivery. *Mesoporous Biomater.* 2016, 3, 93–101.
 21. Santos H. A., Mäkilä E. M., Airaksinen A. J., Bimbo L. M. and Hirvonen J. Porous silicon nanoparticles for nanomedicine: preparation and biomedical applications. *Nanomedicine (Lond)*, 2014, 9, 535-54.
 22. Kovalainen M., Mönkäre J., Mäkilä E., Salonen J., Lehto V. P. and Herzig K. H. Mesoporous silicon (PSi) for sustained peptide delivery: effect of PSi microparticle surface chemistry on peptide YY3-36 release. *Pharm Res*, 2012, 29, 837-46.
 23. Liu D., Bimbo L. M., Mäkilä E., Villanova F., Kaasalainen M. and Herranz-Blanco B. Co-delivery of a hydrophobic small molecule and a hydrophilic peptide by porous silicon nanoparticles. *J Control Release*, 2013, 170, 268e78.
 24. Salonen J., Laitinen L., Kaukonen A. M., Tuura J., Björkqvist M. and Heikkilä T. Mesoporous silicon microparticles for oral drug delivery: loading and release of five model drugs. *J Control Release*, 2005, 108, 362-74.
 25. Fu S. Y., Feng X. Q., Lauke B. and Mai Y. W. Effects of particle size, particle/matrix interface adhesion and particle loading on mechanical properties of particulate–polymer composites. *Compos. Part B Eng.* 2008, 39, 933–961.
 26. Hernandez-Montelongo J., Naveas N., Degoutin S., Tabary N., Chai F., Spampinato V. and Martel B. Porous silicon-cyclodextrin based polymer

- composites for drug delivery applications. *Carbohydr. Polym.*, 2014, 110, 238–52.
27. Tamilselvan N. and Raghavan C. V. Formulation and characterization of anti-alzheimer's drug loaded chitosan nanoparticles and its In vitro biological evaluation. *Journal of Young Pharmacists*, 2015, 7, 28-36.
 28. Md S., Khan R. S., Mustafa G., Chuttani K., Baboota S., Sahni J. K. and Ali J. Bromocriptine loaded chitosan nanoparticles intended for direct nose to brain delivery: Pharmacodynamic, Pharmacokinetic and Scintigraphy study in mice model. *European Journal of Pharmaceutical Sciences*, 2013, 48, 393–405.
 29. Shrestha N., Shahbazi M. A., Araújo F., Zhang H., Mäkilä E. M., Kauppila J., Sarmiento B., Salonen J., Hirvonen J. T. and Santos, H. A. (2014), "Chitosan-modified porous silicon microparticles for enhanced permeability of insulin across intestinal cell monolayers", *Biomaterials*, 35, 7172-7179.
 30. Kafshgari M. H., Delalat B., Tong W. Y. Harding F. J., Kaasalainen M. Salonen J. and Voelcker N. H. Oligonucleotide delivery by chitosan-functionalized porous silicon nanoparticles. *Nano Research*, 2015, 8, 2033–2046.
 31. Cisneros-Covarrubias C. A., Palestino G., Gómez-Durán C. F. A. Rosales-Mendoza S. and Betancourt-Mendiola M. L. Optimized microwave-assisted functionalization and quantification of superficial amino groups on porous silicon nanostructured microparticles. *Anal. Methods*, 2021, 13, 516.
 32. Tabasi O., Falamaki C. and Khalaj Z. Functionalized mesoporous silicon for targeted-drug-delivery, *Colloids and Surfaces B: Biointerfaces*, 2012, 98, 18–25.
 33. Sailor M. J. *Fundamentals of porous silicon preparation. Porous Silicon in Practice: Preparation, Characterization and Applications*, San Diego, California.: Wiley-VCH Verlag GmbH & Co. KGaA, Weinheim, Germany, 2012.
 34. Mali K. K., Dhawale S. C., Dias R. J., Dhane N. S. and Ghorpade V. S. Citric Acid Crosslinked Carboxymethyl Cellulose-based Composite Hydrogel Films for Drug Delivery. *Indian J Pharm Sci.*, 2018, 80(4), 657-667.

35. Wang X., Zheng C., Wu Z., Teng D., Zhang X., Wang Z. and Li C. Chitosan-NAC Nanoparticles as a Vehicle for Nasal Absorption Enhancement of Insulin. *J Biomed Mater Res B Appl Biomater.*, 2009, 88, 150-161.
36. Jarvis K. L., Barnes T. J. and Prestidge C. L. Surface chemistry of porous silicon and implications for drug encapsulation and delivery applications. *Advances in Colloid and Interface Science*, 2012, 175, 25–38.
37. Sciacca B., Secret E., Pace S., Gonzalez P., Geobaldo F., Quignard F. and Cunin F. Chitosan-functionalized porous silicon optical transducer for the detection of carboxylic acid-containing drugs in water. *J. Mater. Chem.*, 2011, 21, 2294–2302.
38. Shrestha N., Shahbazi M., Araujo F., Mäkilä E., Raula J., Kauppinen E. I., Salonen J., Sarmiento B., Hirvonen J. and Santos H. A. Multistage pH-Responsive Mucoadhesive Nanocarriers Prepared by Aerosol Flow Reactor Technology: A Controlled Dual Protein-Drug Delivery System. *Biomaterials* (2015), doi: 10.1016/j.biomaterials.2015.07.045.
39. Almansa C., Mercè R., Tesson N., Farran J., Tomàs J. and Plata-Salamán C. R. Co-crystal of Tramadol Hydrochloride-Celecoxib (ctc): A Novel API-API Co-crystal for the Treatment of Pain, *Cryst. Growth Des.* 2017, 17, 1884–1892.
40. Palla N., Rajashekar V., Marni P., Mittepalli J. and Sridhar K. A. Formulation and in-Vitro Evaluation of Tramadol Hydrochloride Floating Tablets, *Int. Res. J. Pharm.* 2016, 4, 138–144.
41. Zhang D., Hegab H. E., Lvov Y., Snow L. D. and Palmer J. Immobilization of cellulase on a silica gel substrate modified using a 3-APTES self-assembled monolayer, *SpringerPlus*, 2016, 5:48.
42. Sutirman Z. A., Sanagi M. M., Karim K. J. and Ibrahim W. A. Preparation of methacrylamide-functionalized crosslinked chitosan by free radical polymerization for the removal of lead ions, *Carbohydrate Polymers*, 2016, 151, 1091–1099.
43. Kaasalainen M., Mäkilä E., Riikonen J., Kovalainen M., Järvinen K., Herzig K. H., Lehto V. P. and Salonen J. Effect of isotonic solutions and peptide adsorption

- on zeta potential of porous silicon nanoparticle drug delivery formulations, *International Journal of Pharmaceutics*, 2012, 431, 230–236.
44. Drug bank. <https://go.drugbank.com/drugs/DB11117>
45. Ramanery F. P., Mansur A. A. P. and Mansur H. S. One-step colloidal synthesis of biocompatible water-soluble ZnS quantum dot/chitosan nanoconjugates, *Nanoscale Research Letters*, 2013, 8:512.
46. Rocha-García D., Betancourt-Mendiola M. de L., Wong-Arce A., Rosales-Mendoza S., Reyes-Hernández J., González-Ortega O. and Palestino G. Gelatin-based porous silicon hydrogel composites for the controlled release of tramadol. *Eur. Polym. J.*, 2018, 108, 485–497.
47. Zhang Q. and Du L. Hydrogen bonding in the carboxylic acid–aldehyde complexes, *Computational and Theoretical Chemistry*, 2016, 1078, 123–128.
48. Lee S., Müller M., Rezwan K. and Spencer N. D. Porcine gastric mucin (PGM) at the water/poly(dimethylsiloxane) (PDMS) interface: Influence of pH and ionic strength on its conformation, adsorption, and aqueous lubrication properties, *Langmuir*, 2005, 21, 8344–8353.
49. Celli J. P., Turner B. S., Afdhal N. H., Ewoldt R. H., McKinley G. H., Bansil R. and Erramilli S. Rheology of gastric mucin exhibits a pH-dependent sol-gel transition, *Biomacromolecules*, 2007, 8, 1580–1586.
50. Bansil R. and Turner B. S. The biology of mucus: Composition, synthesis, and organization. *Adv. Drug Deliv. Rev.*, 2018, 124, 3–15.
51. Collado-González M., González Espinosa Y. and Goycoolea F. M. Interaction Between Chitosan and Mucin: Fundamentals and Applications, *Biomimetics*, 2019, 4, 32.
52. Haugstad K. E., Hati A. G., Nordgard C. T., Adl P. S., Maurstad G., Sletmoen M., Draget K. I., Dias R.S. and Stokke B. T. Direct determination of chitosan-mucin interactions using a single-molecule strategy: Comparison to alginate-mucin interactions, *Polymers*, 2015, 7, 161–185.

53. Collins J. T., Nguyen A. and Badireddy M. Anatomy, Abdomen and Pelvis, Small Intestine, 2020, In: StatPearls [Internet]. Treasure Island (FL): StatPearls Publishing; 2021 Jan–. PMID: 29083773.
54. Smyj R., Wang X. P. and Han F. Tramadol Hydrochloride, Profiles Drug Subst Excip Relat Methodol, 2013, 38, 463-94.
55. N.H. Maniya, S.R. Patel, Z.V.P. Murthy, Drug delivery with porous silicon films, microparticles, and nanoparticles, Rev. Adv. Mater. Sci. 44 (2016) 257–272.
56. C. Maderuelo, A. Zarzuelo, J.M. Lanao, Critical factors in the release of drugs from sustained release hydrophilic matrices, J. Control. Release. 154 (2011) 2–19. doi:10.1016/j.jconrel.2011.04.002.
57. D. Wójcik-Pastuszka, J. Krzak, B. Macikowski, R. Berkowski, B. Osiński, W. Musiał, Evaluation of the release kinetics of a pharmacologically active substance from model intra-articular implants replacing the cruciate ligaments of the knee, Materials (Basel). 12 (2019). doi:10.3390/ma12081202.
58. R.W. Korsmeyer, R. Gurny, E. Doelker, P. Buri, N.A. Peppas, Mechanisms of solute release from porous hydrophilic polymers, Int. J. Pharm. 15 (1983) 25–35. doi:10.1016/0378-5173(83)90064-9.

GENERAL CONCLUSIONS

In recent years, the use of composite materials applied to the controlled release of therapeutic agents grew exponentially due to the advantageous properties they present, in addition, composite materials can be designed by modifying the synthesis parameters with the main objective of obtaining the optimal characteristics that improve the dosage of therapeutic agents. In this research work, two different types of biodegradable and biocompatible drug delivery systems were proposed based on the combination of porous silicon microparticles and chitosan for the transport and sustained release of TR. The synthesis and study of these tramadol release systems was carried out in three stages.

As a first stage, the development of bare thermally oxidized porous silicon microparticles (TOPSiP) with different particle sizes, pore sizes and porosity were proposed. A highly efficient top-down approach was used to synthesize the TOPSiP and it was shown that the synthesis parameters played an essential role in the materials design. The modified synthesis parameters were current density, concentration of HF relative to ethanol, ultrasonication time, material architecture, and number of perforations. Through the characterization techniques of HRSEM and FT-IR, the successful synthesis of TOPSiP was demonstrated. Average size, thickness, and pore dimensions were calculated, measuring at least 150 PSi microparticles randomly selected in the HRSEM images. Modifying these parameters showed that TOPSiP with large particle sizes and small pore sizes were produced by using high concentration of HF relative to ethanol (3:1) and low ultrasonication times (15 min) of monolayers. In contrast, TOPSiP with smaller particle size and larger pore size were obtained using a low concentration of HF relative to ethanol (3:7) and high ultrasonication time (60 min) of multilayers of 40 defects. With respect to porosity, porosity was determined from gravimetric measurements. High porosities (86 – 89 %) were obtained using low concentrations of HF relative to ethanol. FT-IR, ζ -potential and UV-Vis spectroscopy demonstrated that TR molecules were successfully adsorbed on the TOPSiP porous structure by intermolecular forces (ion-ion electrostatic forces and hydrogen bonding)

created between the TR and the TOPSip inorganic surface. Percentages of TR loading capacity of 10 – 31 % were obtained, which was mainly mediated by pore dimension. TOPSip with bigger pore size showed a higher TR loading capacity (31 %), instead, the lowest drug loading capacity (10 %) was found governed by particles with smaller pore size. The in vitro TR cumulative release profiles study was performed at 37 °C in two simulated fluids: gastric and intestinal, simulating the TR process desorption in the human organism. This study showed that TR cumulative release was mediated by the particles pore size, solvent diffusion, and pH. TOPSip with smallest pore size and largest particle dimensions achieved a sustained TR release over 24 h in both simulated fluids with a non-significant burst effect compared to the rest of the nanostructured TOPSip. Due to the high affinity between TR (positive charge) and TOPSip inorganic surface (negative charge) promoted in simulated intestinal fluid, TR sustained release was obtained. On the other hand, in simulated gastric fluid an initial burst release from TOPSip was obtained, which can be explained in terms of microparticles low stability and low binding affinity between TOPSip inorganic surface (positive charge) and TR (positive charge) in strong acid media. The analysis of TR release kinetics for a time of 24 h showed that TR transport is mainly controlled by drug concentration gradient (Fickian diffusion). Finally, the in vivo evaluation using TOPSip microcarriers was performed for the first time. Models of carrageenan-induced inflammation and withdrawal threshold by mechanical stimulation in rats were used. These studies showed that the TOPSip did not cause any adverse effects in rats and evidence of better and sustainable anti-nociceptive and anti-inflammatory effects were obtained when using TOPSip-OH/TR composites compared with TR alone. In addition, it is essential to highlight that the treatment with TOPSip-OH/TR composite at the lowest TR dosage increased the anti-inflammatory and antinociceptive effect compared to TR alone at its highest dose.

However, despite the results of in vivo studies showing that TOPSip microcarriers with reasonable particle size and pore size enhanced the pharmacokinetic effect of TR, in vitro release studies showed an initial burst effect. Based on this, it was proposed to chemically binding CH to the PSip inorganic surface,

to obtain more controlled drug release profiles. The chemical binding of CH to the PSip was carried out using UA and APTES-GTA as bridges. The functionalization protocol of native PSi layers with UA has already been established in our research group, however, the APTES functionalization of PSip has not been fully established. It was observed in the literature that there are many functionalization conditions of PSip with APTES, therefore, as a second part of the work, the APTES functionalization of PSip under different reaction conditions using the traditional and MW-assisted silanization methods was studied. In this study, the modified variables were reaction time (5 - 30 min), reaction temperature (80 - 120 °C), TOPSip chemical surface (silanol and siloxane groups), APTES solution concentration (2 and 5 %) and silanization method (traditional and MW-assisted). Our studies showed that the MW-assisted method had a significant reduction in reaction time (26 min) when compared to the traditional method (24 h), moreover APTES surface coverage increased by 39 % using MW irradiation. Surface modification was evidenced by FT-IR, STEM, and elements mapping; as well as ζ -potential measurements. It was found that silanol groups (Si-OH) in TOPSip-OH increased 3-fold the amino surface coverage when using a 5 % APTES solution. Compared to using TOPSip with siloxane groups (SiO⁻) and the same APTES solution. In addition, it was found that using a 5 % APTES solution and TOPSip-OH increased the amino surface coverage compared to a 2 % APTES solution on the same PSip. The optimization and modeling of APTES functionalization on TOPSip-OH with 5% APTES solution and MW-assisted method using a composite central design was proposed. APTES surface functionalization was found to strongly depend on the reaction time, reaction temperature and percentage of APTES. The optimal functionalization conditions were obtained at middle-temperature values (95 °C), using 5 % APTES solution in dry toluene for 26 min. Finally, the ninhydrin method was adapted to quantify amino functional groups in PSip. The concentration of amino functional groups quantified by the ninhydrin method was confirmed by TGA. Comparing both results, it was concluded that ninhydrin method is an excellent alternative for amino groups quantification. Another important advantage of the ninhydrin method is that this method involves direct reaction with amino groups;

therefore, quantification is primarily directed at accessible amino groups. Which is relevant since the quantified amino groups are used in subsequent functionalization reactions.

Finally, as the third stage of the research work, the synthesis of biodegradable and biocompatible composites based on chitosan and PSip was carried out: UnPSip/CH and TOPSip-OH/A/G/CH. The native PSi layers were functionalized with UA (UnPSip), functionalization conditions established in the literature and implemented in our research group were used, and a concentration of carboxylic groups of 1.6 mEq/g of UnPSip was obtained. On the other hand, APTES functionalization of TOPSip-OH (TOPSip-OH/A) was carried out using the optimal functionalization conditions obtained in the second stage. Subsequently, the functionalization of the amino groups with GTA (TOPSip-OH/A/G) was carried out, obtaining a reaction's efficiency of 81%. CH was chemically linked to the aldehyde groups of the TOPSip-OH/A/G and to the carboxylic acid groups of the UnPSip. FTIR spectroscopy and ξ -potential demonstrated the chemical modifications carried out at each step of the synthesis of composites. TR loading capacity was lower in composites compared to bare TOPSip. This is the result of the prolonged exposure time (24 h) of the UnPSip/TR and TOPSip-OH/A/G/TR with the medium used in the chemical binding of CH (buffer pH 5). TR is highly soluble in aqueous media, therefore, while CH was chemically bound to UnPSip/TR and TOPSip-OH/A/G/TR, TR diffused from the particles into the medium, causing large amount of TR will be removed in the supernatant. TR release of UnPSip/TR/CH and TOPSip-OH/A/G/TR/CH composites were mediated by stiffness to the polymeric chain and intermolecular forces (electrostatic and/or van der Waals) created between composites surface and TR. Through this strategy, a sustained release of TR was achieved along 30 h. TR release was also mediated by pH. UnPSip/TR/CH and TOPSip-OH/A/G/TR/CH composites showed a high burst effect in SGF due to electrostatic repulsion forces between composites and TR. On the other hand, in SIF, a sustained release of TR was obtained due to the high affinity between TR (positive charge) and UnPSip/CH and TOPSip-OH/A/G/CH composites (negative charge) promoted in this physiological condition. The analysis of TR release kinetics for a time of 30 h showed

that TR transport is mainly controlled by drug concentration gradient (Fickian diffusion). To determine the absorption in the intestine and effectiveness of TR, the mucoadhesive properties were studied by the adsorption of mucin. Mucoadhesive properties were higher at pH 4.6 (duodenum pH) compared with SGF and SIF. These results suggest that mainly the composites will remain for an extended period in duodenum, where the absorption of TR begins. Finally, UnPSip/CH is a promising TR delivery system for oral therapy, increasing TR residence in intestine and maintaining a sustained release.

APPENDIX A

Published articles, Congresses and Awards certificates

Analytical
Methods



PAPER

[View Article Online](#)
[View Journal](#) | [View Issue](#)



Cite this: *Anal. Methods*, 2021, 13, 516

Optimized microwave-assisted functionalization and quantification of superficial amino groups on porous silicon nanostructured microparticles

Cándida Anahy Cisneros-Covarrubias,^a Gabriela Palestino,^{ab} César F. A. Gómez-Durán,^{ab} Sergio Rosales-Mendoza^{ab} and Maria de Lourdes Betancourt-Mendiola^{ab*}

This work presents an optimized microwave (MW)-assisted method for the chemical functionalization of porous silicon particles (PSip). 3-(Aminopropyl)triethoxysilane (APTES) was grafted on previously stabilized PSip. The functionalization efficiency was studied and optimized in terms of reaction time (RT) and reaction temperature (RT) using a central composite design (CCD). The effect of MW irradiation on the surface coverage was found to strongly depend on the PSip surface chemistry, Rt, RT, and percentage of APTES. Quantification of grafted amino groups was performed by the ninhydrin method (NHIM); confirming the results by thermogravimetric analysis (TGA). Reacting with 5% APTES solution at 95 °C for 26 min was the best functionalization conditions. The efficiency of PSip-APTES prepared under the optimized conditions was compared to those functionalized by the traditional method; MW irradiation increases by 39% the number of functional groups grafted onto the PSip surfaces with the additional benefit of having a drastic reduction in Rt.

Received 10th November 2020
Accepted 23rd December 2020

DOI: 10.1039/d0ay02083d

rsc.li/methods